**Department of Mechanical and
Industrial Engineering
University of Illinois at
Urbana-Champaign
Urbana, IL 61801**

UILU-ENG 94-4010

Annual Technical Report

SHOCK INITIATION OF CRYSTALLINE BORON IN OXYGEN AND FLUORINE COMPOUNDS

Herman Krier, Rodney L. Burton, and S. R. Pirman

Annual Contract Report Submitted to

Office of Naval Research
Dr. Richard S. Miller, Program Manager
for research conducted during the period
1 June 1993 to 31 May 1994

under
Contract N00014-93-1-0654

August 1994

Approved for Public Release;
Distribution Unlimited

135 pp

UNCLASSIFIED
SECURITY CLASSIFICATION OF THIS PAGE

REPORT DOCUMENTATION PAGE

Form Approved OMB No. 0704-0188

1a. REPORT SECURITY CLASSIFICATION
Unclassified

1b. RESTRICTIVE MARKINGS
None

2a. SECURITY CLASSIFICATION AUTHORITY

2b. DECLASSIFICATION / DOWNGRADING SCHEDULE

3. DISTRIBUTION / AVAILABILITY OF REPORT
Approved for public release;
distribution is unlimited

4. PERFORMING ORGANIZATION REPORT NUMBER(S)
UILU-ENG-94-4010

5. MONITORING ORGANIZATION REPORT NUMBER(S)
N A

6a. NAME OF PERFORMING ORGANIZATION
University of Illinois at
Urbana-Champaign

6b. OFFICE SYMBOL *(If applicable)*
UIUC

7a. NAME OF MONITORING ORGANIZATION
Office of Naval Research

6c. ADDRESS *(City, State, and ZIP Code)*
Department of Mechanical & Industrial Engineering
140 MEB; 1206 W. Green Street
Urbana, IL 61801

7b. ADDRESS *(City, State, and ZIP Code)*
Code 332; Propulsion & Energetics
800 N. Quincy Street
Arlington, VA 22217-5660

8a. NAME OF FUNDING / SPONSORING ORGANIZATION
Naval Office of Research

8b. OFFICE SYMBOL *(If applicable)*
ONR

9. PROCUREMENT INSTRUMENT IDENTIFICATION NUMBER

8c. ADDRESS *(City, State, and ZIP Code)*
Code 332
800 North Quincy Street
Arlington, VA 22217-5660

10. SOURCE OF FUNDING NUMBERS

PROGRAM ELEMENT NO.	PROJECT NO.	TASK NO.	WORK UNIT ACCESSION NO.

11. TITLE *(Include Security Classification)*
Shock Initiation of Crystalline Boron in Oxygen and Fluorine Compounds

12. PERSONAL AUTHOR(S)
Herman Krier, Rodney L. Burton, and Stephen R. Pirman

13a. TYPE OF REPORT
Annual

13b. TIME COVERED
FROM 6/1/93 TO 5/31/94

14. DATE OF REPORT *(Year, Month, Day)*
August 31, 1994

15. PAGE COUNT
134

6. SUPPLEMENTARY NOTATION

7. COSATI CODES

FIELD	GROUP	SUB-GROUP

18. SUBJECT TERMS *(Continue on reverse if necessary and identify by block number)*
Ignition of metal powder; Shock tube initiation

9. ABSTRACT *(Continue on reverse if necessary and identify by block number)*

The ignition delay and combustion of amorphous and crystalline boron particles is investigated at elevated temperatures and pressures for wet, dry, and fluorine-containing atmospheres. Particles ranging from sub-micron to 32 μm in diameter are ignited in the ambient conditions produced by a reflected shock wave in a shock tube. The ignition delay and combustion times are examined as a function of temperature for pressures of 8.5, 17, and 34 atm and for oxidizer mixtures of 100% oxygen, 30% water vapor, 1-3% sulfur hexafluoride, and 6-12% hydrogen fluoride. Results indicate that pressure in the range studied does not affect the ignition delay or burn time. The additives, water vapor and sulfur hexafluoride, reduce the ignition delay time for amorphous and sub-micron crystalline boron when compared to oxygen. For 20 μm particles, H_2O and SF_6 reduce the ignition temperature limit from 2500 K in pure oxygen to 2200 K and 1900 K, respectively. Burn time is unaffected by the additives. Hydrogen fluoride did not show any change in ignition delay or burn time compared to pure oxygen. At the range of temperatures tested, very little (less than 2%) of HF is dissociated into H and F atoms.

The report also presents reviews of previous chemical and physical models that have attempted to explain why boron powder is relatively difficult to ignite.

20. DISTRIBUTION / AVAILABILITY OF ABSTRACT
☒ UNCLASSIFIED/UNLIMITED ☒ SAME AS RPT. ☐ DTIC USERS

21. ABSTRACT SECURITY CLASSIFICATION
Unclassified

2a. NAME OF RESPONSIBLE INDIVIDUAL
Dr. Richard s. Miller

22b. TELEPHONE *(Include Area Code)*
703/ 696-4407

22c. OFFICE SYMBOL
ONR

D Form 1473, JUN 86 *Previous editions are obsolete.*

SECURITY CLASSIFICATION OF THIS PAGE
UNCLASSIFIED

ANNUAL TECHNICAL REPORT

No. UILU ENG 94-4010

For research supported by contract
N00014-93-1-0654

for period 06/01/93 to 05/31/94

SHOCK INITIATION OF CRYSTALLINE BORON IN OXYGEN AND FLUORINE COMPOUNDS

prepared by

Herman Krier(1), Rodney L. Burton(2), and Stephen R. Pirman(3)

Department of Mechanical and Industrial Engineering
University of Illinois at Urbana-Champaign
1206 West Green Street
Urbana, IL 61801

Work supported by

Office of Naval Research
Dr. Richard S. Miller is Program Manager

---

(1) Co-Principal Investigator
(2) Co-Principal Investigator, Department of Aeronautical and Astronautical Engineering
(3) Graduate Research Assistant

AUGUST 1994

ABSTRACT

The ignition delay and combustion of amorphous and crystalline boron particles is investigated at elevated temperatures and pressures for wet, dry, and fluorine-containing atmospheres. Particles ranging from sub-micron to 32 µm in diameter are ignited in the ambient conditions produced by a reflected shock wave in a shock tube. The ignition delay and combustion times are examined as a function of temperature for pressures of 8.5, 17, and 34 atm and for oxidizer mixtures of 100% oxygen, 30% water vapor, 1-3% sulfur hexafluoride, and 6-12% hydrogen fluoride. Results indicate that pressure in the range studied does not affect the ignition delay or burn time. The additives, water vapor and sulfur hexafluoride, reduce the ignition delay time for amorphous and sub-micron crystalline boron when compared to oxygen. For 20 µm particles, H_2O and SF_6 reduce the ignition temperature limit from 2500 K in pure oxygen to 2200 K and 1900 K, respectively. Burn time is unaffected by the additives. Hydrogen fluoride did not show any change in ignition delay or burn time compared to pure oxygen. At the range of temperatures tested, very little (less than 2%) of HF is dissociated into H and F atoms. A review of previous chemical and physical models that have attempted to explain why boron powder is relatively difficult to ignite is presented for comparison.

ACKNOWLEDGMENTS

We greatly appreciate the expertise and the assistance of Ph.D. candidate, Robert O. Foelsche, who was instrumental in redeploying our shock tube facility into a new building and who was often consulted when interpreting the data with the chemical models for boron combustion. We also acknowledge Chuck Meyer and Ushio Yuki, both undergraduate research assistants, for their efforts as lab assistants. The work by former graduate students (who did shock tube research), Ted Roberts and Tom Megli, allowed this effort to be completed in a reasonable time period.

Finally, we express our gratitude to the Office of Naval Research for supporting this work.

TABLE OF CONTENTS

APPENDIX

LIST OF TABLES

LIST OF FIGURES

LIST OF VARIABLES

English Symbols

a	Speed of sound
C_{H_2O}	Concentration of water vapor
c_p	Specific heat capacity
c_1	Curve fit constant
c_2	Curve fit constant
C_2	Equation constant
D	Source term
d_o	Initial diameter
e	Energy
H_{fus}	Enthalpy of fusion
H_{vap}	Enthalpy of vaporization
k	Thermal conductivity
l	Length of driver section
L	Length of shock tube
M	Mach number
M_R	Mach number of reflected shock wave
M_S	Mach number of incident shock wave
M_{S_i}	Mach number of incident shock wave
MW	Molecular weight
P	Pressure
P_F	Final pressure
p_{gas}	Partial pressure of additive
P_∞	Ambient pressure
Q	Heat of reaction
r	Radial position
R_u	Universal gas constant
t	time
t_{ew}	time shock wave reaches the endwall
t_{ign}	Ignition delay time
t_{burn}	Burn time
T	Temperature
T_{bp}	Boiling temperature
T_F	Final temperature

T_{ign}	Ignition temperature
T_{mp}	Melting temperature
T_o	Initial temperature
T_∞	Ambient temperature
u	Velocity
u_p	Velocity of gases behind incident shock wave
V_{S_i}	Velocity of incident shock wave
v	Velocity
w	Velocity of incident shock wave
w_i	Uncertainty of variable i
w_R	Velocity of reflected shock wave
x	Distance
X_{H_2O}	Mole fraction of water vapor
X_{O_2}	Mole fraction of oxygen
y_{gas}	Mole fraction of additives

Greek Symbols

α	Equation constant
ρ	Density
γ	Specific heat ratio

Numerical Subscripts

1	Initial conditions in driven section
1	First peak of photodiode signal
2	Conditions behind incident shock wave
2	Second peak in photodiode signal
3	Third peak in photodiode signal
4	Initial conditions in driver section
4	Fourth peak in photodiode signal
5	Conditions behind reflected shock wave

Elements

Al	Aluminum
Ar	Argon
Be	Beryllium
B	Boron
C	Carbon
Ca	Calcium
F	Fluorine
H	Hydrogen
He	Helium
Na	Sodium
O	Oxygen
S	Sulfur

Compounds

Al_2O_3	Aluminum oxide
BeO	Beryllium oxide
BF_3	Boron trifluoride
BO	Boron oxide
BO_2	Boron oxide
BOH	Boric acid
B_2O_2	Boron oxide
B_2O_3	Boron oxide
$Ca(OH)_2$	Calcium hydroxide
CH_2	Methylene
CO	Carbon monoxide
CO_2	Carbon dioxide
F_2	Fluorine
HBO	Boric acid
HF	Hydrogen fluoride
HOBO (HBO_2)	Boric acid
JP5	Hydrocarbon jet fuel
M	Radical
NaOH	Sodium hydroxide
O_2	Oxygen
OBF	Boron oxyfluoride

OH	Hydroxyl
SF_6	Sulfur hexafluoride

CHAPTER 1 - INTRODUCTION

The use of high energy density materials has important applications. The desire for a controlled high energy release in various applications has warranted extensive research in the area of liquid and solid propellant combustion. Whether the energetic material is used for rocket propulsion or detonation purposes, performance increases are always a major goal. A concentrated effort has also been placed into studying metalized solid propellant combustion, which can yield large amounts of energy per unit volume. Currently, aluminum and magnesium are the metals of choice. However, if it is desired to obtain the highest energy possible, then the most likely candidate is *boron*.

1.1 Benefits of Boron as a Fuel

Boron has great potential for use as an additive for an energetic material. Apart from being a relatively common element, it has the greatest heating value of any other fuel, except for beryllium, used with oxygen. Table 1.1 lists the heating values for some of the more common fuels. Beryllium, when it reacts with oxygen, forms BeO which is extremely toxic, so beryllium is never considered a viable fuel. As can be clearly seen, boron has considerably greater heating values per unit mass and per unit volume. If it is to be used as a rocket fuel, the reduction of weight and volume of the fuel will result in higher payloads or longer durations of flight, not to mention a more cost effective flight.

Also being considered is the use of boron for controlled, non-ideal detonations. The high energy output with delayed reaction will generate an expanded pressure-volume process, which

Table 1.1 Heating values of various fuels [1, 2].

Fuel/Additive	Gravimetric Heating Value [cal/g]	Volumetric Heating Value [cal/cm^3]
JP5 (Jet fuel)	10,150	8,230
Kerosene	9,860	10,000
Propane	12,230	24,000
Coal, C(s)	7,830	17,700
$(CH_2)_n$	10,400	9,600
Aluminum	7,420	20,000
Magnesium	5,910	10,300
Beryllium	15,890	29,400
Boron	13,800	32,200

would result in more work output. However, having a high heating value does not alone make a material a desirable fuel.

1.2 Disadvantages of Boron as a Fuel

For a material to be a likely candidate for a fuel or fuel additive, it must be able to ignite, burn, and release its energy within the combustor region of a rocket. Unfortunately, boron does not meet this criteria for most applications [1]. The main reason that boron is difficult to ignite is that the particle is coated with an oxide layer, B_2O_3. The oxide layer, which is present whenever the particle is in an oxygen containing atmosphere, inhibits further oxidation of the particle and therefore restricts the ignition process.

Burning of the particle is also restricted by the oxide layer. After the particle reaches a certain temperature, the oxide layer will liquefy. This allows some oxygen to slowly diffuse through the liquid layer and to react with the boron. However, the reaction will then produce more oxide and will increase the thickness of the oxide layer, which will retard the diffusion process as well as the combustion of the particle.

Finally, full utilization of energy from the combustion reaction is difficult to achieve because most of the energy is never released. The chemical reaction of the boron and oxygen is exothermic but most of that energy initially is used to continue the heat up of the particle. Also, because boron has high melting and boiling temperatures, the heating of the particle can continue for durations longer than most residence times in combustors. If the particle happens to react completely, most of the products formed will be in the gas phase. The high energy output shown in Table 1.1 is not achieved until the products condense to liquid phase. The trapping of the products in the gas phase can potentially reduce the heating value of boron by up to 25 percent. The condensing of the boron products is relatively slow until the temperature drops significantly, and therefore the benefits of the high energy release are realized too late [1, 3].

1.3 Comparison of Boron with Aluminum

Other solid fuels have similar qualities with boron, so that it would seem that the combustion process would also be similar. For instance aluminum, which is in the same group on the periodic table as boron and has been utilized extensively for rocket propulsion, also forms an oxide layer upon heating, which is also similar to the structure of boron oxide (Al_2O_3 and B_2O_3). Table 1.2 lists some of the properties of boron and aluminum and their oxides. However, as can be seen, the two elements and their oxides have little in common, especially their melting and boiling temperatures and the enthalpy of fusion. There is little in common in the ignition process as well [1, 4].

Table 1.2 Physical properties of amorphous and crystalline boron and aluminum and their oxides, B_2O_3 an Al_2O_3, respectively.

Physical Property	Amorphous Boron	Crystalline Boron	Boron Oxide	Aluminum	Aluminum Oxide
ρ [g/cm^3]	2.22 [2]	2.35 [6]	2.99 [11]	2.70 [7]	3.98 [7]
k [W/m K] @ 300 K	27.6 [9]	27.4 [6]	—	237 [7]	36 [7]
k [W/m K] @ 800 K	8.1 [9]	7.36 [11]	—	218 [7]	10.4 [7]
c_p [J/gK] @ 300 K	1.116 [11]	1.055 [8]	1.026 [6]	0.903 [7]	0.765 [7]
c_p [J/gK] @ 800 K	—	2.144 [11]	1.863^a [8]	1.146 [7]	1.180 [7]
T_{mp} [K]	—	2350 [8]	723 [6,8]	933 [11]	2327 [11]
T_{bp} [K]	—	4137.895 [8]	2316 [8,10]	2791 [11]	3253 [11]
T_{ign} [K]	1073 [12]	1950 [10]	—	2327 [4]	—
H_{fus} [kJ/mol]	—	50.2±1.7 [8]	24.1±0.4 [8]	10.7±0.21 [8]	111.1±4 [8]
H_{vap}[kJ/mol]	—	480.344 [8]	—	294.001 [8]	—
MW [kg/kmol]	10.81 [11]	10.81 [11]	53.62 [11]	26.98 [11]	101.96 [11]

^{a} - at 723 K

The ignition and combustion of aluminum has been studied extensively by many researchers, including Roberts, et al. [4, 5], who conducted their shock tube experiments with a similar configuration used with the present boron research. The general aluminum ignition model is initially defined similar to the boron ignition model, in that an oxide layer forms during heating in an oxygen containing atmosphere. Before the aluminum melting point is reached, the aluminum expands and the oxide layer breaks apart allowing oxygen to reach the aluminum particle (Ref. [4]). The particle temperature increases up to the melting point of the oxide, which then retracts and allows vigorous reaction between the liquid aluminum particle and the oxidizer and the particle ignites. The liquid droplet has a detached gas phase envelope where the homogeneous combustion of the particle occurs. To complete the process, the product Al_2O_3 condenses out, releasing the additional enthalpy of vaporization.

Boron particle ignition follows a completely different process. After initial particle heat up, it is the oxide layer that begins to melt prior to any transformation of the boron particle. This allows the oxidizer to diffuse through the layer and react with the particle. This starts the ignition process. However, as stated earlier, the oxide layer builds up, retarding further oxidation. As the temperature increases, the oxide begins to evaporate, cooling the particle due to the endothermic evaporation process. At a certain point, the energy released from the chemical reaction exceeds the energy absorbed from evaporation and heat loss and the rest of the oxide will suddenly evaporate. This will extinguish the particle temporarily, which will then reignite and heterogeneously combust. It is difficult to achieve homogeneous gas phase combustion of the boron particle because the boiling temperature is so high, i.e. the combustion reaction consists mainly of surface reactions. Finally, the product B_2O_3 remains in the gas phase so the benefits of energy release from condensation are lost.

1.4 Goals of Current Research

Because the benefits of boron based combustion are apparent, research continues in order to eliminate the many drawbacks. There are numerous experiments reported which study the ignition process and attempt to establish a starting database for models. It is in models where important understanding of boron ignition and combustion can be exploited.

In 1982, King [1] reviewed several models and described a basic procedure a boron particle follows in order to complete its combustion. Figure 1.1 shows a schematic of a boron particle and some of the processes it goes through as it heats up. Notice that there are other species considered other than B, B_2O_3, and O_2. Some have theorized that these intermediate species, BO and BO_2, are the cause for the long ignition delays because they are slow to react to form B_2O_3 [13]. Others have considered that those species might not be intermediate but actually could be final products. In any case, it is agreed by many, including King, that the ignition of boron can occur sooner if the oxide layer was somehow removed quicker. Experimental evidence has shown that ignition delay is reduced in atmospheres containing water vapor [14, 15]. Other experiments have shown changes in ignition delay with atmospheres containing other compounds, such as

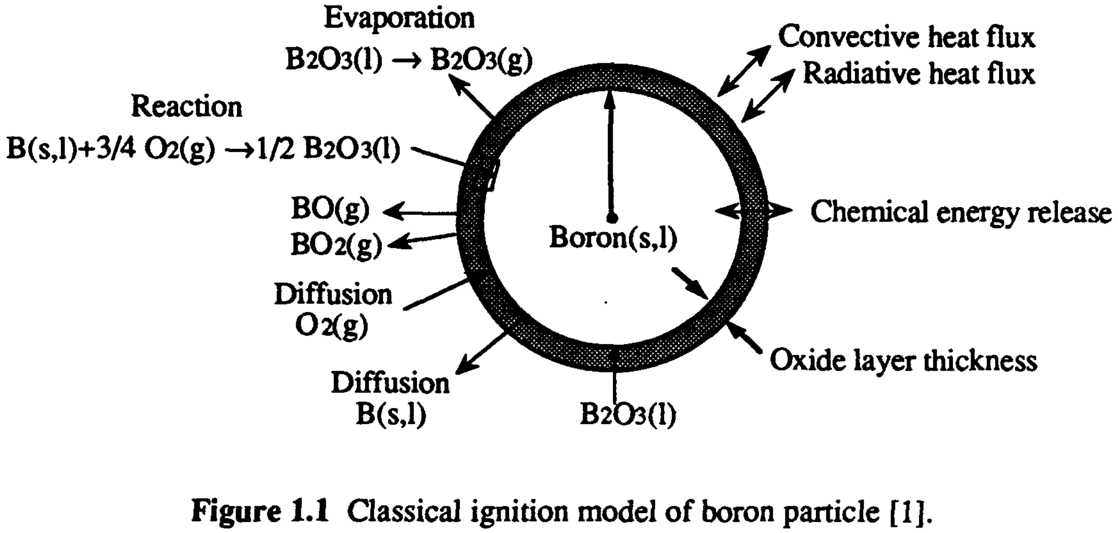

Figure 1.1 Classical ignition model of boron particle [1].

species containing fluorine [16]. Modelers have theorized that chemical reactions are taking place between the oxide and the different species, releasing gaseous products such as HBO_2 or possibly OBF. However, the models in this area are difficult to accept because there is very little experimental data to back them up.

1.5 General Overview

The focus of this research is to expand the boron ignition database to include results of boron igniting in oxygen at pressures ranging from 5-10 atmospheres and in gases containing fluorine/oxygen mixtures. Two types of fluorine containing species that are used are sulfur hexafluoride and hydrogen fluoride. The first compound is utilized to study the effects fluorine atoms on boron ignition. Fluorine atoms have been reported to increase energy output of boron combustion as well as reduce its ignition delay [17]. Sulfur hexafluoride, SF_6, dissociates easily at relatively low temperatures (< 2000 K) [34], so it provides an excellent and safe source of fluorine atoms. Hydrogen fluoride does not dissociate as easily, so the molecule itself must interact with the boron particle. It has been proposed that the HF molecule, because it contains both hydrogen and fluorine, which each separately are linked to reducing the ignition delay time, will reduce the particle ignition delay even further.

The experiments are conducted at these elevated pressures to extend the database and to compare the results with upcoming experiments to be performed in a closed vessel where ignition delays can be measured at pressures ranging from 100 to 1000 atmospheres. Pressure effects of boron igniting in pure oxygen atmospheres have been rarely studied and therefore could provide some insight for further research in this area.

A literature survey of previous experiments and models that has led to the current research is presented in Chapter 2. The discussion describes the conditions studied as well as the apparatus used to achieve the results. A brief overview of the results from all experiments is also presented. Current physical models as well as some of the underlying assumptions are described in some detail and compared to experimental data for validity. Finally, preliminary chemical kinetic modeling is presented to establish some of the groundwork behind the current investigation.

Chapter 3 describes the apparatus utilized in this research. A brief discussion of shock tube theory and operation is introduced, with emphasis placed on the handling of hydrogen fluoride. A description of the boron particles is given. A section is also included describing the data acquisition system and a sample ignition signal. A matrix of operating conditions, including particle size, pressure, and oxidizer type is also established.

Chapters 4 and 5 present and discuss the results of the research. Focus is on ignition delay time and how it is affected by temperature and oxidizer. A section describes burn times of boron. A discussion of error analysis and possible misinterpretation of the data is also included.

Chapter 6 concludes with a summary and recommendations concerning the analysis of the current data and suggestions for additional experiments that need to be conducted to fully understand the boron ignition phenomenon.

CHAPTER 2 - STATUS OF BORON COMBUSTION RESEARCH

Since the 1960's, researchers have been trying to explain the mystery of boron ignition delay and combustion. Experiments have yielded important results describing the physical characteristics of the ignition and combustion process. However, the incomplete understanding of boron and its oxide has led to different theoretical models for the mechanisms behind this delay process. Many researchers have attempted to model the physical aspect of how an oxidizer must breach the boron oxide layer to initiate the ignition process. However, it has not been until recently that the actual chemistry of the oxidizer reacting with boron and its oxide layer been studied in depth. Kinetic models have been developed to explain some of the experimental results, although these always seem to be incomplete. The motivation behind the present research is to answer some of the chemical kinetic questions by yielding experimental results of how boron reacts with different oxidizers. This section will survey the previous experiments and models that has contributed significantly to the current research.

2.1 Experimental Results

One of the first experiments done with crystalline boron combustion was conducted by Talley [19]. The method of his experiments was to heat cylindrical boron rods 1 mm in diameter in a stream of pure oxygen using electrical resistance within the rod. The temperature ranged from 1000 to 1900 K and pressures from 0.1 to 1 atm. He developed a generalized model of boron and oxide characteristics in certain temperature regions and predicted what are the rate limiting steps in each region. Most of the steps focused on how the boron oxide layer, B_2O_3, retarded the transport of oxygen to the clean boron surface. He also estimated the ignition temperature of boron by equating the heat generation by chemical reaction to the radiative heat loss. His result was calculated to be 2200 K. The heat generation was defined as the heat of formation of $B_2O_3(g)$ from B(s) and $O_2(g)$ and is an extremely simplistic model which does not completely describe the process. Experimentally, Talley found that boron rod started to burn at 1800 K.

Boron particle combustion, which is the focus of this research, was first studied by Gurevich, et al. [20] which utilized a jet of hot gas consisting of argon/oxygen or argon/water vapor to ignite particles which ranged in size from 75 to 200 microns. They observed that the boron combustion consisted of two zones; (1) a bright central core which corresponds to the heterogeneous combustion, and (2) a broad, blurred envelope which represents the homogeneous combustion in the vapor phase. They also observed trends in the ignition temperature, one was that the ignition temperature increased with decreasing particle size.

The Gurevich, et al. data showed that a 200 micron particle ignites at a temperature of approximately 1300 K while a 75 micron particle ignites at 1700 K, all for atmospheres containing

45% oxygen. They also observed that the ignition temperature increased with decreasing oxidizer mole fraction, for both oxygen and water vapor. Another trend indicated that using water vapor in place of oxygen increased the ignition temperature by up to 250 K.

Gurevich, et al., also did preliminary studies on amorphous boron ignition. Amorphous boron was stated to be agglomerations of small particles, on the order of hundreds of angstroms. They did discover that amorphous boron particles were able to ignite at lower temperatures than crystalline boron particles of the same size. The quoted ignition temperature for 25 micron particles in 100% water vapor was 1100 K. However, because the amorphous boron is actually an agglomerate of smaller particles, it is difficult to compare the two types of boron directly.

Gurevich, et al., were also one of the original researchers to find ignition delay and burn-times of boron. However, they only did these measurements in a water vapor/argon atmosphere. They did notice that ignition delay time decreased with increasing temperature. Figure 2.1 shows the results of ignition of a 145 μm diameter particle, d_o, in 36% water vapor atmosphere (C_{H_2O}). At one atmosphere pressure, P_∞, ignition delay was also found to increase with increasing particle size for a ambient gas temperature, T_∞, of 2400 K, as shown in Figure 2.2. They also noticed that burn time decreased with increasing oxidizer mole fraction.

Robert T. Uda [21] conducted experiments that found the ignition limit of particles at elevated pressures. He utilized a shock tube to ignite 30-50 micron agglomerates, which consisted

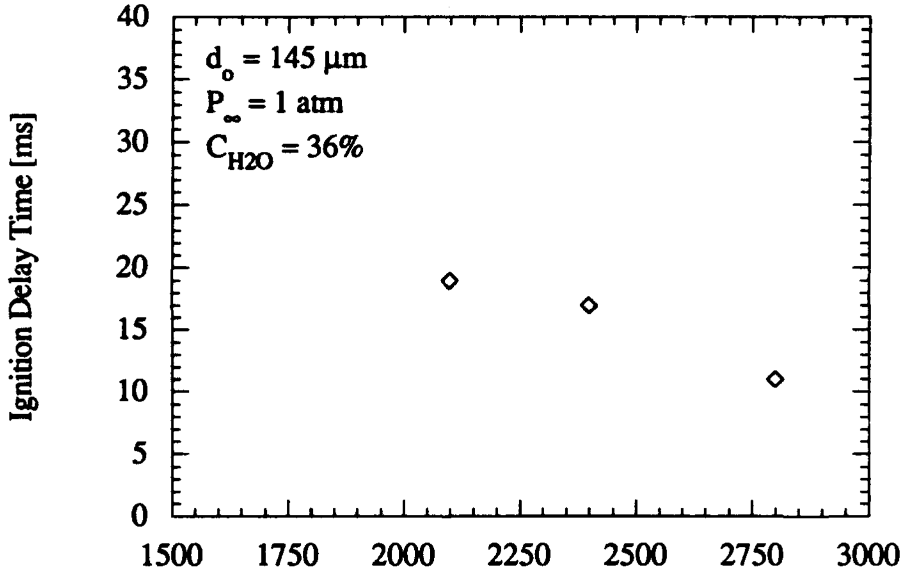

Figure 2.1 Ignition delay versus temperature data of 145 μm particle in .36/.64 water vapor/argon mixture at one atmosphere. Found by particle injection into a hot gas [20].

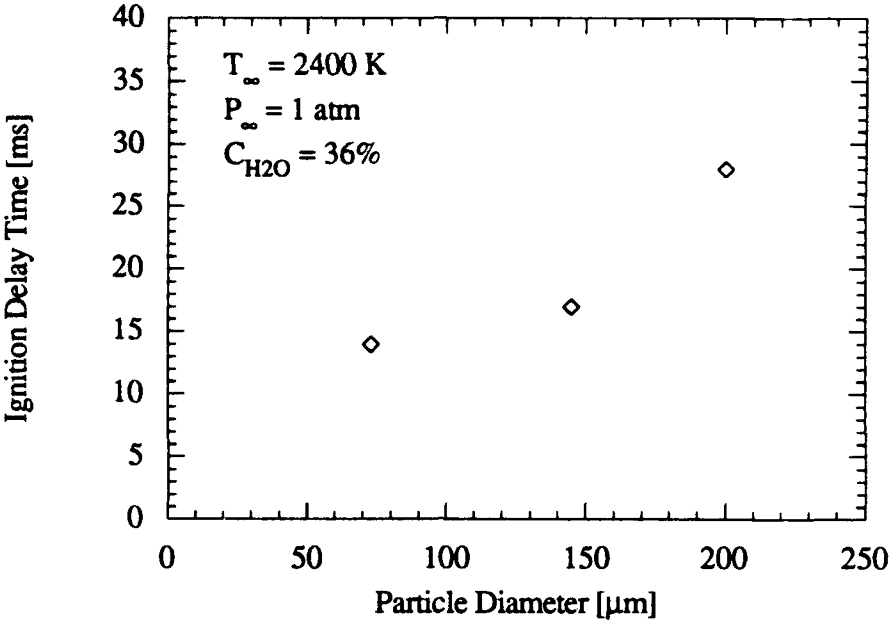

Figure 2.2 Ignition delay versus particle diameter data of particles in .36/.64 water vapor/argon mixture at one atmosphere at 2400 K. Found by particle injection into a hot gas [20].

of 1-2 micron particles, in air and at pressures up to 20 atm. He found the ignition temperature to decrease with increasing pressure (from 1900 K at 1 atm to 1400 K at 20 atm). He also did some limited ignition-delay time experiments on 0.015 micron particles, which only showed that it took less than 1 ms to ignite below 1400 K and less than 0.1 ms to ignite above that temperature.

Very significant boron combustion research were those experiments conducted by Macek and Semple [14]. Single particles of crystalline boron, which were separated into two samples having average diameters of 34.5 and 44.2 µm, were injected into a stream of hot oxidizing gas generated by a gas-burner at atmospheric pressure. The temperatures ranged from 1800 to 2900 K. They also varied the oxidizer mole fraction from 0.08 to 0.37 of oxygen, X_{O2}, and 0.00 to 0.21 of water vapor, X_{H_2O}.

During those experiments, they observed interesting characteristics of boron combustion. First of all, the structure of the boron flame consisted of a bright central core surrounded by a green envelope. Secondly, the boron combustion takes place in two stages, where the first stage consists of the particle igniting, burning for a short time and then extinguishing, and the second stage is the particle reigniting and burning to completion. They noticed that the two stages tend to merge when they use low oxygen mole ratios. As for the quantitative results, they observed ignition temperature to average out to be 1992±16 K when no water vapor was added and

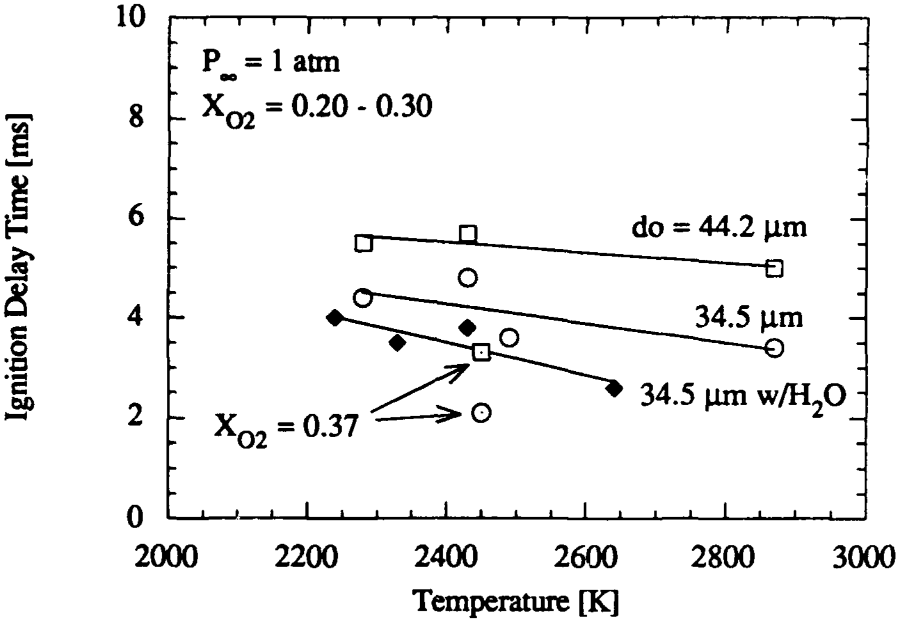

Figure 2.3 Ignition delay time as a function of temperature at one atmosphere. Delay measured with a flat flame burner from point of first glow to point of bright glow [14].

1860±24 K when the mole fraction of water vapor was between 0.16 and 0.21. Ignition delay times are plotted in Fig. 2.3. Ignition delay is defined as the time from the beginning of the first stage to the beginning of the second stage. Burning times for each stage of combustion were also measured and discovered to decrease with increasing temperature and mole fraction of oxidizer.

In a later study [22], Macek and Semple carried out combustion studies at elevated pressures and used a focused laser to energize the particle. At the lower pressures, below 10 atm, they were able to get reproducible data for ignition delay times but at higher pressures, their data was inconsistent. However, there is a definite trend that ignition delay increases with increasing pressure, at least in air. There was also a decrease in burn times with increasing pressure. They only reported one test case in pure oxygen and that was for a pressure of 1 atm, using a 75 μm particle heated up by the laser to an initial temperature, T_o, of 2000 K. The results were an ignition delay of 1.8 ms and a burn time of 6.8 ms. Figure 2.4 displays the results of those experiments. The error bars bound the scatter of his data.

In an even later work [16], Macek continued his experiments for different size particles. This time he used "spherical" particles, which were manufactured by the plasma-torch technique, to attempt to get more reproducible data. The same pressure trends were observed as in the previous work (see Fig. 2.5). As for trends due to the particle size, ignition delay showed little

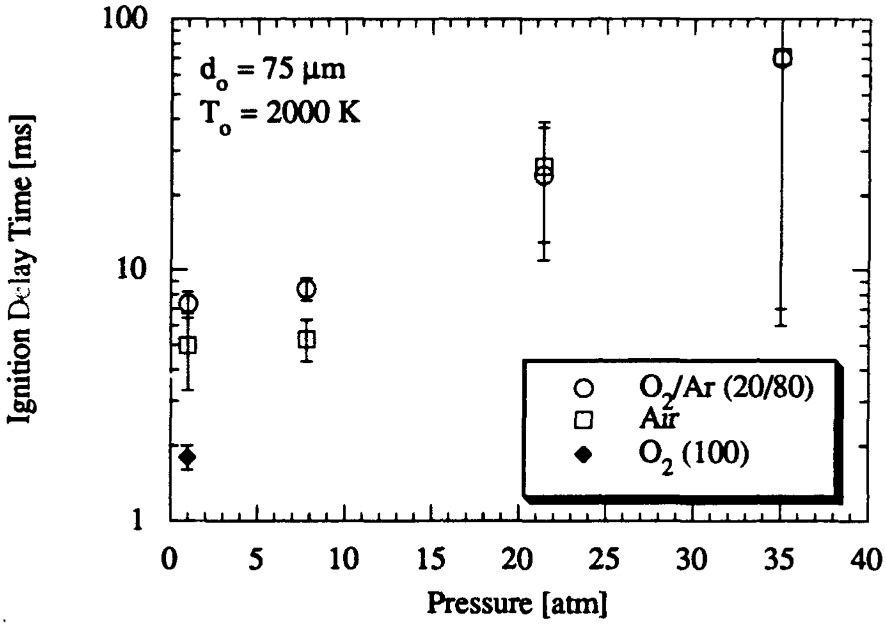

Figure 2.4 Ignition delay versus pressure for 75 micron particles. Error bars indicate scatter in the data [22].

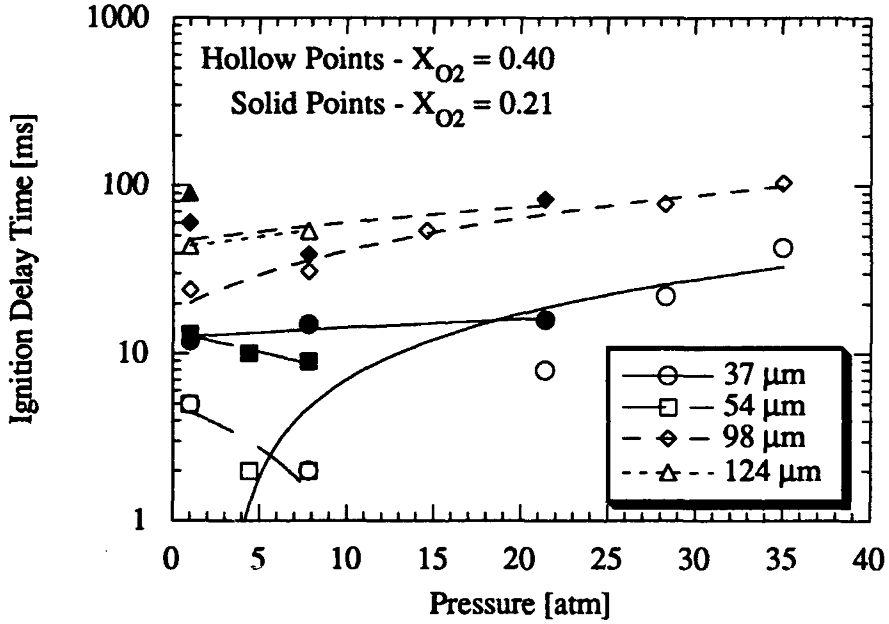

Figure 2.5 Ignition time versus pressure for laser-ignited particles heated up to 2000 K [16].

change when smaller particles were used (37 and 54 μm). However, for larger particles (98 and 124 μm), there was a significant increase in ignition delay with increasing particle size. This experiment also discussed the first attempts of using fluorine containing oxidizers. Using a nitrogen fluoride/argon mixture, they found that it increased the burn time, but little quantitative data was presented.

In a more recent effort, Li, Williams, and Takahashi [23] concentrated their efforts to study the kinetics of boron ignition. A flat flame burner with a steady nitrogen jet injecting 0.04 to 0.15 μm particles were utilized in that study. At temperatures below 1800 K, a dark yellow plume with dark brown smoke was observed emanating from the flame tip. Between 1800 and 1900 K, a yellow flame was surrounded by green emission around the lower part of the flame. Above 1900 K, the flame became bright yellow and was completely surrounded by bright green radiation. Using spectrographic analysis, they determined that the green radiation corresponded to BO_2 emissions from the boron combustion products while the yellow band represented boron ignition. They measured the ignition time according to the height and flow rate of the flame, their data is graphically presented in Fig. 2.6.

Finally, Yuasa and Isoda [24] studied spontaneous ignition and combustion of boron lumps by impinging an oxygen jet upon a 5 to 8 mm lump of boron. All experiments were at atmospheric pressure and the particle was heated using a xenon lamp. Ignition temperature was

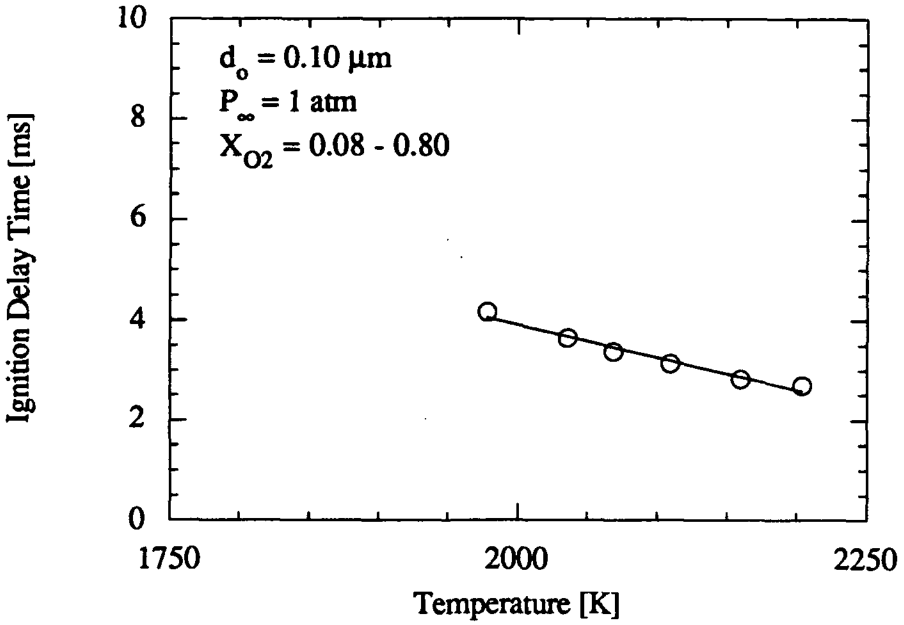

Figure 2.6 Ignition delay versus temperature for sub-micron particles in a flat flame burner. Experiments conducted at one atmosphere were independent of oxygen concentrations [23].

found to be 1580 K and the delay was between 200 and 400 ms. They also found a minimum oxygen mole fraction necessary for ignition, namely 0.3. They also observed the green envelope around the lump, which was found spectroscopicly to be both BO and BO_2. They even determined that the amount of BO decreases as distance from the particle increases, which indicates that BO is formed on the liquid boron surface by surface reactions. BO_2 has a maximum intensity some distance away from the boron lump surface which means that BO_2 is formed in the gas phase. Finally, it was noticed that no B_2O_3 was evidenced on the surface of the particle but was the sole product after complete combustion. Based on these findings, an improved chemical kinetic model was suggested, which will be discussed later in this chapter.

2.2 Physical Modeling Research

Mohan and Williams [10] carried out research utilizing laser ignition of both crystalline and amorphous boron particles, but minimal quantitative results were presented. They concentrated on modeling the process. They developed two models to explain two stages of boron combustion. The first stage, the low temperature stage where a solid boron particle is coated with a liquid oxide layer, involved modeling of the regression rate of the boron oxide layer due to diffusion controlled reaction at the solid particle surface and vaporization of the oxide to the atmosphere. The steady state condition of this model successfully predicted the ignition temperature that both Talley [19] and Macek and Semple [14] had found experimentally.

The second stage of combustion was the high temperature combustion process, where the boron has liquefied and the oxide layer has evaporated. The modeling consists of gas phase diffusion of O_2, B_2O_3, and B_2O_2. This is one of the first studies that has taken into account that the oxide layer, B_2O_3, can react with the boron. The model predictions compared well with Macek and Semple's gas-burner experiments [14].

One of the more considerable modeling efforts was performed by King [1]. Although there have been other researchers to develop different models, they all seem to agree on the same basic concept. The first is that the boron particle is initially coated with a solid oxide layer. Then as heat-up begins, solely by radiation or convective heat fluxes, the oxide layer begins to melt. For the boron to react, the oxygen or oxidizer must diffuse through the liquid boron oxide layer. The oxidation of the boron will then cause the oxide layer to thicken, increasing the diffusional resistance of the oxygen through the oxide layer. However, the oxidation of the boron is exothermic, so this will add to the heat-up of the particle and the particle's oxide layer. The temperature increase of the oxide layer will reduce its viscosity and therefore will increase the diffusion rate. Meanwhile, the oxide layer will begin to evaporate, reducing the oxide layer's thickness and cooling the particle. Also, the gaseous oxide must diffuse away from the particle for ignition to proceed to combustion. If the particle temperature continues to rise, the oxide layer will thin to a layer where temperature runaway will occur and full fledged combustion will begin.

Most who have modeled the ignition of boron [1, 10], including King, assume that the diffusion of the oxygen through the liquid is the rate limiting step. King also attempts to model the gas diffusion of the oxide and the kinetic resistances along with the liquid diffusion, but those resistances do not become important until the oxide layer has become very thin. However, he does suggest, along with others, that to decrease the ignition delay, the oxide layer must be removed more rapidly than what occurs normally in oxygen atmospheres.

King also summarized some of the previous research done to promote ignition. Childs, King, and Martin [25] combined boron with aluminum/magnesium in propellant and found improved efficiencies over boron-only propellants. They postulated that the improvements came from the intense radiation flux from the additives. They also attempted and succeeded in improving the removal of the oxide layer by coating the boron particles with lithium fluoride, which is hypothesized to reduce the boiling temperature of the boron oxide. Finally, they are quoted to have used fluorinated oxidizers and that this also increased efficiency, which they presumed was caused by the reaction of hydrogen fluoride with the boron oxide. Although no actual data was tabulated, fluorine compounds appeared to be beneficial to boron ignition.

Dirk Meinkohn [26] expands on King's model and determines the ignition temperature for boron. By equating rates of oxide formation and evaporation, he determines the ignition temperature to be 1900 K, which compares favorably to previous experimental work and also strengthens King's assertion that the oxide layer must be removed for ignition to occur. Meinkohn's model also implies that an increase in pressure and/or a decrease in particle size would decrease the ignition temperature, which agrees well with Macek's data.

Glassman, Williams, and Antaki [13] attempted to model boron ignition from a different approach. Instead of assuming that oxygen diffuses through the oxide layer to the boron, they assume that boron diffuses out toward the boron oxide/gas interface and reacts there. After calculating diffusion rates, they concluded that this model is a viable alternative because, for one, the diffusion rate of boron across the oxide layer is much higher than boron oxide vaporization rates and therefore is not a limiting factor in the ignition process. They also estimated solubilities of oxygen and boron in the oxide and found that boron was more soluble. Diffusion rates were found to be the same for boron and oxygen but actual oxygen flux through the oxide is negligible compared to boron flux.

Li and Williams [15] expanded this model but added the chemical kinetic effects water vapor plays on boron ignition and combustion. They have chosen to model the process as four steps, with a fifth step necessary for ignition in water vapor. The first step, which many modelers agree with, is the evaporation of the oxide, which is endothermic. The next step is the reaction at the particle surface between boron and oxygen. This is an exothermic process. The third step, which involves numerous chemical reactions, can be summarized as an exothermic reaction between boron, boron oxide, oxygen, and water vapor within the oxide layer. The final step is the combustion of the boron after the oxide layer has been completely removed. This step only involves surface reactions between the boron particle and oxygen. The fifth step, which has not been examined thoroughly, would augment the removal of the oxide if in atmosphere containing water vapor by having the oxide react with the water vapor to form gaseous HOBO. This model compared well with their experimental results discussed in Section 2.1 above.

An interesting experiment conducted by Zvuloni, Gomez, and Rosner [27] examined the reactivity of solid boron with O_2, H_2O, CO_2, and B_2O_3. The surprising result was that the boron oxide was a considerably more efficient reactant for gasifying boron at high temperatures than the other reactants. They conclude that at one atmosphere, particles between 3 and 30 microns would undergo kinetically limited combustion governed by the boron oxide/boron reaction. For smaller particles, they estimated the reaction would be controlled by the oxygen/boron reaction, which would reduce the gasification rate by a significant factor of 2 to 3 times.

2.3 Kinetic Modeling Research

The evolution of the boron ignition and combustion physical model has led to one major conclusion and that is that the ignition of boron is limited to the rate that the oxide is removed. The models also indicate that oxide removal appears to be kinetically limited, which would appear to be true when water vapor accelerates the ignition process. This section reviews the latest research conducted on the investigation of boron kinetics.

A study of boron kinetics in oxygen atmospheres was done experimentally by Yuasa and Isoda [24]. As stated earlier, during boron ignition, they found regions above the boron surface that consisted of certain types of products. They developed the kinetic scheme shown in Table 2.1 from those results. Although, this schematic defines certain steps that arise during ignition of boron, it does not indicate which step is the limiting one or which steps are dominant, or which are necessary, if boron ignition delay reduction is to be investigated.

Another step toward the investigation of the kinetics of boron combustion is presented by Li and Williams [15]. The main steps in their model as stated earlier are actually comprised of many kinetically controlled steps. They define which of their reactions are the rate limiting steps but there are uncertainties because not all of the steps have been accurately tested. Some of these steps have estimated rates from the basis of other rate data.

However, some conclusions can still be reached. Most of their kinetics investigation is centered around the heterogeneous reaction of the solid boron with oxygen or water vapor or the

Table 2.1 Kinetic reaction scheme proposed by Yuasa and Isoda [24].

Reaction Type	Reaction	Heat of Reaction [kJ/mol]
Surface Reactions	$B(l) + B_2O_3(g) \rightarrow 3\ BO(g)$	811.6
	$B(l) + BO_2(g) \rightarrow 2\ BO(g)$	262.5
	$B(l) + O \rightarrow BO(g)$	-271.3
Gas Phase Reactions	$BO(g) + O_2 \rightarrow BO_2(g) + O$	-35.2
	$BO(g) + BO_2(g) \rightarrow B_2O_3(g)$	-589.0
	$BO_2(g) + BO_2(g) \rightarrow B_2O_3(g) + O$	-14.99
	$B_2O_3(g) \rightarrow B_2O_3\ (l)$	-419.2
	$O + O + M \rightarrow O_2 + M$	-498.6

oxide layer. Their model for boron surface reaction with oxygen and oxide contains the same steps as the model of Yuasa and Isoda [24], which they summarize to the following overall exothermic reaction:

$$B(s) + O_2(g) \rightarrow BO_2(g) + Q \tag{2.1}$$

where Q is 68±2 kcal/mol. They do state that the slowest kinetic step is $BO + O_2 \rightarrow BO_2 + O$ and that it occurs within the oxide layer. However, since the step has a low energy, BO_2 cannot be liberated as a gaseous product. Li and Williams add the final step (Equation 2.2) to their kinetic reaction, which is highly energetic and produces gaseous BO_2.

$$O(a) + BO(d) \rightarrow BO_2(g) \tag{2.2}$$

The symbol (d) signifies dissolution in the liquid oxide and (a) represents adsorption on the oxide surface.

When water vapor is added, the chemistry changes and a new rate limiting reaction occurs. The overall reaction becomes

$$4/3\ B(s) + 4/3\ B_2O_3(l) + 2\ H_2O(g) + O_2(g) \rightarrow 4\ HOBO + Q \tag{2.3}$$

where Q is 21 kcal/mol. This reaction accelerates ignition compared to the dry gas reaction by removing $B_2O_3(l)$ in the process. The slowest kinetic step in this process is similar the dry gas limiting step in that it involves BO and the oxidizer (Equation 2.4).

$$BO(d) + H_2O(g) \rightarrow HBO(a) + OH(a) \tag{2.4}$$

The other steps that produce the final product are given in Table 2.2.

Table 2.2 Chemical kinetic reactions for homogeneous combustion (Li and Williams [15]).

Reaction
$HBO(a) \rightarrow BO(d) + H(a)$
$H(a) + O_2(g) \rightarrow OH(a) + O(a)$
$O(a) + H_2O(g) \rightarrow 2\ OH(a)$
$OH(a) + BO(d) \rightarrow HOBO$

The most considerable effort into modeling the kinetics of boron combustion is done by Yetter, et al. [3]. They investigated the homogeneous gas phase chemistry of boron with hydrocarbons at temperatures ranging from 1800 to 3000 K. They tested fuel rich and fuel lean systems and did sensitivity analysis to determine the critical reactions involved. They concluded that for fuel rich systems, HBO, B_2O_2, and BO are the dominant equilibrium species in the boundary layer surrounding the boron particle. For oxygen rich systems, HBO_2, B_2O_3, and BO_2 dominate. HBO_2 and B_2O_3 are the two main combustion products where the latter is favored at higher temperatures. With these results and a sensitivity analysis of reaction rates of 58 steps, a small set of kinetic reactions dominate, which are given in Table 2.3. Their final conclusion is that the initial reactants, which influences the oxidation chemistry for very short time periods (on the order of 1 μs), have only a slight affect on subsequent oxidation chemistry, meaning that the initial reactants did not need to be precisely known in order to conduct the homogeneous gas-phase chemical analysis.

In a later paper by Pasternack [28], the gas-phase chemical model was updated to include recent experimental measurements of thermodynamic and kinetic data. The author also concluded that the species HOBO was one of the main products and also that the radical HBO dominates as well. These results came from an entirely different set of dominant reactions (see Table 2.4) and indicated that equilibrium temperature rise was slower compared to Yetter's model. It would appear that from this model, more species must be studied in order to understand boron ignition.

Further research by Brown, et al.[29] continued the kinetic modeling by utilizing the homogeneous model reactants to help model the boron oxide heterogeneous reaction. They discovered, by placing certain criteria on the reactants, that the three species, O, OH, and H_2O, seem to be the only reactants which contribute to the gasification of B_2O_3. The reactions that were proposed to be significant or responsible are shown in Equations 2.5, 2.6, and 2.7. Brown, et al. also did some modeling on gasification rates of boron oxide in relation to temperature and particle size. One result was that for boron oxide droplets smaller than 200 μm at 1800 K, the surface

Table 2.3 Critical elementary reactions for high temperature boron/hydrocarbon homogeneous combustion (Yetter, et al. [3]).

	Oxygen-rich reactions
HBO reactions	$HBO + OH \rightarrow BO + H_2O$
	$HBO + O \rightarrow BO + OH$
	$HBO + O \rightarrow BO_2 + H$
	$HBO + H \rightarrow BO + H_2$
	$HBO + M \rightarrow BO + H + M$
BO reaction	$BO + OH \rightarrow BO_2 + H$
BO_2 reactions	$BO + O_2 \rightarrow BO_2 + O$
	$BO_2 + CO \rightarrow BO + CO_2$
HBO_2 reactions	$BO_2 + H + M \rightarrow HBO_2 + M$
	$BO_2 + H_2O \rightarrow HBO_2 + OH$
	$BO_2 + OH \rightarrow HBO_2 + O$
	$BO_2 + H_2 \rightarrow HBO_2 + H$
	$HBO + OH \rightarrow HBO_2 + H$
B_2O_3 reactions	$BO_2 + BO_2 \rightarrow B_2O_3 + O$
	Fuel Rich Reactions
B_2O_2 reactions	$BO + HBO \rightarrow B_2O_2 + H$
	$BO + BO + M \rightarrow B_2O_2 + M$
	$BO + HBO_2 \rightarrow B_2O_2 + OH$

$$B_2O_3 + O(g) \rightarrow 2\ BO_2(g) \tag{2.5}$$

$$B_2O_3 + OH(g) \rightarrow HOBO(g) + BO_2(g) \tag{2.6}$$

$$B_2O_3 + H_2O(g) \rightarrow 2\ HOBO(g) \tag{2.7}$$

reactions are kinetically limited and the gasification rate is proportional to droplet diameter. For larger droplets, the surface reactions are diffusion limited and are independent of droplet diameter.

2.4 The Role of Fluorine Additives

From all modeling completed to date, it can be concluded that the kinetically limited gasification of the boron oxide is also the limiting factor of boron ignition. Physical models, experimental results, and kinetic analyses indicate that certain additives in the oxidizer would improve ignition. However, up to this study, only water vapor has been studied in detail. Some

Table 2.4 Updated critical elementary reactions for high temperature boron/hydrocarbon homogeneous combustion (Pasternack [28]).

Reactions
$HBO + O_2 \rightarrow HBO_2 + O$
$BOH + O_2 \rightarrow HBO_2 + O$
$HBO + OH \rightarrow HBO_2 + H$
$HBO + OH \rightarrow BO + H_2O$
$BO + O_2 \rightarrow BO_2 + O$
$BO + H_2 \rightarrow HBO + H$
$BO + H_2 \rightarrow BOH + H$
$BO_2 + CO \rightarrow BO + CO_2$
$B_2O_2 + H \rightarrow BO + HBO$
$B_2O_2 + H \rightarrow BO + BOH$
$B_2O_2 + O \rightarrow BO + BO_2$
$B_2O_2 + OH \rightarrow BO + HBO_2$
$H + O_2 \rightarrow OH + H$
$H + H_2O \rightarrow OH + H_2$
$O + H_2 \rightarrow OH + H$

previous experiments dealt with fluorine containing compounds and showed some beneficial results but there has not been any follow-up or explanation until recently.

Brown et al. [29] have started investigating the advantages of boron/fluorine systems. One benefit is that the reaction $B(s) + 3/2\ F_2 \rightarrow BF_3(g)$ has considerable higher heats of reaction compared to $2\ B(s) + 3/2\ O_2 \rightarrow B_2O_3(l)$ (-105.1 and -58.0 kJ/g, respectively). Another benefit from this comparison is that the latter reaction requires condensed products to achieve full energy release while the former does not. They also state that gas phase oxidation and heat release rates are increased when fluoride is added to the oxidizer mix. Initial modeling has also shown substantially different kinetic pathways and combustion products because the equilibrium kinetics favor OBF and BF_3 over HOBO and B_2O_3. They also propose that hydrogen fluoride promotes gasification of the oxide. From these calculations, fluorine would be the ideal candidate for promoting boron ignition.

2.5 UIUC Research Overview

The conclusions reached by Brown, et al. [29] has led our University of Illinois research group to investigate the actual behavior of fluorine compounds with respect to boron ignition. To examine this phenomenon, experiments are conducted with sub 50 micron crystalline boron particles in a shock tube, which allows temperatures to range from 1600 to 3000 K and pressures to range from 8.5 to 35 atmospheres. The scope of the research is to determine the ignition delay time of boron in fluorine/oxygen and hydrogen fluoride/oxygen atmospheres and to establish another independent set of ignition delay/burn time data for reaction in pure oxygen and oxygen/water vapor mixtures. The data with fluorine additives is compared to oxygen and water vapor/oxygen results to determine if fluorine is a beneficial additive. Temperature trends of boron ignition are also investigated. The results from this study should bring researchers one step closer to solving the problem of boron combustion.

CHAPTER 3 - EXPERIMENTAL TECHNIQUE

The experiments were conducted in the Shock Tube and High Pressure Combustion Laboratory located in Talbot Laboratory at the University of Illinois at Urbana-Champaign. The experiments consisted of igniting and combusting sub 50 micron boron particles with various oxidizers in a shock tube. Most of the procedures used were developed by the engineers who designed and constructed the laboratory and equipment [4, 30], although the entire apparatus was removed from one laboratory scheduled for demolition and completely reinstalled in a new laboratory. The procedure was updated to also include the handling of hydrogen fluoride. The general guidelines of the procedure will be given with detailed descriptions of all the modifications necessary to conform to the specific experiments.

3.1 Shock Tube

3.1.1 Theoretical calculations

The ignition and combustion of boron is studied in the high temperature and high pressure region of gas produced by a reflected shock wave within a shock tube. This region of gas is well suited for particle combustion studies since the flow velocity is nearly zero. The main limitation behind this technique however, is the short duration of the test conditions due to the arrival of pressure disturbances from the interaction of the reflected shock wave and the endwall. A complete discussion of the duration of the test condition is presented in Appendix A. If the experiment is conducted within the test time, specific desired conditions are readily obtainable since they are based on the initial conditions in the shock tube, which can precisely set.

To create the desired conditions, the shock tube is filled with a high pressure gas on one end, the driver section (condition 4), and a low pressure gas on the other end, the driven section (condition 1). All conditions are depicted in Fig. 3.1. These conditions are calculated in the following way, assuming an ideal gas with constant properties [32, 33]. Given the desired final conditions desired (condition 5) and the initial temperature of the driven gas, which is usually taken to be room temperature, the Mach number of the incident shock wave can be found iteratively using Equation 3.1.

$$\frac{T_5}{T_1} = \frac{\left[\left(\frac{3\gamma_1 - 1}{\gamma_1 - 1}\right) M_1^2 - 2\right]\left[2M_1^2 + \frac{3 - \gamma_1}{\gamma_1 - 1}\right]}{\left(\frac{\gamma_1 + 1}{\gamma_1 - 1}\right)^2 M_1^2} \tag{3.1}$$

With this value, the initial driven pressure can be found by using Equation 3.2 as well as the pressure ratio of the incident shock wave by using Equation 3.3.

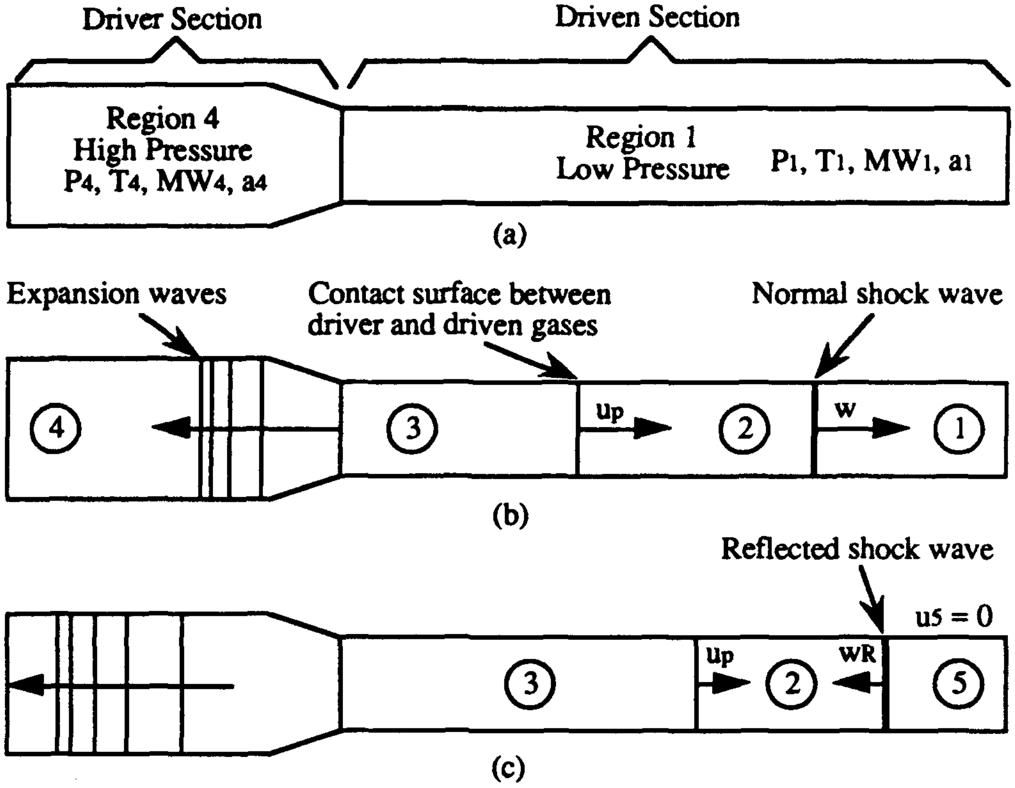

Figure 3.1 *Conditions in a shock tube* (a) *initially*, (b) *after diaphragm is broken*, and (c) after shock wave reaches endwall [33].

$$\frac{P_5}{P_1}=\left[\frac{\left(\frac{3\gamma_1-1}{\gamma_1-1}\right)M_1^2-2}{M_1^2+\frac{2}{\gamma_1-1}}\right]\left[\frac{\left(\frac{2\gamma_1}{\gamma_1-1}\right)M_1^2-1}{\frac{\gamma_1+1}{\gamma_1-1}}\right] \tag{3.2}$$

$$\frac{P_2}{P_1}=\frac{2\gamma_1 M_1^2-(\gamma_1-1)}{\gamma_1+1} \tag{3.3}$$

With this pressure ratio, the initial pressure in the driver section can be found by the relation

$$P_4=P_1\frac{P_2}{P_1}\left\{1-\frac{(\gamma_4-1)(a_1/a_4)(P_2/P_1-1)}{\sqrt{2\gamma_1\left[2\gamma_1+(\gamma_1+1)(P_2/P_1-1)\right]}}\right\}^{-2\gamma_4/(\gamma_4-1)} \tag{3.4}$$

where the speed of sound, *a*, is defined as

$$a=\sqrt{\gamma(R_u/MW)T} \tag{3.5}$$

From Equation 3.4, the incident shock could be increased if a_1/a_4 is decreased. To implement this, a heavier gas is used in the driven section (e.g. oxygen) and a lighter gas (e.g. helium) in the driver section.

Relations 3.1 to 3.4 assume an ideal, constant composition gas. For real gases, densities and heat capacities are strong functions of temperature. Also chemical reactions will take place, changing the type and amount of gases in the shock tube as well as divert the energy created by the shock wave from heating up the gas. To calculate the conditions for a real gas, the NASA Equilibrium Gas Composition Program [34] and a computer program developed by Roberts [18] was utilized. The final conditions are entered and the operating parameters, P_4, P_1, and the incident Mach number, are calculated. Further discussion on actual operating conditions follows in Section 3.4.

3.1.2 Laboratory set-up

A schematic of the shock tube used is shown in Figure 3.2. The driven section, where the particles are ignited, is a 8.4 meter (27.5 foot) stainless steel tube, that is 8.9 cm (3.5 inches) in diameter. This is coupled to a 3.3 meter (10 foot) long, 16.5 cm (6.5 inch) diameter stainless steel driver section by a converging nozzle and a diaphragm section. A converging section provides an efficient steady expansion and also reduces the driver pressure necessary to produce the test conditions compared to a constant area shock tube [35]. The tube uses the dual diaphragm technique. Two layers of diaphragms separate the high pressure driver section from the low pressure driven section, with an intermediate pressure contained between the two layers. The diaphragm section is then vented to the atmosphere, creating a pressure difference between this section and the driver section large enough to burst the diaphragms, firing the shock tube. Each diaphragm layer consists of a number of 0.25 and 0.125 mm thick sheets of Mylar. The desired final conditions determine the initial pressures in all sections which, in turn, determine the number of Mylar sheets that will separate the driven and driver sections. For all tests, helium is used to pressurize the driver and diaphragm sections. The driven section contains the desired oxidizer, usually oxygen mixed with other species.

The boron particles are installed near the endwall of the driven section. The endwall consists of a quartz window and a polycarbonate window so the radiation emitted can be measured. It also consists of a hobby knife blade where the particles are held by electrostatic charge build-up. The blade is 8 mm from the endwall so the powder has a chance to be blown off the knife blade and to ignite due to the hot, surrounding gases. The particles are blown off the blade by the high velocity flow behind the incident shock wave and are accelerated toward the endwall. After the reflected shock passes, the particles drift in the stagnant gases and collide and reflect off the endwall. The particles are then dispersed and ignited. Figure 3.3 illustrates the

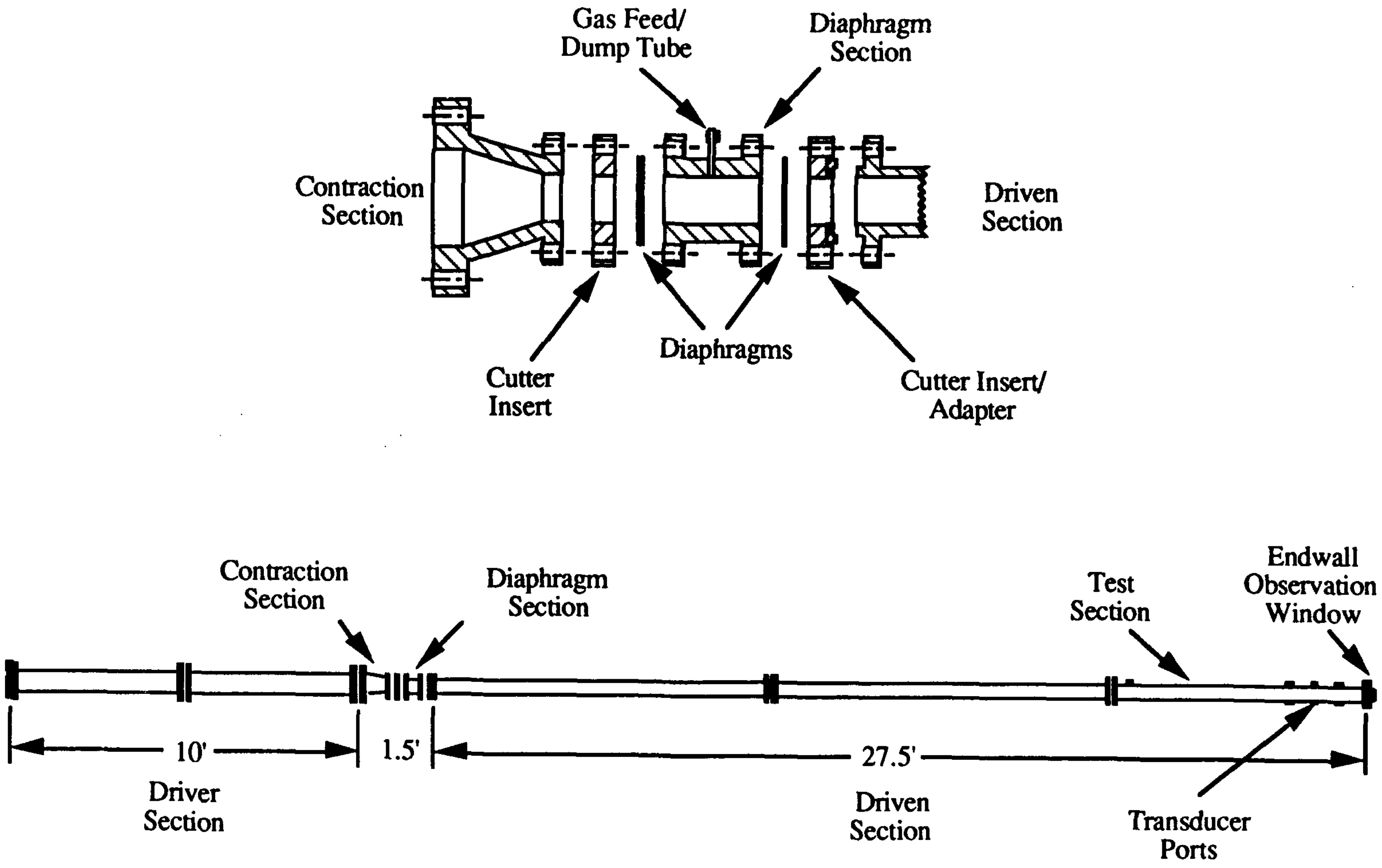

Figure 3.2 Helium driven shock tube with a double diaphragm firing system.

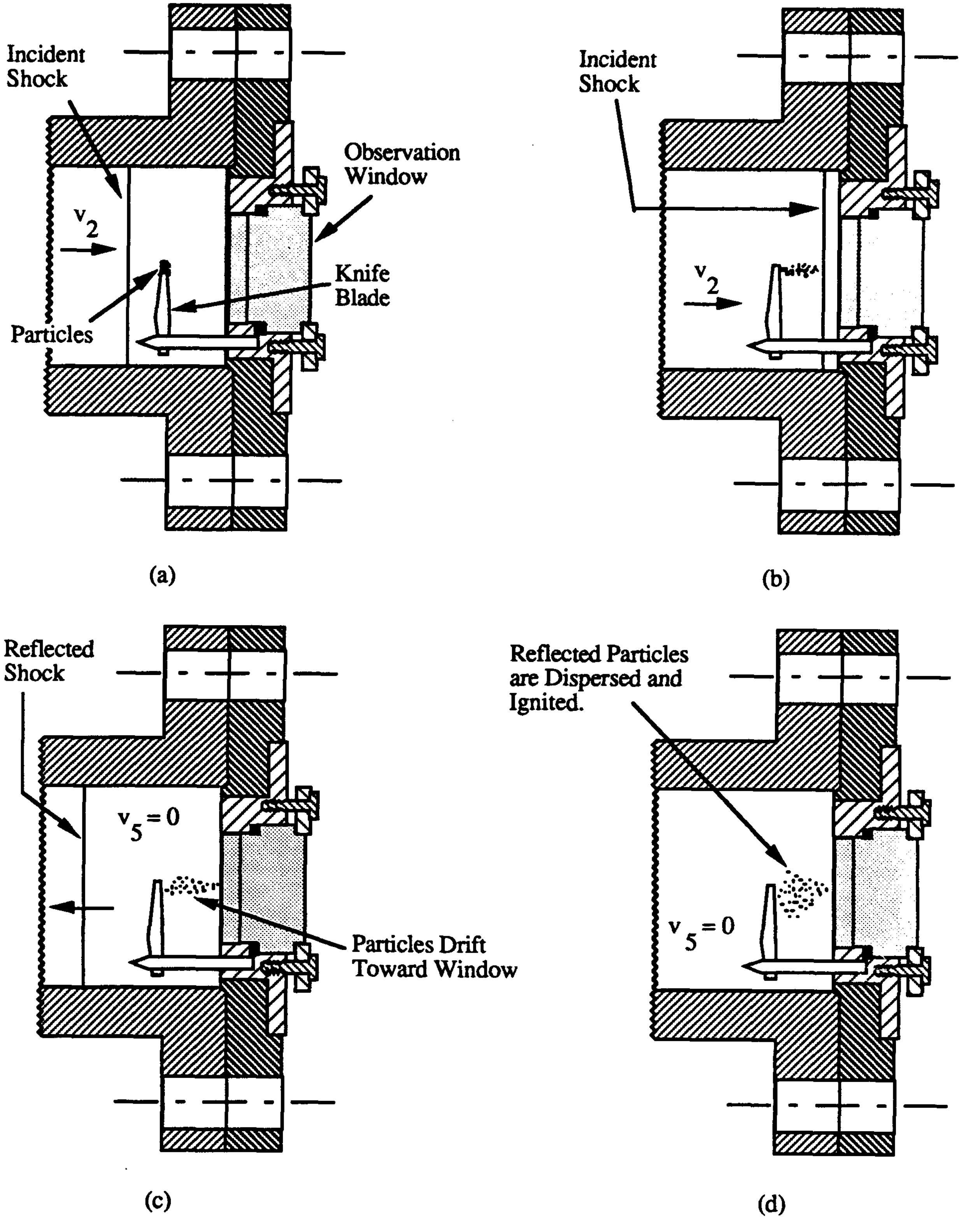

Figure 3.3 Particle mounting technique and particle dispersal from incident and reflecting shock waves. Knife blade is located 8 mm from endwall.

technique. The particles are considered dispersed enough that the radiation from a hot particle does not contribute to the heating of the other particles. This would make the ignition time independent of the number of particles installed [4].

3.1.3 Gas handling procedure

After the boron is installed the shock tube must be pressurized. The procedures are different for the various driven section gases. A general procedure, developed by Roberts [5], is utilized for oxygen installment. Procedural adjustments are made when water vapor, sulfur hexafluoride, or hydrogen fluoride are added. The general procedure and the modifications are discussed in general for oxygen, water vapor, and sulfur hexafluoride. A more detailed presentation is made for handling hydrogen fluoride vapors, discussing the dangers and limitations involved in its use.

3.1.3.1 Oxygen, water vapor, and sulfur hexafluoride

The pure oxygen installment procedure is similar to the oxygen mixtures with water vapor and sulfur hexafluoride installment procedure so all discussions will refer to the piping diagram given in Fig. 3.4. Table 3.1 enumerates the basic steps involved in the procedure for oxygen.

Table 3.1 General procedure for the installment of oxygen in the driven section of the shock tube.

Step	Instruction
1	Evacuate the driven section of air with the Marvac Scientific Manufacturing Company high pressure vacuum pump.
2	Read and record absolute vacuum from the vacuum gauge within the control room. This will be the zero reading for future pressure measurements.
3	Pressurize driven section with oxygen up to 345 kPa from the control room. This is done so there is pure oxygen in the shock tube. Previous calculations indicate the driver gas composition is 98.6 percent oxygen [5].
4	Vent off driven section to the room until just above atmospheric pressure is reached.
5	Evacuate driven section to desired pressure.
6	Record initial temperature.
7	Reset data acquisition system.
8	Fill driver and diaphragm section with helium the diaphragm pressure reaches half the desired driver pressure. Close off diaphragm section.
9	Fill driver section to desired pressure.
10	To fire the shock tube, evacuate the diaphragm section from the control room.

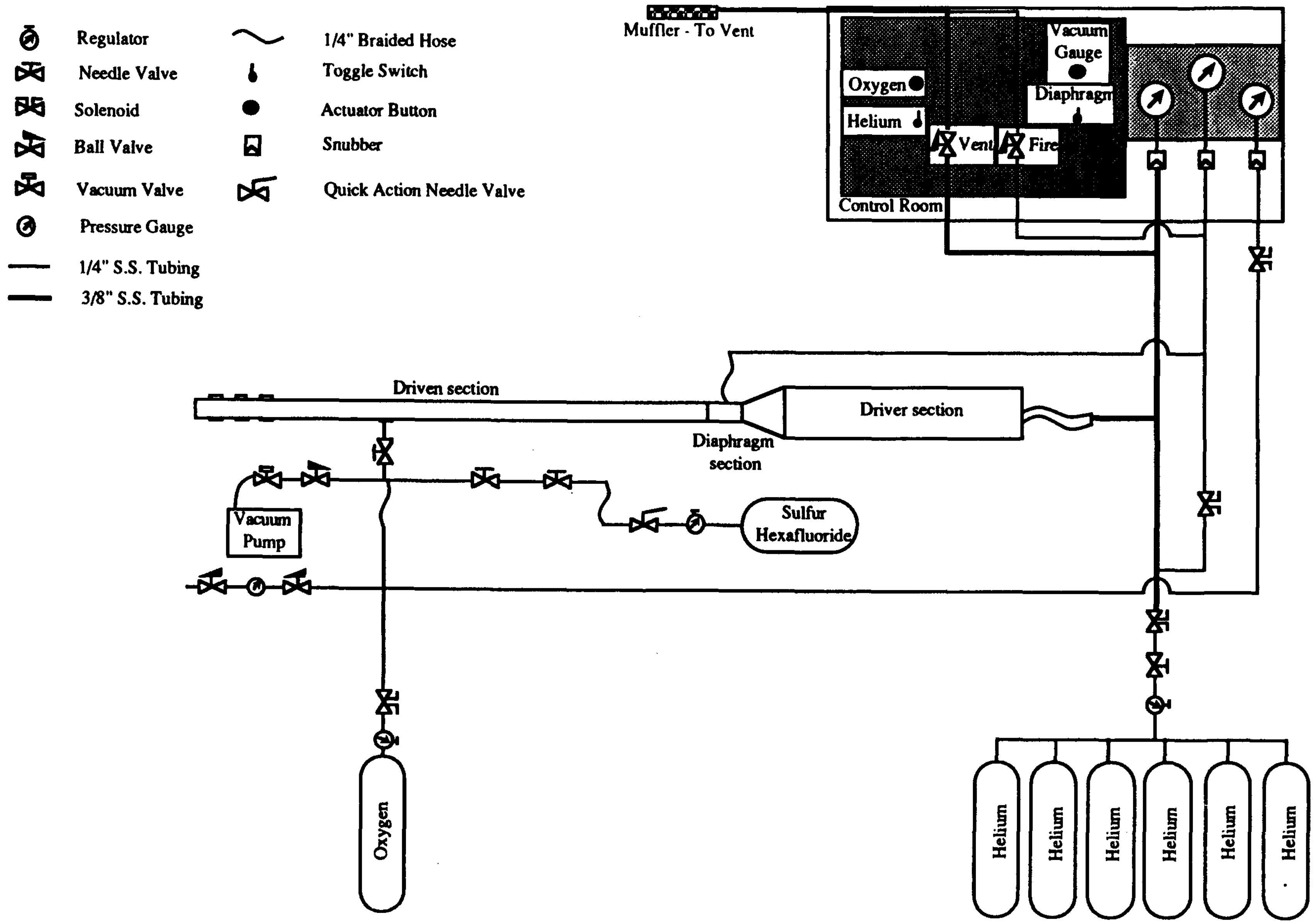

Figure 3.4 Piping layout for oxygen, water vapor, and sulfur hexafluoride installment.

Further details of this procedure are given in Ref. [5].

The procedure for mixed water vapor and oxygen was developed by Megli [31] but Megli used mixtures of water vapor and argon. After the tube has filled with oxygen to 345 kPa and vented down, the tube is evacuated back down to absolute vacuum instead of the initial oxygen partial pressure. Once completely evacuated, distilled water is installed between two interlocking ball valves, which are located just downstream of the quick action needle valve for the sulfur hexafluoride. as shown in Fig. 3.4. The lower valve is opened to evaporate the water into the shock tube [illegible] necessary for the tube to be at complete vacuum in order to evaporate the water easily. Two or three drops produce approximately 0.1 kPa partial pressure in the shock tube. Drops of water are continuously added until the desired water partial pressure is reached. Then oxygen is regulated into the tube by way of the push button solenoid until its partial pressure is reached. Again, helium is filled into the driver section and the shock tube is ready for firing.

Sulfur hexafluoride is installed in a procedure similar to the water vapor procedure. However, only small amounts of SF_6 are needed for the experiments, on the order of one percent in the driven section, which is less than 0.1 kPa, the smallest demarcation on the existing pressure gauge. To put in the precise mole fraction of SF_6, the driven section, after filled with oxygen to 345 kPa, is evacuated down to ten times the partial pressure of oxygen. Then the tube is filled, in much the same way as water vapor, with ten times the amount of SF_6. Then the tube is evacuated down to the desired driven pressure and then the rest of the oxygen procedure is followed.

3.1.3.2 Hydrogen fluoride

Numerous and significant changes had to be made for the handling procedures when using hydrogen fluoride. A detailed procedure is given in Appendix B, but the main modifications are given below. The modified set-up is shown in Fig. 3.5. Because it is a corrosive gas, the bottle was always stored in a fume hood. Also, safeguards were made to vent off the combustion products which contained hydrogen fluoride. A scrubber was built to neutralize the products before being discharged to the atmosphere. A flushing system was also built, which is simply a way to drive the hydrogen fluoride out of the shock tube. High pressure nitrogen was used as the flush because it is relatively cheap and dry. Any moisture within the system would promote corrosion. Finally, the tube had to be HF resistant, which meant replacing all rubber gaskets with Teflon, replacing the quartz window when excessive corrosion was evidenced, and repairing the external trigger to prevent leaks.

The procedure was modified to ensure safety. First, prior to filling the tube with oxygen, the tube is first filled with nitrogen to approximately 650 kPa. This step allows for the detection of leaks and purges any moisture from the system while the nitrogen is being vented off. The oxygen

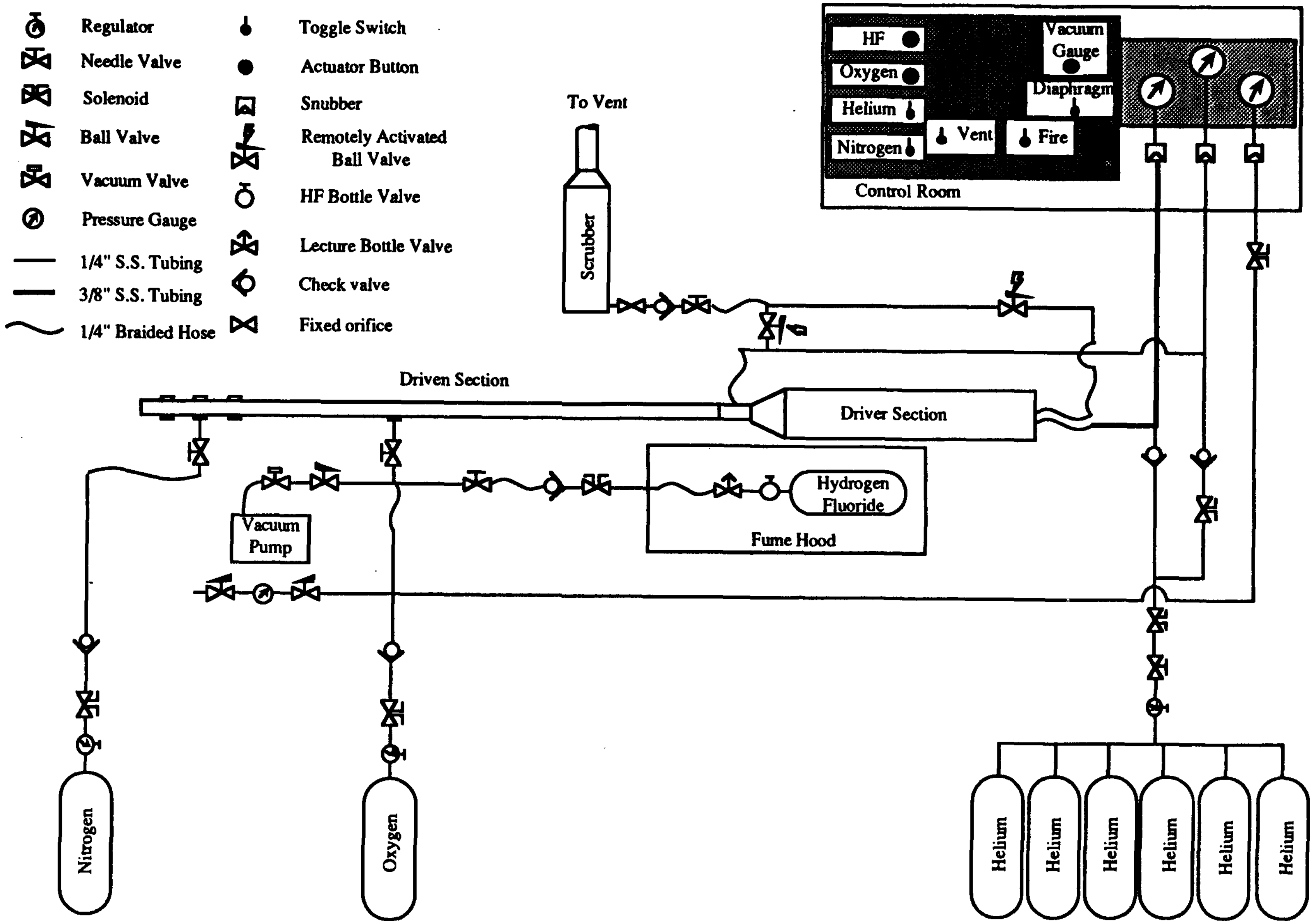

Figure 3.5 Piping layout for installing hydrogen fluoride into the shock tube.

installment is the same as the water vapor procedure. After the partial pressure of oxygen is in the tube, hydrogen fluoride is regulated into the tube by way of a push-button solenoid and interlocking valves. Hydrogen fluoride is stored as a liquid that begins to evaporate when lowered to a pressure of one atmosphere. When the solenoid is open, the bottle is exposed to complete vacuum, so there must be a quick action solenoid or else considerable amounts of HF will enter. That is the reason for using the interlocking valves, which allow minimal amounts of HF in the piping. After the hydrogen fluoride is in the tube, a few minutes must pass before filling the driver section because hydrogen fluoride does react with the shock tube and "plates" out, making it appear that no hydrogen fluoride is in the tube [36]. If no pressure drop is observed in the driven section, the procedure can continue as in the oxygen procedure.

3.2 Experimental Data

The data desired are the conditions of the gas behind the reflected shock as well as the time it takes the boron to ignite and burn. The temperature and pressure are determined from the initial set up conditions and the velocity of the incident shock wave. The velocity is measured with PCB piezoelectric pressure transducers located along the sidewall and endwall of the shock tube (see Figure 3.6). The transducers send the voltage signal to a Soltec ADA-1000 8 bit, 10 MHz digital waveform recorder, which in turn downloads the data to an IBM-AT computer through an IEEE-488 parallel port. The signals from the endwall and sidewall transducers are depicted in Figure 3.7 (a), (b), and (c). A more detailed description of the setup can be seen in Ref. [5]. The distances between transducers are known and the time the shock wave reaches each transducer can be read from the recorder/computer. This will yield the velocity of the shock wave. The average of the velocity between the sidewall transducers and the velocity between the second sidewall transducer and the endwall is used as the shock wave's actual velocity. Its Mach number is determined from the initial driven conditions. With the Mach number and initial pressure and temperature of the driven section, the NASA Gordon-McBride code can calculate the final pressure and temperature.

The ignition and burning of the particles are recorded with Motorola MRD500 semiconductor photo detector, which is sensitive to light in a wavelength region ranging from 0.35 to 1.25 μm with a peak sensitivity at 0.8 μm. The photodiode also sends its signal to the Soltec recorder. The radiation from the particles passing through the endwall window is collected with an 80 mm diameter aspheric collecting lens. The light then reflects off a mirror and is focused onto the photodiode (see Figure 3.8). The data analyzed is the voltage outputted from the photodiode. A typical signal is shown in Figure 3.7 (d). The two peaks represent the two sizes of particles igniting, which are discussed in section 3.3.

Because the ignition event is not well characterized (see discussion in Chapter 4), ignition delay is measured with two methods. The first method measures ignition time in the following

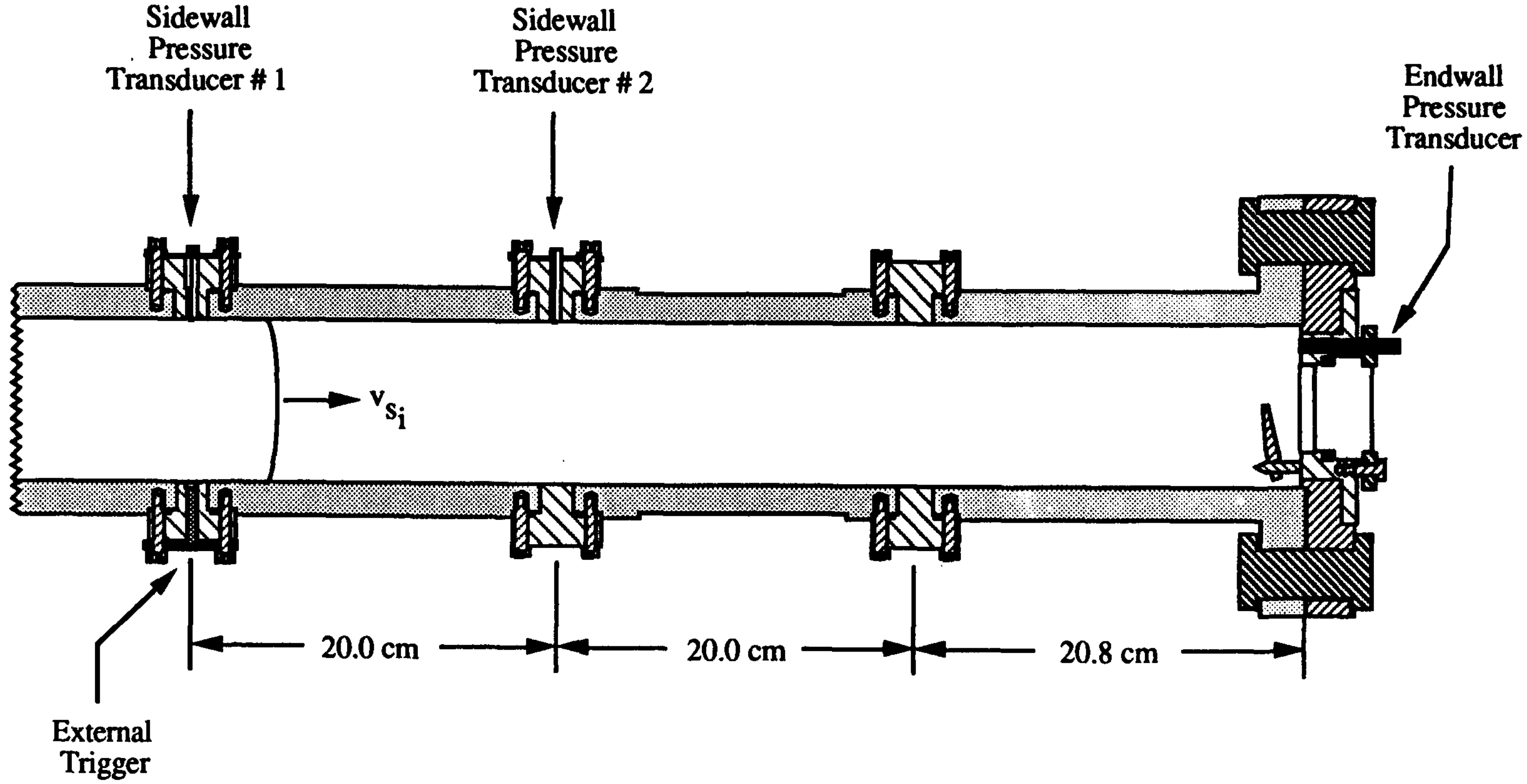

Figure 3.6 Arrangement of the shock tube pressure transducers and recorder trigger.

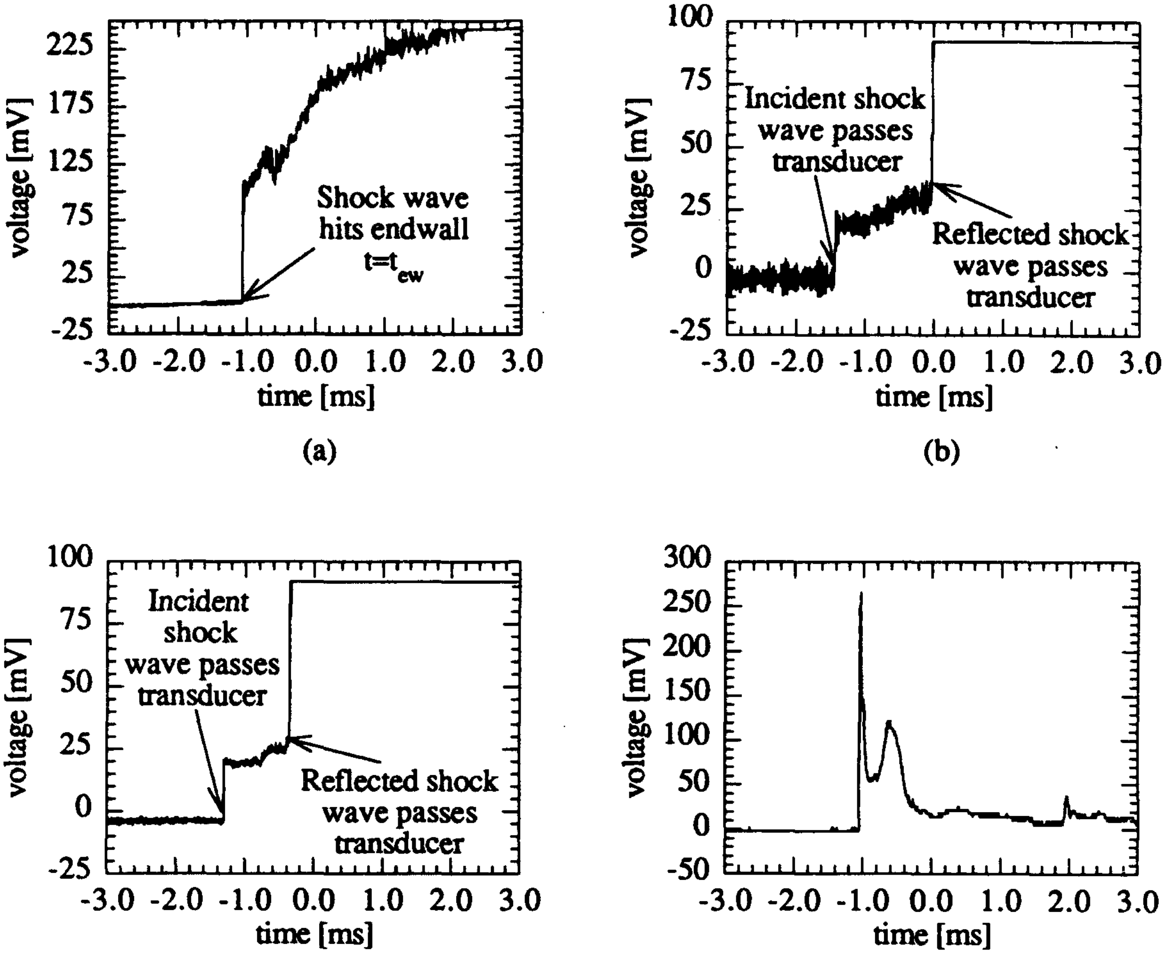

Figure 3.7 Sample signals from (a) endwall pressure transducer, (b) first sidewall pressure transducer, (c) second sidewall pressure transducer, and (d) photodiode. All ignition times are referenced from t_{ew} in (a).

way. The initial voltage (8), the peak voltage (10), and the midpoint (9), shown in Fig. 3.9, of the first peak are averaged. The time where the signal is the average voltage is defined as the time of ignition for the main particles. The ignition delay time is measured relative to the time the shock wave reaches the endwall, measured with the endwall transducer.

To determine the burn time of the main particles, the downward slope's times at peak (10), midpoint (11), and minimum voltage (12) are averaged. Then the average rise time is subtracted from the fall time, which yields the burn time. The ignition time of the small particles is defined the same way as the main particles except peaks 1 and 2 are combined to determine the burn time. The ignition delay time is also relative to the endwall signal. The burn time of the large particles is also similar to the first peak.

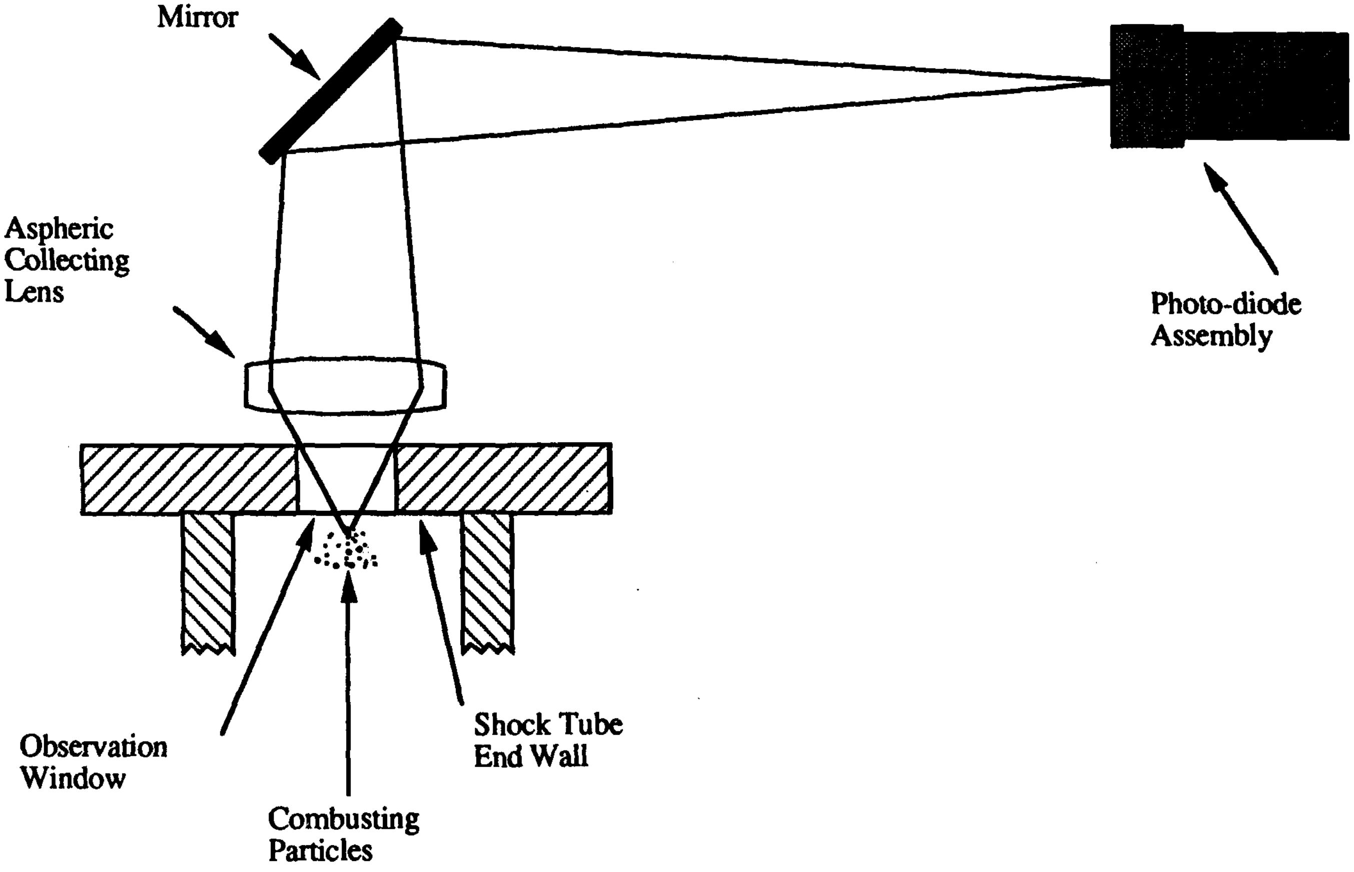

Figure 3.8 Optics layout to record radiation from combusting particles.

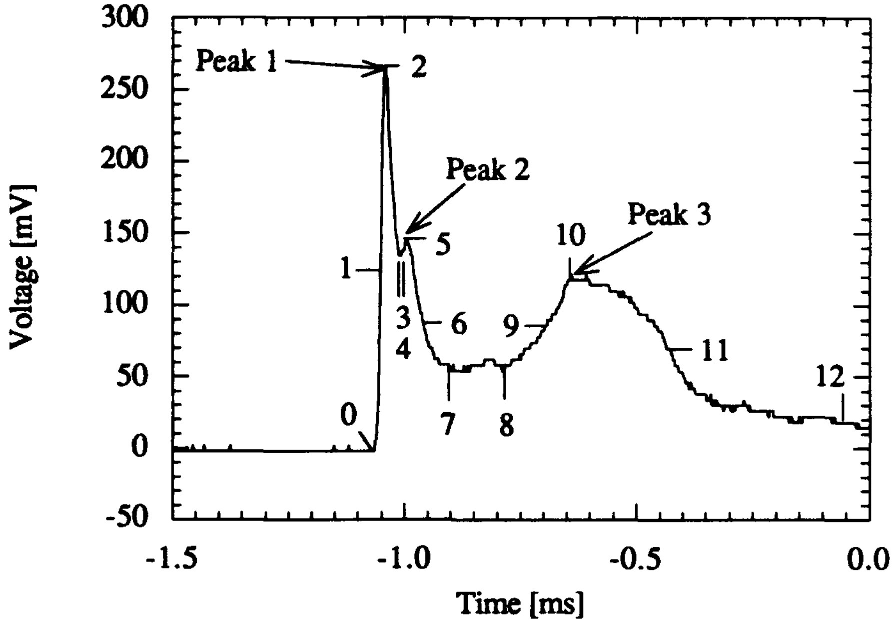

Figure 3.9 Sample signal from the photodiode. The two peaks represent two different size particles burning.

The *second method* is similar to method Roberts used for aluminum/magnesium particle studies [4]. The half height of the first and third peaks are the points where the times are recorded. The upward slope's half height time minus the time the shock wave reached the endwall is defined as ignition delay time. The downward slope's half height time minus the upward slope's time is the burn time.

The reason for a need to define two types of measurements is because the second peak usually had two different shapes. Frequently, the peak had a steep upward slope, but in some cases, the slope was gradual. Simply measuring the half height of the latter signal is difficult because the signal could remain at the half height voltage for up to 50 μs. However, the valley between the two peaks also has a considerable variance which would bias the measurements of the first method. Both methods are discussed in Chapter 4.

3.3 Boron Particles

Two types of boron particles are used in the experiments. The primary supply is a *crystalline* boron purchased from Aldrich Chemical Company, Inc. The supply obtained has a size range of 45 μm or less and has a quoted purity of 99%. For the tests to yield comparable results, the powder is sifted into specific size ranges. This is accomplished with the Gilson vibrating shaker accompanied with U.S. Standard sieves with mesh sizes of 325, 400, 450, 500, and 635 which correspond to mesh openings of 45, 38, 32, 25, and 20 μm respectively. The stated tolerance of all mesh openings is ±3 μm.

The particles are viewed under an optical microscope to determine if the sieving technique is working. The sieving technique is poor in many cases since there are still ultra-fine particles falling through after the sieves are tapped by hand. This is said to be due to static charge holding the particles together because the particles are so small. The sifting is then continued by hand to contribute more force to the process. After a lengthy time for hand sieving, the optical microscope shows particles of basically two different sizes. The larger of the particles appear to be similar in size and they are assumed to be the size the sieves would catch. The smaller particles are of the range of one micron or smaller.

Photographs of the particles are taken with a Scanning Electron Microscope (SEM) which confirm the presence of two sizes. Both sizes are considered to be present in the tests. As for the actual diameter, the particles are crystalline in shape so the diameter of the larger particles are measured by the sedimentation technique with a Horiba CAPA-700 Particle Analyzer with glycerin as the dispersion fluid. Figures 3.10 through 3.15 show photomicrographs of the particles within the 20-25 μm, 25-32 μm, and 32-38 μm size range along with their measured effective diameter histograms. Although there is a considerable standard deviation, qualitatively comparing the two samples indicate there is a significant difference in size and therefore, the sieving was judged successful. Because the standard deviation is large and because measurements of many samples from the same size range resulted in a range of mean effective diameters, the particles are considered to be the size of the sieve that caught them (20 μm from the 20-25 micron sample).

Figure 3.16 shows an SEM photomicrograph of a single 20 μm particle. As can be seen, the particles have smaller, "parasitic" particles attached to them. These particles could not be measured by sedimentation except by finding how many particles did not fall within the range of measurement. To find a general distribution of the small particle, a blow-up of the photograph is used to measure the longest diameter of the particles by hand. The small particles on one face of a large particle are counted and measured. The distribution is presented in Fig. 3.17.

The second supply is an *amorphous* boron purchased from Johnson Matthey Catalog Company. Amorphous "particles" are actually agglomerates of smaller particles, but for this research, the agglomerates are referred to as particles. The particles are quoted to have an average diameter of 10 microns, however, the label states that the boron was less than 1 micron, an extremely small size that prevents any meaningful ignition delay experiments. A Scanning Electron photomicrograph is presented in Fig. 3.18. The particles ranged in size, but there were no particles greater than 7 microns. Since a majority of the tests would deal with the crystalline

Figure 3.10 Scanning Electron Microscope photomicrograph of crystalline boron sieved between 20-25 microns. The long bar at the bottom of the photograph is 100 μm.

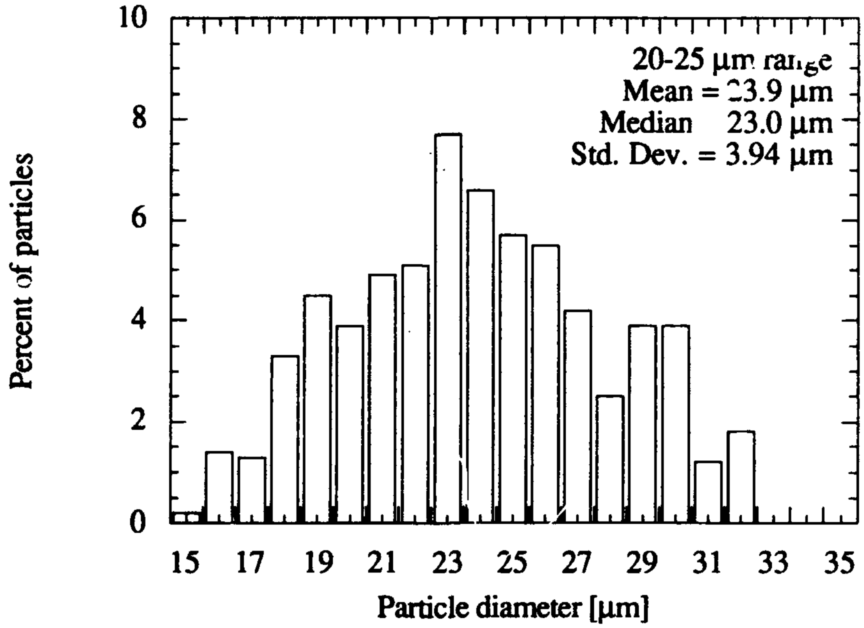

Figure 3.11 Histogram of 20-25 micron crystalline boron particles.

Figure 3.12 Scanning Electron Microscope photomicrograph of crystalline boron sieved between 25-32 microns. The long bar at the bottom of the photograph is 100 μm.

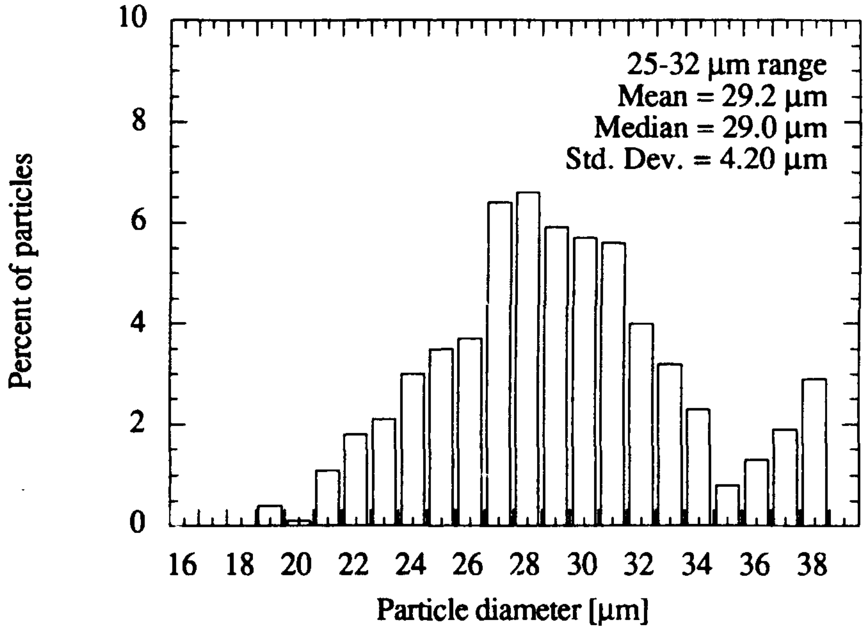

Figure 3.13 Histogram of 25-32 micron crystalline boron particles.

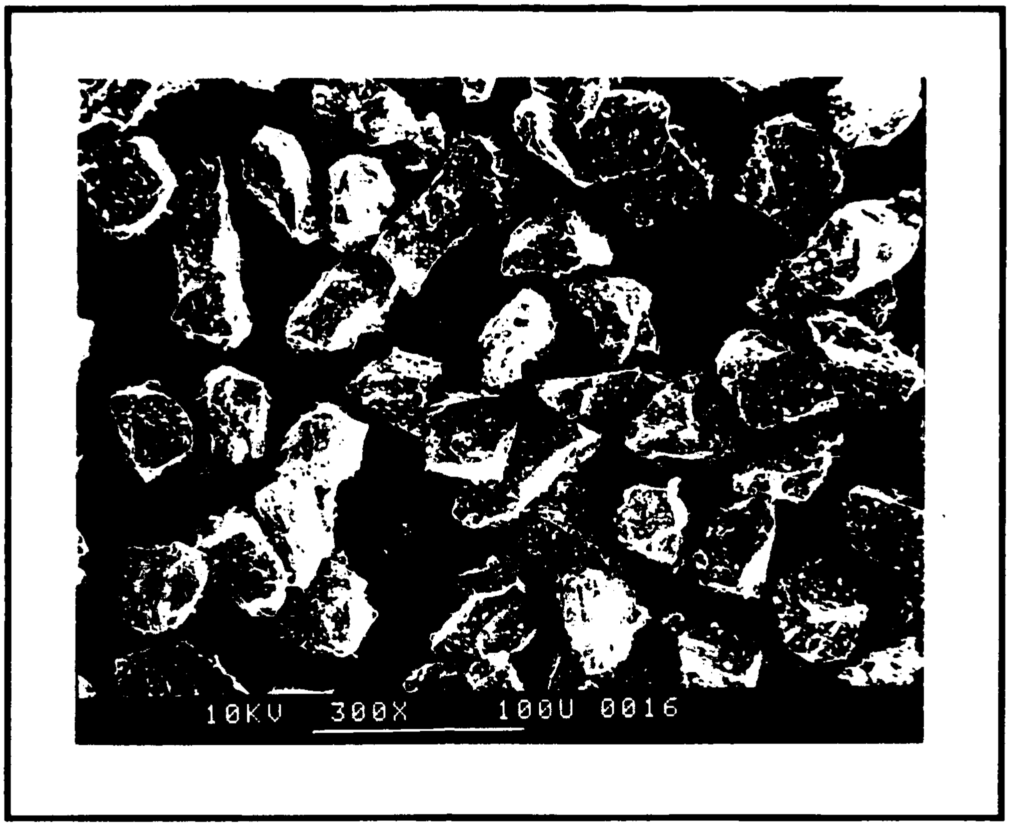

Figure 3.14 Scanning Electron Microscope photomicrograph of crystalline boron sieved between 32-38 microns. The long bar at the bottom of the photograph is 100 μm.

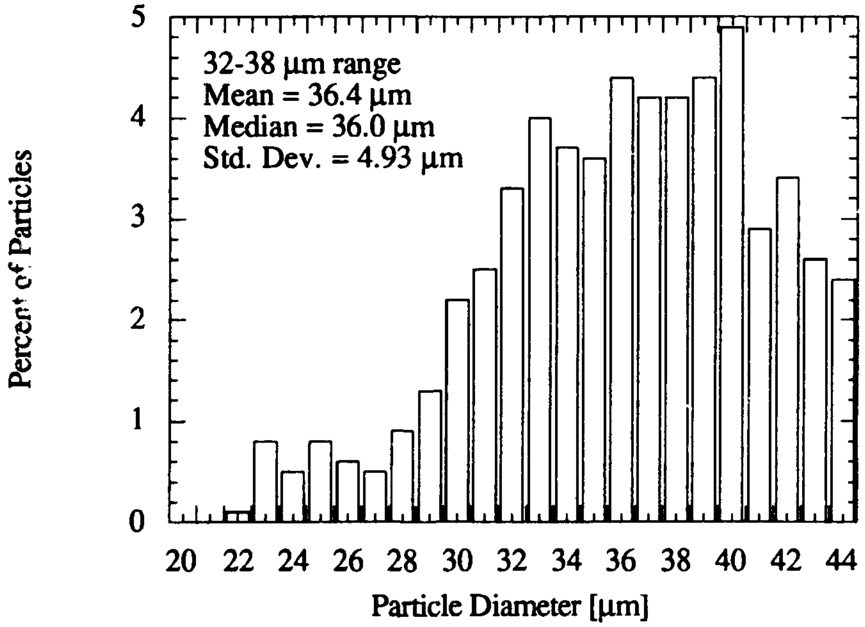

Figure 3.15 Histogram of 32-38 micron crystalline boron particles.

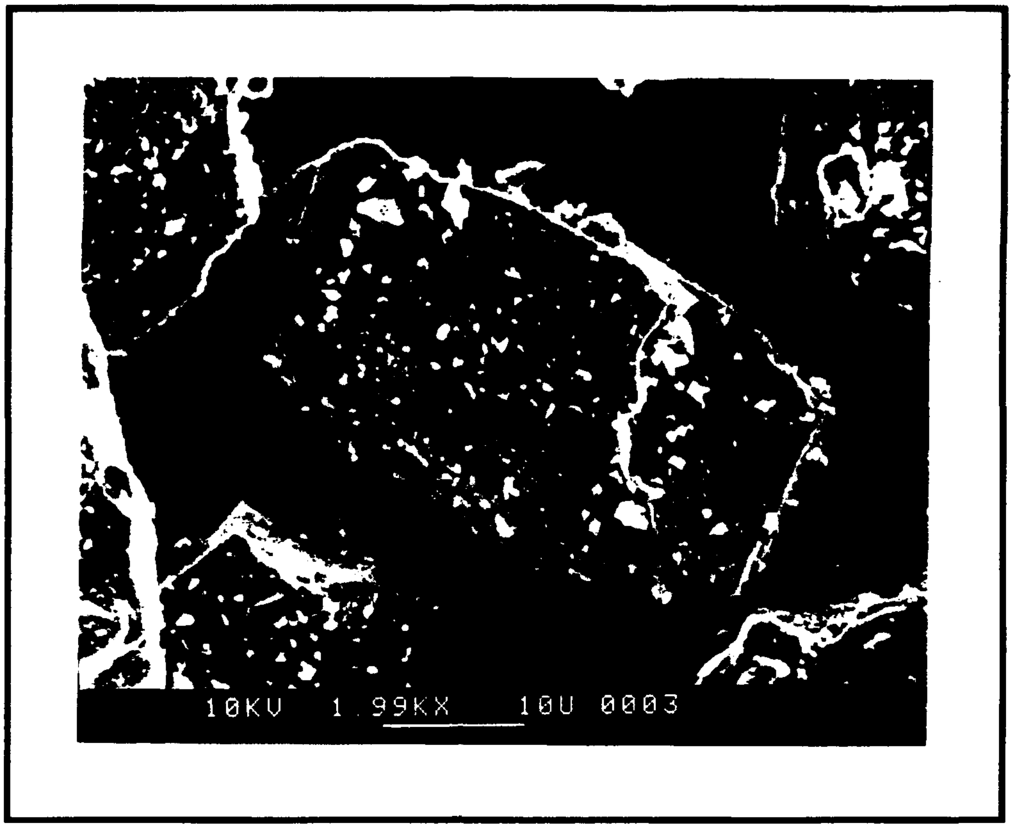

Figure 3.16 Scanning Electron Microscope photomicrograph of a single crystalline boron particle sieved between 20-25 microns. The long bar at the bottom of the photograph is 10 μm.

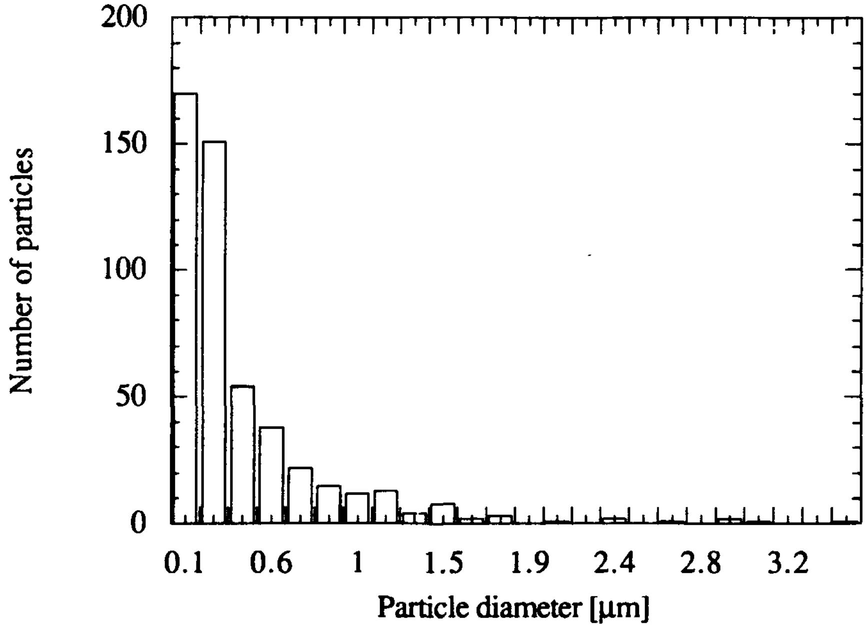

Figure 3.17 Size distribution of "parasitic" particles attached to larger particles shown in Fig. 3.16. The diameter represents the longest width of the particle. Taken from a sample of 500 particles.

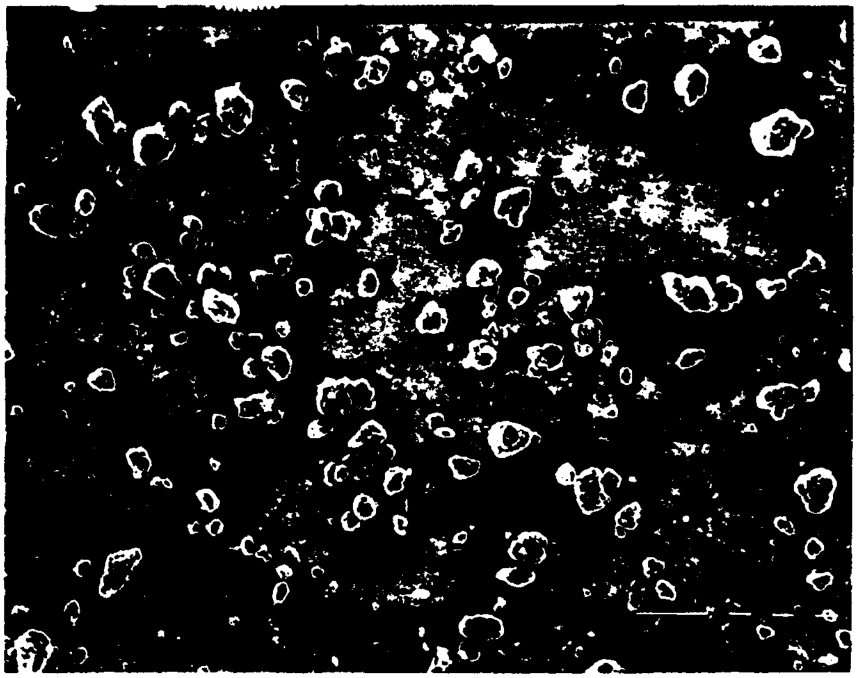

Figure 3.18 Scanning Electron Microscope photomicrograph of amorphous boron. The long bar in lower right corner is 10 μm.

boron, there was no attempt to correct the discrepancy, and amorphous boron particles were not further studied.

3.4 Operating Conditions

The limit of operating conditions is determined from the design of the shock tube and the type of oxidizer that is used. The structural design of the shock tube is made to hold a maximum of 10 MPa in the driver section. If oxygen is used, this would correspond to a test pressure of 34 atmospheres and a temperature around 3000 K [5]. Higher temperatures could be obtained if the desired test pressure is low. If other gases are used, the limitations change in order to account for the different molecular weights and different rates of dissociation.

The initial ignition delay experiments with boron utilized 100 percent oxygen. The results from these tests were then used as the basis for comparison with experiments when other gases are added to the oxygen. Also, these pure oxygen tests indicated which size particles were best suited for the experiments. Although calculations were conducted similar to Roberts' aluminum particle ignition delay calculations [4] to show that 45 micron boron particles would ignite within one millisecond in gas temperatures of 3000 K, and that "d^2 law" calculations applied to Macek's data

[14] show that 32 micron particles would ignite within one millisecond, then the size range available (20-25 micron) was appropriate for a majority of the experiments. The initial experiments did show that those particles ignited in less than one millisecond in a range of gas temperatures (2500-3100 K).

Water vapor was the first additive to the oxidizer that is employed. Previous experiments with boron and water vapor [14] used mole fractions between 0.20 and 0.30 but the remaining gases consisted of a mixture of oxygen and carbon dioxide. This research used 30% water vapor and 70% oxygen.

Sulfur hexafluoride was then later added to the oxygen in following experiments. The amount of sulfur hexafluoride is calculated from the amount of boron used per experiment. There were approximately ten thousand particles used for each experiment. If three fluorine atoms react with each boron atom (described in Section 2.4), then a mole fraction of 0.02 of sulfur hexafluoride would create enough fluorine atoms to react with all of the boron. If more SF_6 is used, sulfur dioxide would be a considerable final product. Sulfur dioxide is a yellow powder that coats the inside of the shock tube after firing and is difficult to remove so a maximum of two percent SF_6 was set. A majority of the experiments were conducted with one percent SF_6 added to 99% oxygen.

Finally, hydrogen fluoride was the last additive tested. To keep the experiments similar, the number of hydrogen fluoride molecules used was the same as the number of fluorine atoms produced in the sulfur hexafluoride experiments. Calculations show that here is not much dissociation of HF at the temperatures studied, i.e. less than one percent, and therefore a maximum of twelve percent of hydrogen fluoride is used. 6% HF and 94% oxygen experiments are the main focus of this research.

To calculate the initial conditions for each experiment, a computer code employing gas dynamic relations specific to the shock tube geometry [18] was utilized. The code iteratively uses the NASA Equilibrium Gas Composition program [34] to determine the operating parameters P_1 and the incident shock wave Mach number as a function of P_5 and T_5. The driver pressure was then estimated from the ideal gas relation. However, at certain lower test temperatures for some oxidizer compositions, the ideal driver pressure differs significantly from the actual driver pressure necessary. The driver pressure is then measured experimentally and a best fit relation between the initial pressure ratio and incident Mach number is found and then used for future calculations of driver pressure.

The oxygen and water vapor/oxygen performance parameters are shown in Figs. 3.19 through 3.22. As can be seen in Fig. 3.19, the gas composition is a major role player in the determination of initial conditions. Because of the increased energy loss due to dissociation of the water molecule compared to the oxygen molecule, the final gas temperature is decreased. Although initial pressure is not a function of oxidizer, shown in Fig. 3.19, the initial pressure ratio (Fig.

3.21), and therefore the initial driver pressure (Fig. 3.22) are affected by the presence of water vapor.

A more dramatic effect of dissociation is shown with the sulfur hexafluoride performance parameters depicted in Figs. 3.23 through 3.26. Since SF_6 is easily dissociable, considerable energy is used for this dissociation rather than increasing the temperature of the gas. This trend can be seen for increased SF_6 is in the driven section (Fig. 3.23). The irregularities of the Mach number/reflected temperature relation is due to the amounts and rates of dissociation for each fluorine atom of the sulfur hexafluoride molecule. As in the oxygen/water vapor relation, initial driven pressure is not a function of oxidizer but the driver pressure is related to the driven gas composition.

Finally, hydrogen fluoride performance parameters are shown in Figs. 3.27 through 3.30. There is little difference between HF parameters and oxygen parameters due to HF's resistance to dissociate. With these figures, as well as with the figures for the other gas compositions, the following simple four step procedure can be followed to specify the initial conditions:

(1) The desired reflected shock temperature and pressure were chosen.
(2) The magnitude of the reflected shock Mach number were read from the Mach Number versus Reflected Temperature figure of the desired gas composition.
(3) The initial driven pressure were read from the Driven Pressure versus Mach Number figure of the desired gas composition.
(4) The initial driver pressure was read from the Driver Pressure versus Mach Number figure of the desired composition.

For the experiments conducted, the Mach number of the incident shock wave ranged from 2.9 to 6.0. The pressures ranged from 7.0 to 33.7 atm (102.9 to 495.3 psia) although a majority of experiments were at 8.5 atm. The temperatures ranged from 1173 to 3088 K, where the greatest concentration of measurements were above 2500 K. Ignition times for the large particles ranged from 130 to 1300 μs while the small particles had ignition times ranging from 10 to 40 μs. The results for all of the experiments are in the following chapter.

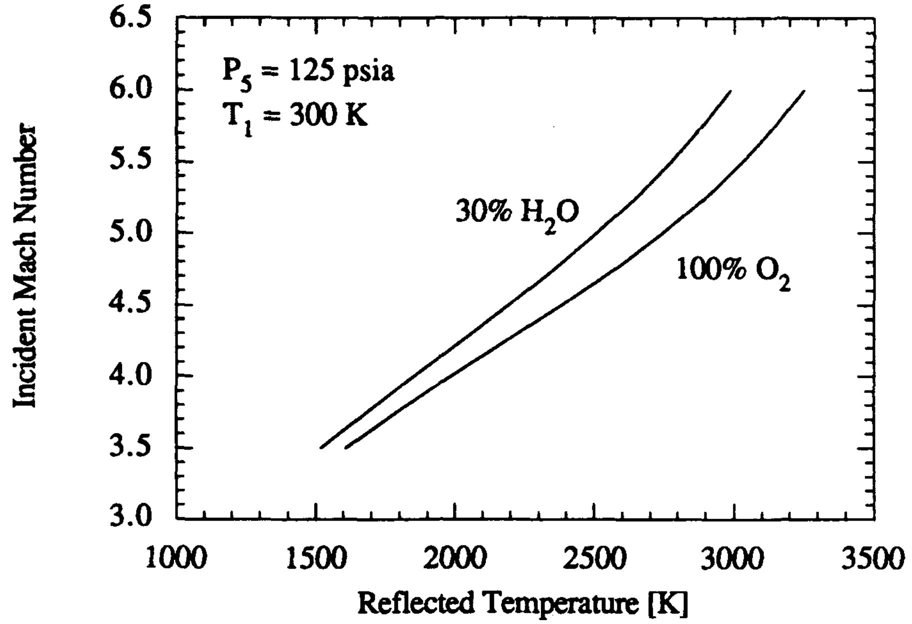

Figure 3.19 Calculated incident shock Mach number as a function of reflected gas temperature and oxidizer composition. Calculated with the NASA Gordon-McBride code [34].

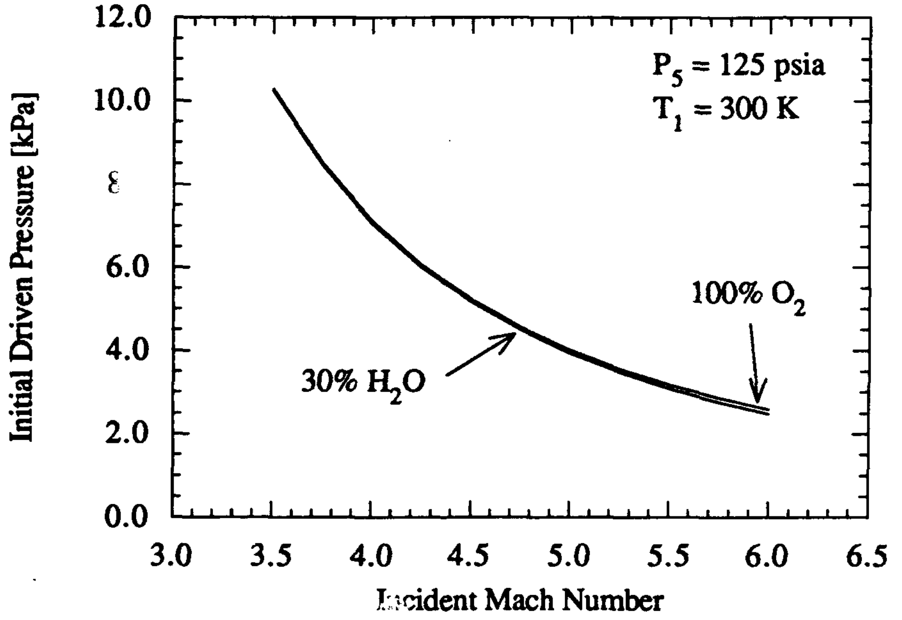

Figure 3.20 Required initial driven section pressure as a function of the incident shock Mach number and oxidizer composition. Calculated with the NASA Gordon-McBride code [34].

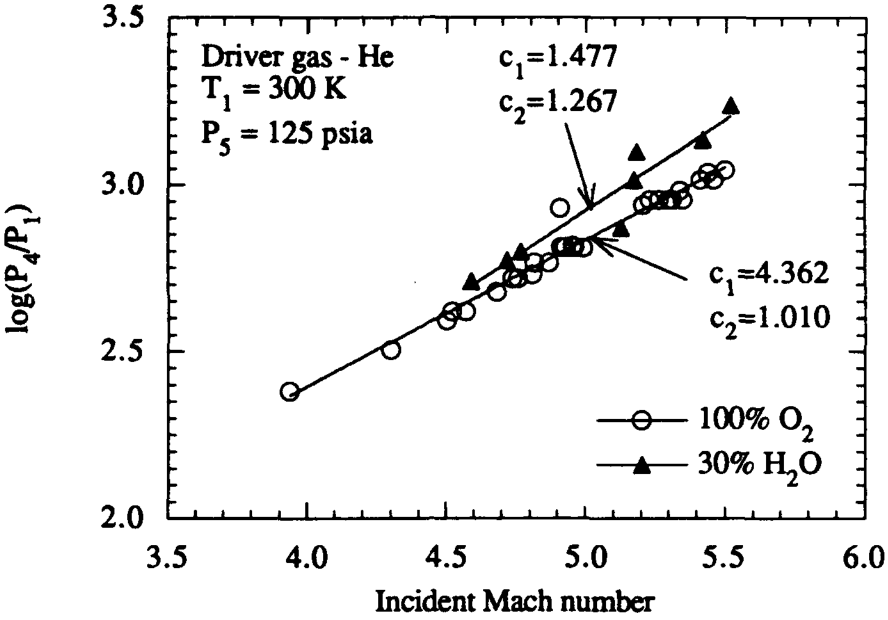

Figure 3.21 Measured shock tube performance as a function of oxidizer composition. Variables c_1 and c_2 refer to the curve fits $P_4/P_1 = c_1 \exp(c_2 M_{Si})$.

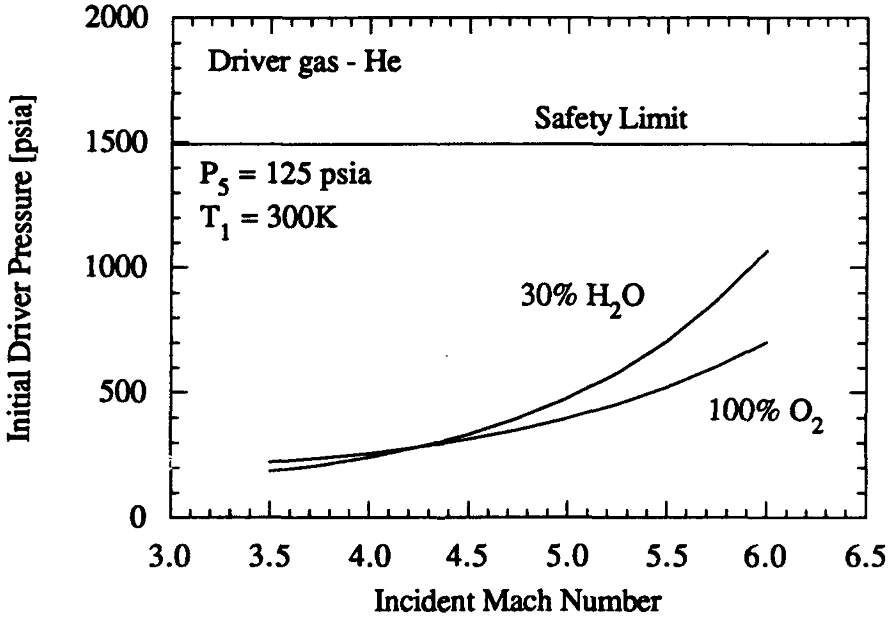

Figure 3.22 Required driver pressure as a function of incident shock Mach number and oxidizer composition. The curves are calculated from the real gas calculations of Fig. 3.20 and the experimental measurements of Fig. 3.21.

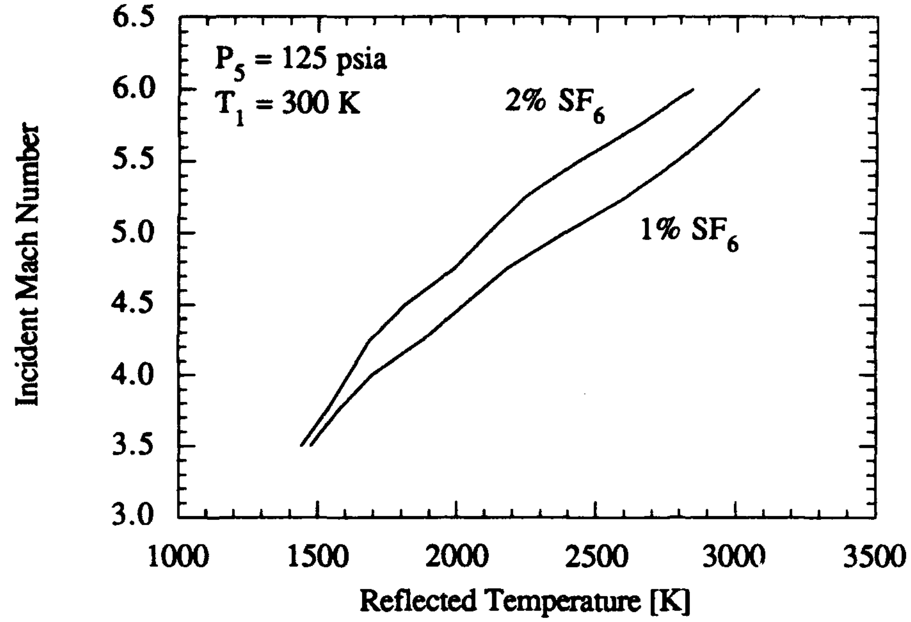

Figure 3.23 Calculated incident shock Mach number as a function of reflected gas temperature and oxidizer composition. Calculated with the NASA Gordon-McBride code [34].

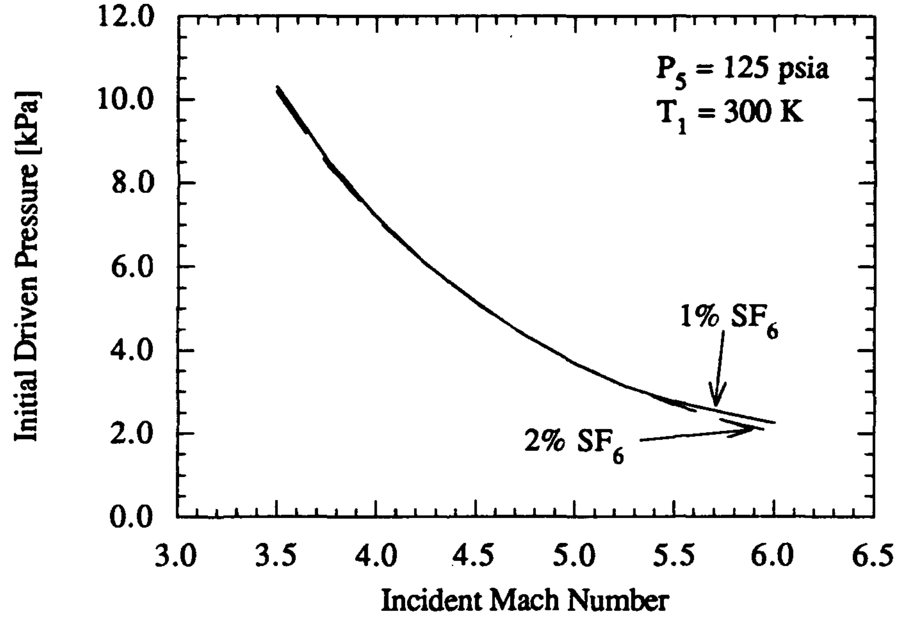

Figure 3.24 Required initial driven section pressure as a function of the incident shock Mach number and oxidizer composition. Calculated with the NASA Gordon-McBride code [34].

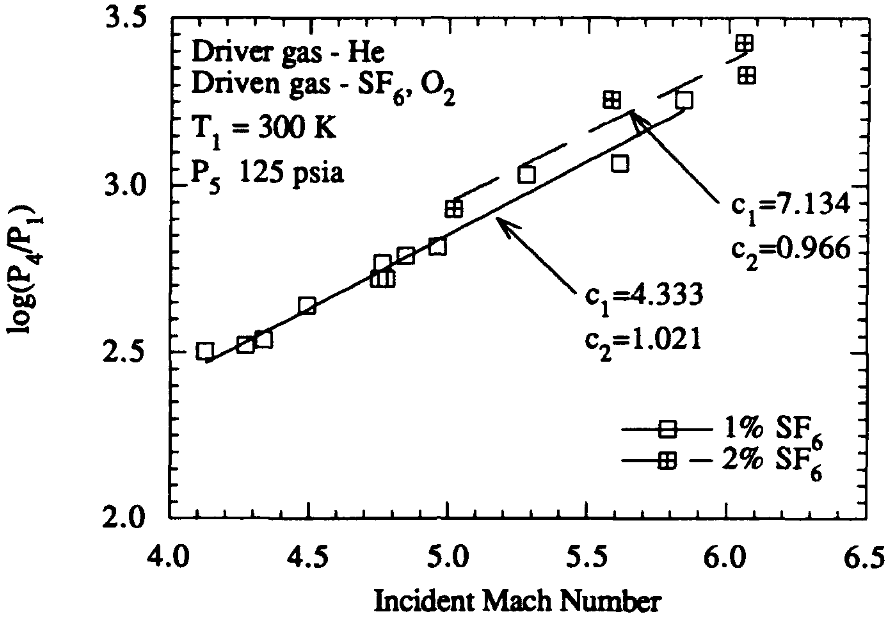

Figure 3.25 Measured shock tube performance as a function of oxidizer composition. Variables c_1 and c_2 refer to the curve fits $P_4/P_1 = c_1 \exp(c_2 M_{S_i})$.

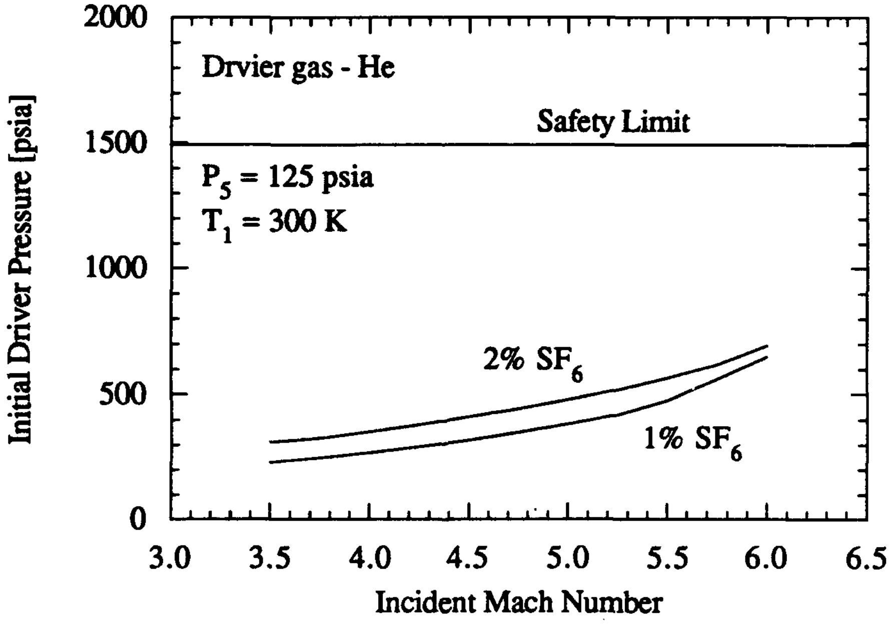

Figure 3.26 Required driver pressure as a function of incident shock Mach number and oxidizer composition. The curves are calculated from the real gas calculations of Fig. 3.24 and the experimental measurements of Fig. 3.24.

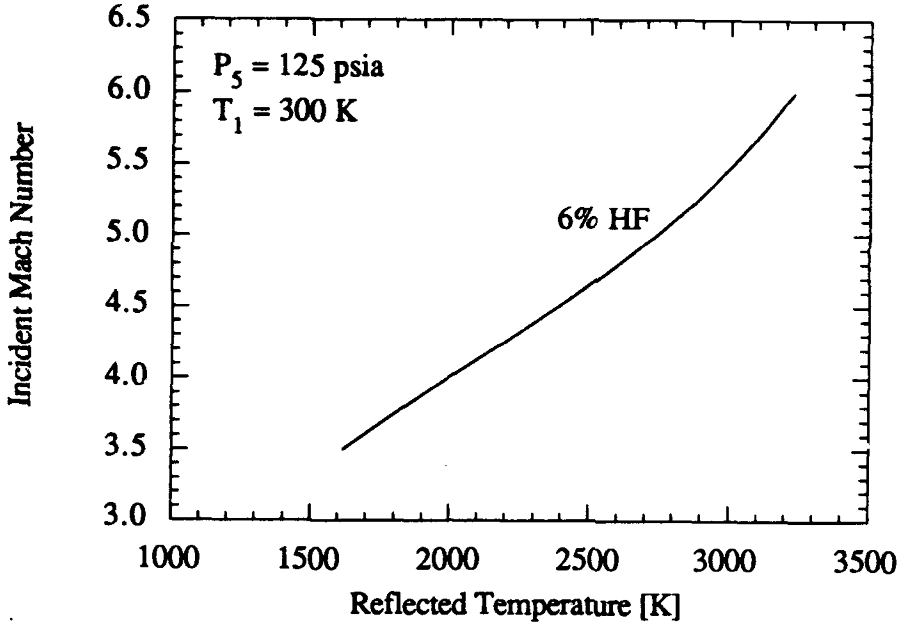

Figure 3.27 Calculated incident shock Mach number as a function of reflected gas temperature and oxidizer composition. Calculated with the NASA Gordon-McBride code [34].

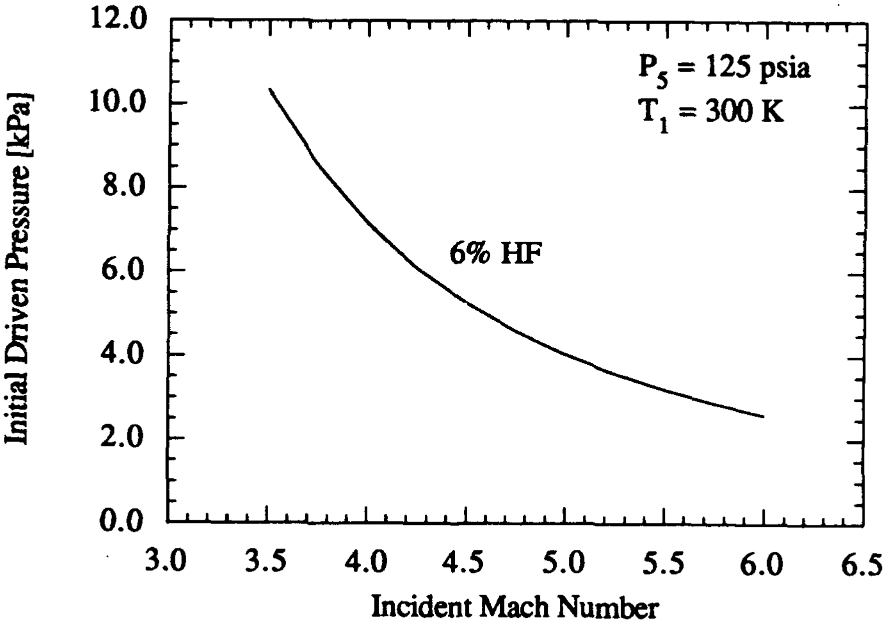

Figure 3.28 Required initial driven section pressure as a function of the incident shock Mach number and oxidizer composition. Calculated with the NASA Gordon-McBride code [34].

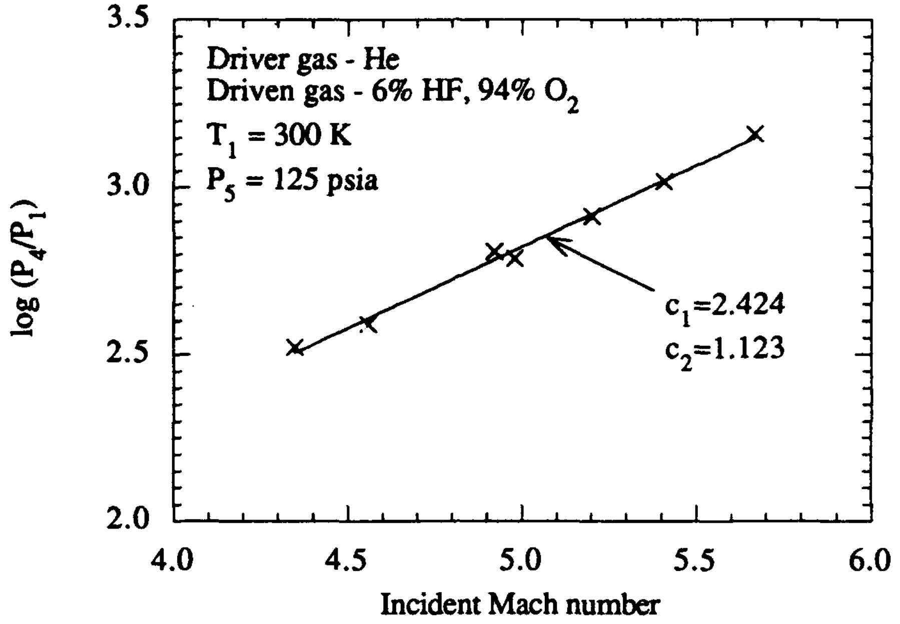

Figure 3.29 Measured shock tube performance as a function of oxidizer composition. Variables c_1 and c_2 refer to the curve fits $P_4/P_1 = c_1 \exp(c_2 M_{S_i})$.

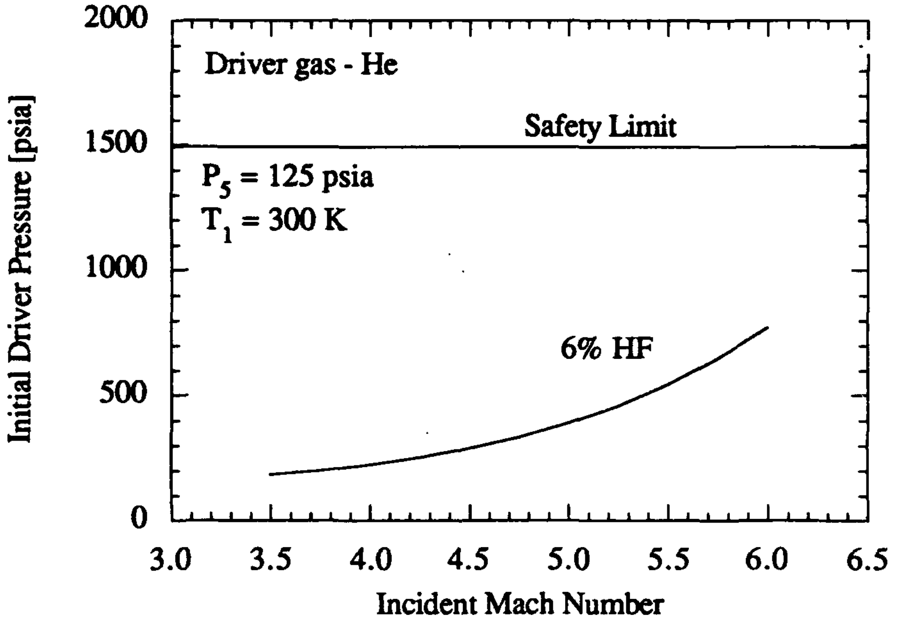

Figure 3.30 Required driver pressure as a function of incident shock Mach number and oxidizer composition. The curves are calculated from the real gas calculations of Fig. 3.28 and the experimental measurements of Fig. 3.29.

CHAPTER 4 - PRESENTATION OF RESULTS

The results of the shock tube experiments are presented in this chapter with the focus on the ignition delay time. The ignition delay data is presented as a function of temperature, pressure, particle size, and more importantly, oxidizer mixtures. A brief discussion comparing amorphous boron to crystalline boron is also given here. Burn time is also presented as a function of the parameters listed above. First, a discussion of data interpretation is in order.

4.1 Interpretation of Data

After the shock tube is fired, the only signals read are from the three pressure transducers and the photodiode. The three pressure transducers measure the velocity of the shock wave from the time-of-arrival data. With that piece of information, along with the initial conditions, the driven gas test conditions can be calculated, using the NASA Gordon-McBride code. The photodiode is used to view the boron combustion process, by measuring the intensity of light emitted from the endwall window, and generating a voltage reading to be recorded by the data acquisition system (DAS). The DAS can be manipulated to record for any length of time, although the actual length of time of the test conditions is limited by the length of the shock tube. The test time, measured by Roberts, et al. [4, 5], ranges from 400 to 1200 µs depending on the incident shock wave Mach number. This is confirmed by Orth, et al. (see Appendix A), and also by examining the endwall pressure transducer signal, which shows the pressure in the shock tube not to increase significantly (10% of its initial value) over the test time. Because of the short test time, small boron particles are used in the experiment and the acquisition system is set for a recording time of not more than 10 ms, with 3 ms being the standard.

Initial experiments are done with amorphous boron. A sample signal is shown in Fig. 4.1. As discussed in Chapter 3, the time measurement of the photodiode signal is referenced to the time the shock wave strikes the endwall pressure transducer. All experiments with amorphous display a similar signal, a single voltage peak (see Fig. 4.1). Since there is only one peak with approximately zero initial and final voltage, the half-height method of measurement discussed in Chapter 3 is used to measure ignition and burn times.

When 20 µm crystalline boron is used, the signal time history is more complex. A typical signal is shown in Fig. 4.2. For the initial oxygen experiments, most signals show three peaks. The first peak appears in all tests above 1800 K. It is suggested that this peak represents sub-micron boron particles combusting. When examining the photomicrograph in Fig. 3.15, the large particle is seen to be covered with smaller parasitic particles. These parasitic particles are on the same size scale as the amorphous boron, on the order of 1 µm. This photodiode peak is also

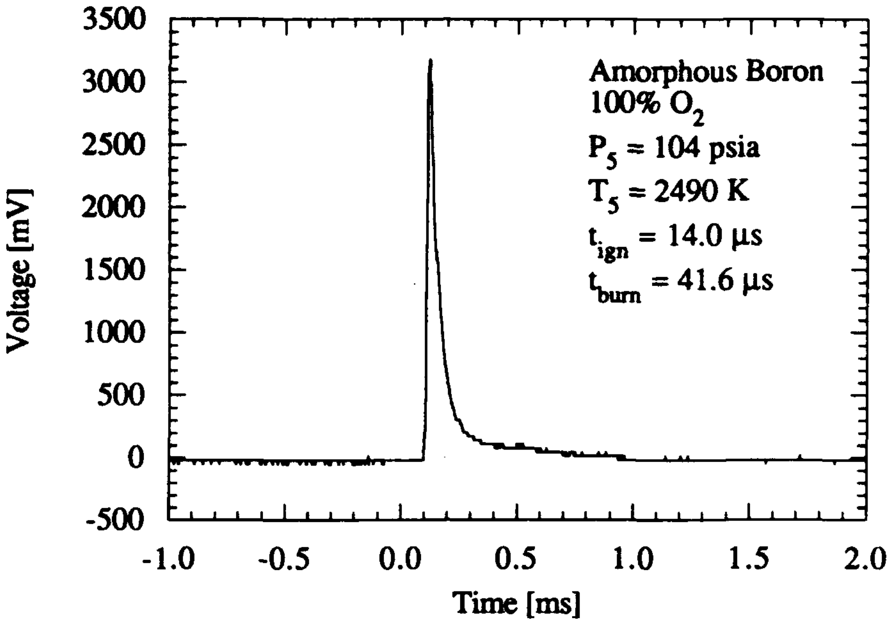

Figure 4.1 Sample amorphous boron light signal in pure oxygen.

similar to the amorphous boron peak in that it occurs within the same time. It would appear that this first peak could well be the combustion of the small particles.

It has been stated by Gurevich, et al. that amorphous agglomerates ignite at lower temperatures than crystal particles of the same size [20] as is evidenced in this research. The first peak from crystalline boron ignition is non-existent in experiments below 1800 K while the amorphous peak disappears around 1450 K. However, as stated in Chapter 2, it is difficult to compare amorphous and crystalline boron particles of the same size directly because of the nature of amorphous boron, being an agglomerate of smaller particles. The evidence still indicates that the first peak represents the small particles igniting, which will be discussed in detail in Chapter 5.

The second peak, which can be seen clearly in Figure 4.3, is not present in all cases. It appears consistently in the pure oxygen experiments, always attached to the first peak as shown. It also is present in a majority of the water vapor/oxygen experiments. However, in almost all of the sulfur hexafluoride/oxygen tests, the second peak is non-existent. It also does not appear in low temperature, below 2500 K, hydrogen fluoride shots. One possible explanation of this peak comes from the phenomenon of two-stage ignition. In previous research, boron particles have been seen to glow for a period of time and then extinguish before another bright glow is evidenced, where the second glow is the particle burning to completion [14]. Here, the second peak can be explained as the second stage reignition and complete combustion of the parasitic particles.

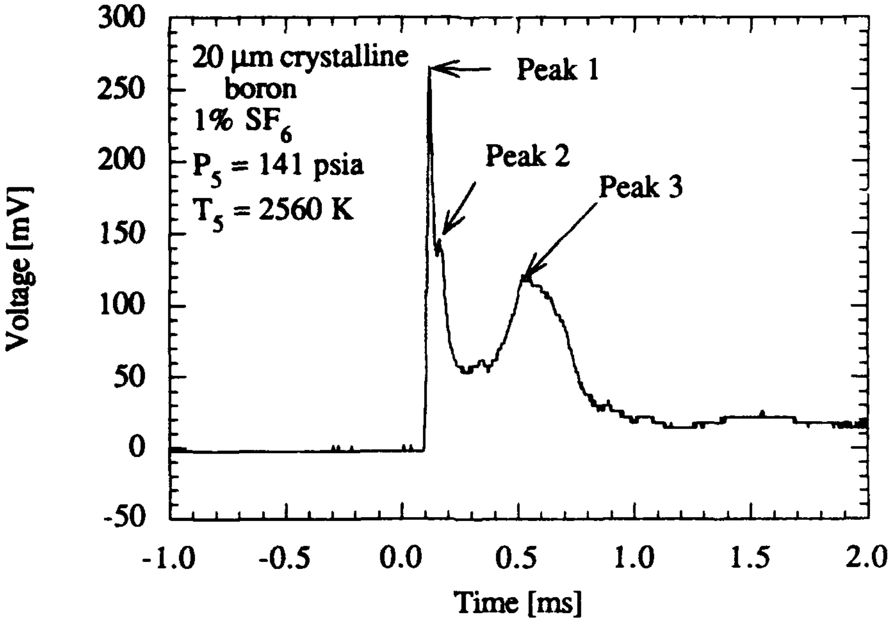

Figure 4.2 Typical crystalline boron light signal.

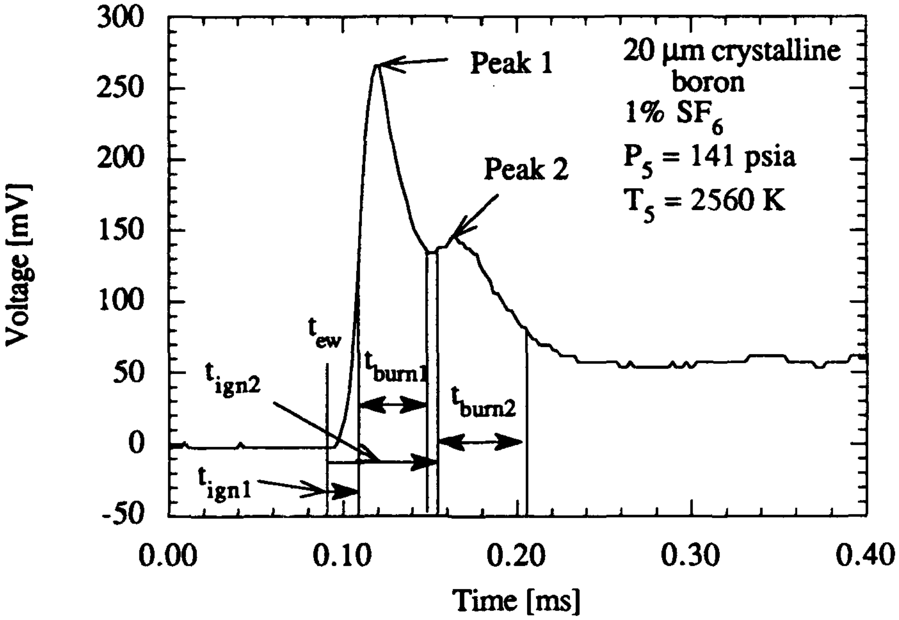

Figure 4.3 Close-up of first two peaks of sample crystalline boron light signal.

Because the first two peaks are not separated from each other, the time measurement technique must be modified. The first peak ignition delay time is measured with the same method as the amorphous boron. However, measuring the first peak burn time is not possible with the half-height method, because the second peak is present before the first peak can fully extinguish, as shown in Fig. 4.3. Therefore, the burn time of the first peak is measured from the half height of the upward slope to the initial lowest point between the two peaks. The reason that the *initial* lowest point is used is that the valley between the two peaks can stay at a minimum voltage for a period of time. From this same valley, the ignition delay of the second peak is measured, although it is measured from the final lowest point in the valley. The burn time of the second peak is then measured with the half-height method on the downward slope. Sometimes, the second peak does not fall to half of its height due to the presence of a third peak. Therefore, the method similar to that of the first peak is used.

The third peak represents the point of maximum light output from the combustion of the main particles. Figure 4.2 shows a typical signal with a well-defined third peak. The measurement of the ignition delay and burn time of the third peak also utilize the half-height method. Again, as with the first two peaks, the half height cannot be measured due to interference of other peaks. Therefore, as before, the minimum voltage plateau between two peaks is employed for time measurements.

An additional method of measurement, called the average method, is also used, for which the lowest, highest, and middle voltages of a slope have their times averaged (see Chapter 3). When compared to the half-height method, the two measurements can differ either way by as much as 100 μs. Also, when studying temperature trends of ignition delay time, both methods show considerable scatter in the data. It is judged that, although both methods have their faults, the half-height method is more consistent in the measurability of time; and therefore, all results presented in this work use the half-height method.

Not all third peaks clearly define an ignition event. While Fig. 4.2 clearly shows ignition, Fig. 4.4 is a case of no ignition. Many tests have peaks that lie between those two examples. Using shots with no particles as a comparison, ignition is said to have occurred if the third peak is at least twice the voltage of the "noise", with a qualitatively clear and significant rise and fall. The cases where ignition is said to have occurred must have a peak voltage of at least 25 mV. However, some points that met the first criteria, do not have a definite shape so are not used for ignition trends except to say that it did not ignite at that certain condition. The case shown in Fig. 4.4 does not display ignition because the third peak is below twice the noise level of 25 mV. Appendix C tabulates all of the data and Appendix D displays all of the photodiode signals.

Another problem that can occur with the photodiode signal is the appearance of other peaks. Figure 4.5 shows a four peak signal. The fourth peak is not consistently present in all

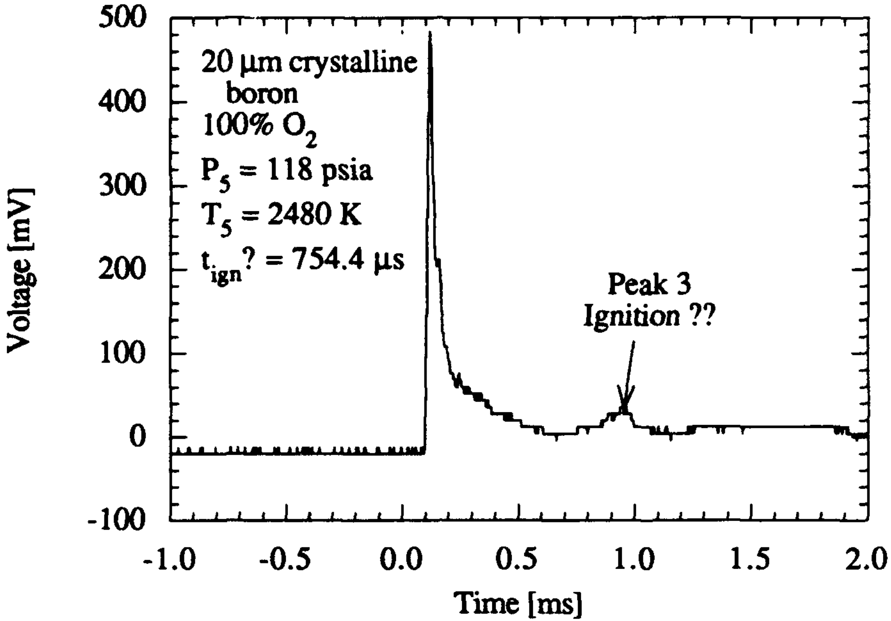

Figure 4.4 Sample crystalline boron signal showing no ignition.

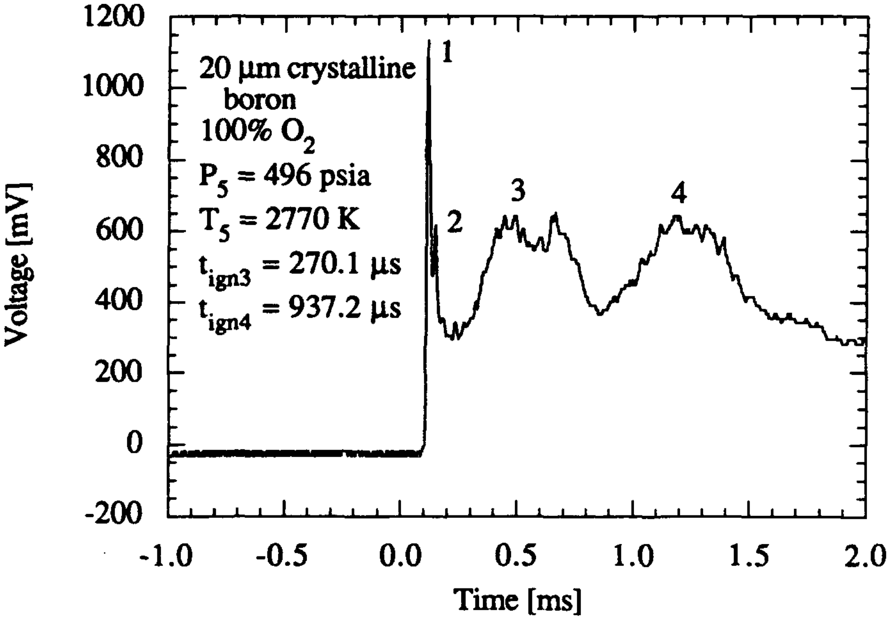

Figure 4.5 Sample crystalline boron signal showing four peaks.

cases, and sometimes there are more than four peaks. If the DAS is set for a long enough recording duration, some of the signals are caused by pieces of diaphragm material that travel down the shock tube and burn in the test section. Since the time it takes the particles to reach the test section is estimated to be approximately 10 ms, these particles do not affect the boron readings. Another possible reason for the extra peaks could be particle fragmentation. A third possibility could be that the large particles behave as the small particles, and have two stage ignition. The fragmentation hypothesis is the more likely candidate, because the fourth peak is not always present, even in repeated experiments, and because there are no evident trends in ignition delay time with temperature. For the most part, fourth peak igniti [illegible] times are recorded but not studied in detail here.

4.2 Amorphous Boron Results

Even though the focus of this research is on crystalline boron, some limited results can be derived from the amorphous boron data. Once again, amorphous boron is considered to be an agglomerate of particles so that particle size analysis cannot be accomplished. A brief investigation of amorphous boron ignition delay time and burn time versus temperature for different pressures and oxidizers is conducted. The temperatures studied ranges from 1400 to 2800 K. The nominal condition, to which all results are compared, is a reflected pressure of 125 psia for a 100 percent oxygen atmosphere. The results are presented below.

4.2.1 Pressure effects

Two pressures are investigated; 125 and 250 psia as shown in Fig. 4.6. The 125 psia data clearly display an ignition limit of 1425 K, below which ignition is not measured with the photodiode or the DAS. The acquisition system, for all cases with amorphous boron, is set to record for 6 milliseconds. The recording time encompasses the 400 μs period of constant ambient conditions produced by the reflected shock wave (see Appendix A), and the sub 50 μs ignition delay times in Fig. 4.6. It is possible that the ignition event occurred beyond that time but unlikely for there would have to be jump from 50 μs to 3 ms within a few degrees in temperature. For the photodiode to miss the event, the particles would have to be out of the field of view of the lens, an unlikely occurrence because the optical system is aligned before every shot. During the test time, the particles gravitationally fall less than 4 μm indicating that if no light signal is measured, ignition did not occur.

An important result from Fig. 4.6 is the trend of ignition delay versus temperature. Between 1425 and 1900 K, there is a definite decrease in ignition delay with increasing temperature. Above 1900 K, the ignition delay is approximately 15 μs, independent of

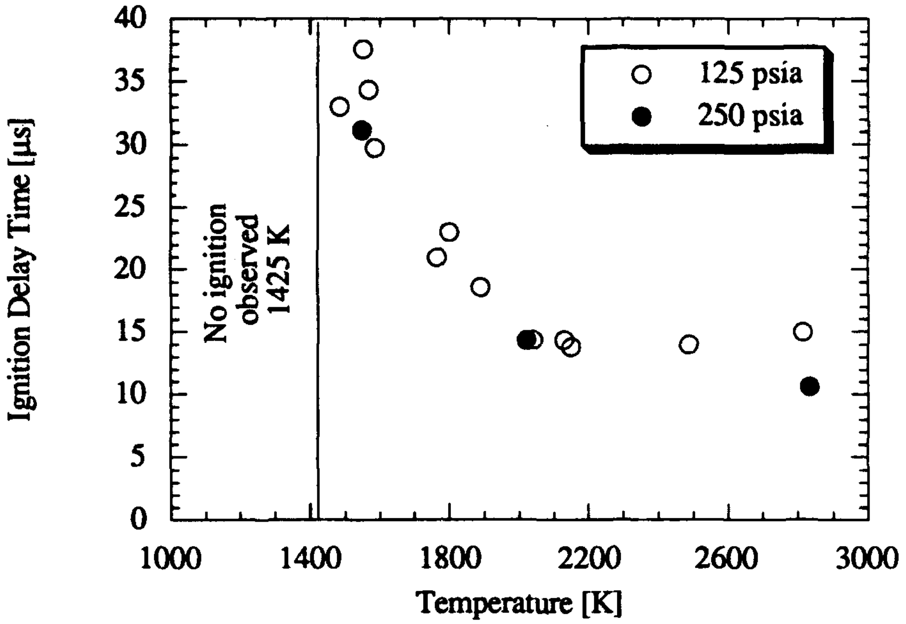

Figure 4.6 Amorphous boron ignition delay time versus temperature at two pressures. All conditions tested with 100% oxygen. The ignition limit of 1425 K is found at 125 psia.

temperature both for the 125 psia and the 250 psia cases. The difference of 4 µs between the two different pressures at 2800 K is within experimental error.

Figure 4.7 shows the burn time of amorphous boron in 100 percent oxygen for 125 and 250 psia. All burn times occur between 16 and 42 µs, on the same order as the ignition delay time. There is no obvious trend of burn time with temperature or pressure. This trend could possibly be obscured by the accuracy of the time measurement, but it is felt that this is unlikely.

4.2.2 Oxidizer effects

Figure 4.8 presents the effects of both 100% oxygen and 3/97 percent sulfur hexafluoride/oxygen oxidizers on the ignition delay of amorphous boron as a function of temperature. All experiments were conducted at a nominal pressure of 125 psia. When compared to the oxygen data, considerable differences are observed with the addition of SF_6.

The three percent sulfur hexafluoride in oxygen conditions decreases ignition delay time at temperatures from 1500 to 1700 K. At 1450 K, the SF_6 data approach the oxygen data, close to the 1425 K ignition temperature limit of boron in oxygen, but SF_6 appears to be an ignition accelerator at slightly higher temperatures.

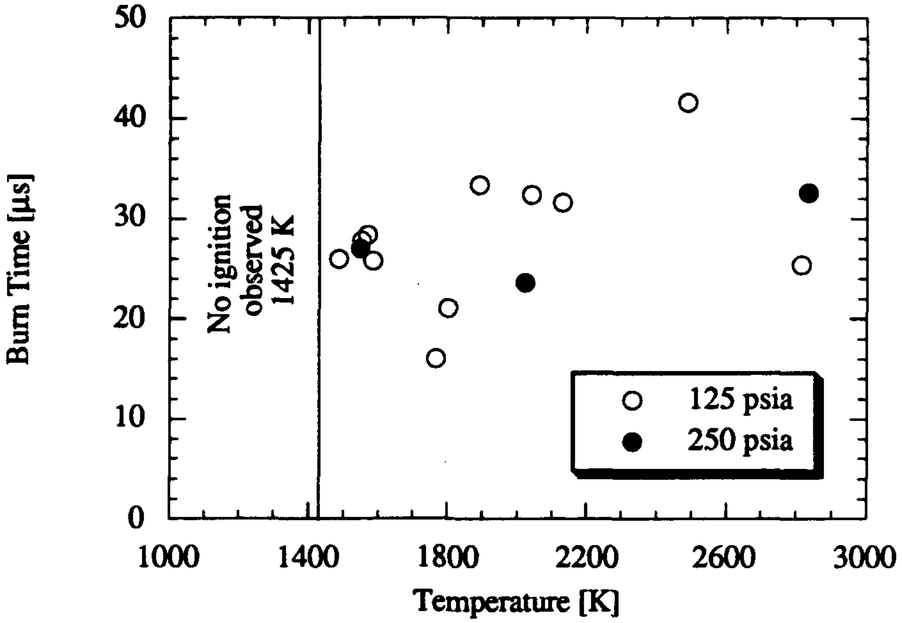

Figure 4.7 Burn time of amorphous boron versus temperature at two pressures. All conditions tested with 100% oxygen. The ignition limit, 1425 K, is found at 125 psia.

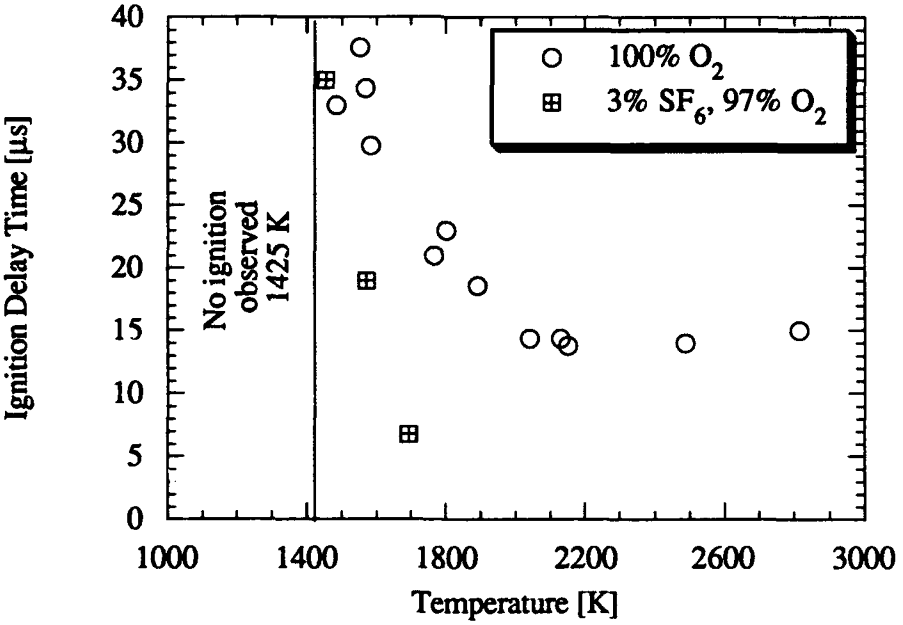

Figure 4.8 Amorphous boron ignition delay time versus temperature for various oxidizers at a nominal pressure of 125 psia.

The burn time of amorphous boron as a function of temperature is shown in Fig. 4.9. No obvious trends are observed. The SF_6 burn time appears to increase slightly with increasing temperature but the scarcity of data points prevents any definite conclusions. Also because the amorphous boron particle size is unknown, burn time studies cannot be investigated in detail. After these experiments, only 20 µm crystalline boron was examined.

4.3 Crystalline Boron Results

Since it is possible to produce specified particle sizes with sieves, the first set of experiments deal with particle size effects, to determine the optimum size to use for further experiments. Next, a limited investigation is performed with pressure effects, also with different size particles. Finally, the relationship between oxidizer mixture and ignition delay is researched in detail, to answer the question of how to reduce ignition delay time. The first sub-section will describe the nominal conditions to which the other experiments are compared.

As stated earlier, multiple signal peaks are recorded and each peak has a different origin. The third peak, which is generated as particles ignite and combust, is the focus for most of the discussion.

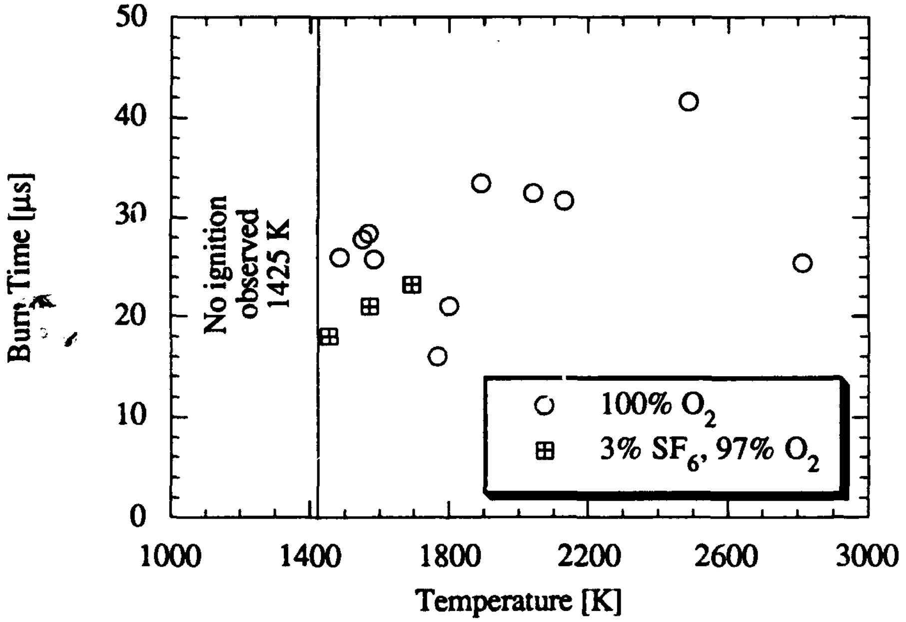

Figure 4.9 Burn time of amorphous boron versus temperature for various oxidizers at a nominal pressure of 125 psia.

4.3.1 Nominal condition

As with the amorphous boron experiments, nominal conditions are set at a pressure of 125 psia and an oxidizer gas of 100 percent oxygen. The particle size is chosen to be 20 μm for the nominal case for reasons that will be discussed in the next sub-section.

The most common signal for the nominal conditions contains four peaks, although the fourth peak does not appear for about half of the tests. Figure 4.10 depicts the ignition delay versus temperature trend for the first peak. The ignition temperature limit for the first peak is approximately 1900 K, which is found by not observing any peaks at tests below that temperature. It is evident that, although the ignition delay for all cases lie between 10 and 40 μs and there is a slight trend of decreasing delay time with increasing temperature, the scatter in the data is large enough to suggest that temperature has little effect on ignition delay time.

Other researchers [14] have discovered boron to undergo two stage ignition, where the first stage represents the particle becoming luminous for a short period of time and fading out and the second stage represents the particle reigniting and burning to completion. The first stage, quoted as being the ignition stage [1], is when the particle combustion begins but is retarded by the presence of a liquid oxide layer. The first stage ends when there is a runaway of oxide evaporation, which, in turn, cools and extinguishes the particle If the first peak represents the

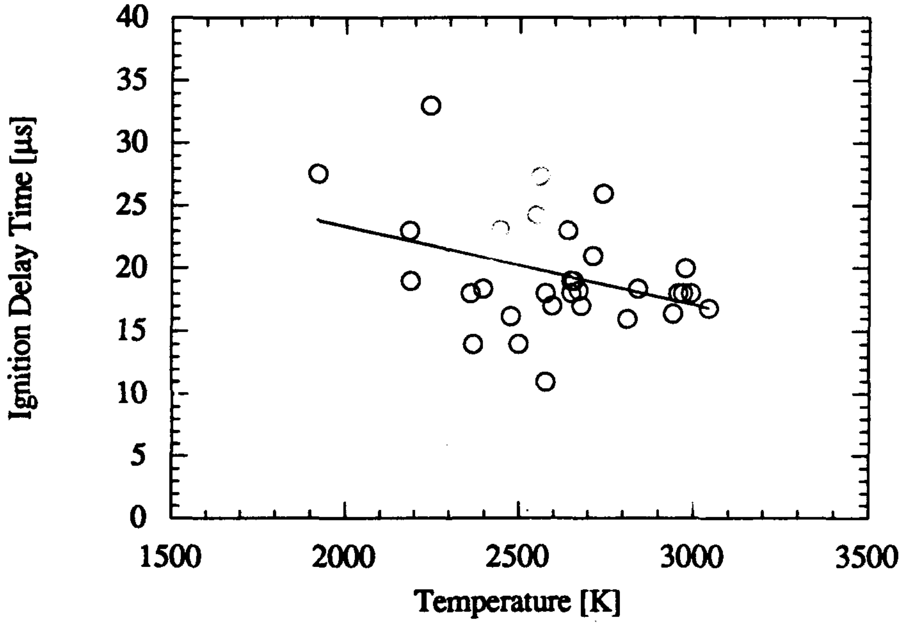

Figure 4.10 Ignition delay time versus temperature of the first peak in 100% oxygen atmosphere at 125 psia for a 20 μm crystalline boron particle sample. The line represents a linear curve fit of the data.

"parasite" particles' oxide layer evaporating, the figure would suggest that evaporation rates of boron oxide is not a function of temperature, at least for sub-micron particles. However, because of the errors in measuring the conditions and results, this portion of the experiment is not dependable for conclusive analysis of ignition delay trends.

It is plausible that this peak is generated by combustion of the parasite particles. One piece of evidence for this is that the measured ignition delay times are on the same order of magnitude as those for amorphous boron. Another piece of evidence comes from experiments performed here which utilize larger diameter boron particles with attached parasite particles. The first peak appears for these cases, with ignition delay times similar to those of Fig. 4.10 (see Section 4.3.2).

For all cases except one, the second peak is present along with the first peak. Figure 4.11 shows the ignition delay time of the second peak as a function of temperature for the nominal case described earlier. A trend of decreasing delay time with increasing temperature is more evident for the second peak. As discussed earlier, the second peak could represent the second stage ignition of the parasite particles, with the entire width of the first two peaks representing the complete combustion of those particles. One attempt to verify this was to study the time separating the two peaks. It was noticed that the time between the peaks ranged from 8 to 45 μs, but there was not any distinct trend. However, this trend could be obscured by the method of measurement of the

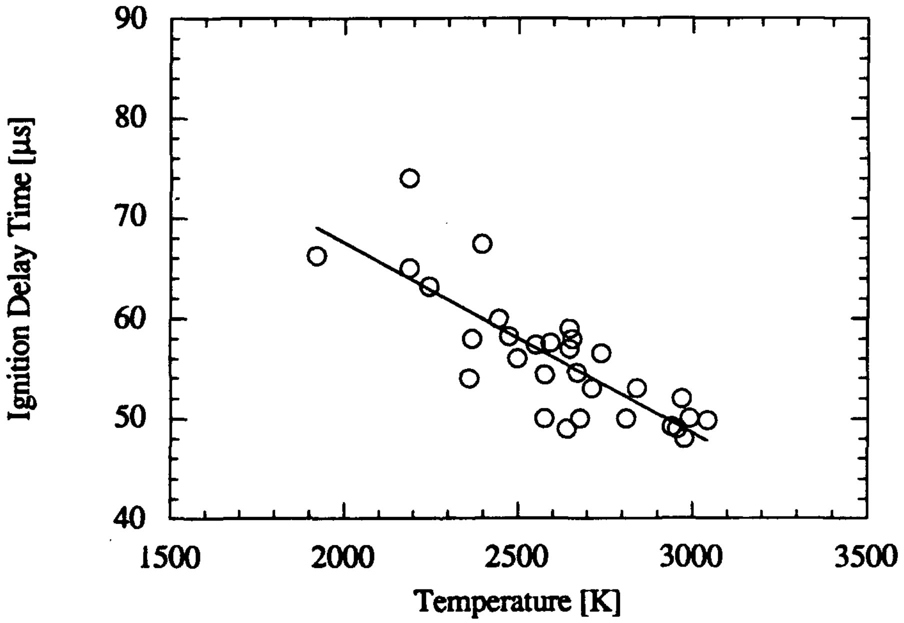

Figure 4.11 Ignition delay time versus temperature of the second peak in 100% oxygen atmosphere at 125 psia for a 20 μm crystalline boron particle sample. The line represents a linear curve fit of the data.

ignition delay of the second peak. For many cases, the second peak overlaps the first peak, starting well before the first peak falls to the initial voltage level (see Fig. 4.3). In some cases, the valley between the two peaks disappears, and is replaced by a plateau region on the back side of the first peak.

The coupling of the first and second peaks is consistent with the hypothesis linking them to the combustion of the small, parasite boron particles. Because both the first and second peak ignition delay times decrease with increasing temperature, it is likely that the two peaks are related to each other. If the second peak does represent the second stage ignition of the parasite particles, then this could not occur until first stage ignition, the boron oxide removal, was complete. Therefore, a long delay for the first peak would imply a long delay for the second peak.

Figure 4.12 displays the total experimental burn time versus temperature for the first and second peaks, using 20 μm crystalline boron particles at nominal conditions. The average method of measurement is used. The half-height method of burn time measurement discussed earlier produces inconsistent results, since sometimes the second peak is not as high as the half-height of the first peak, and therefore the burning of the second peak is not measured. In other cases, the point of measurement is near the top of the second peak, where its width does not accurately reflect the burn time, such that the scatter in the data is large, from 20 to 200 μs.

The average method of measurement is more reliable. This method measures burn time

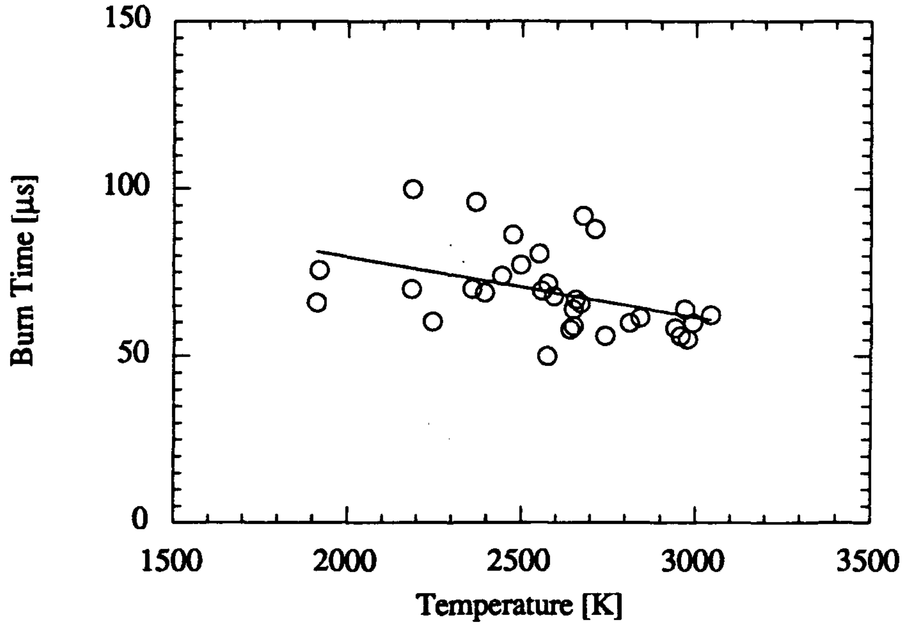

Figure 4.12 Burn time versus temperature of the first two peaks in 100% oxygen atmosphere at 125 psia for 20 μm crystalline boron particles. The line represents a linear curve fit to the data.

from the time to reach half height on the rise of the first peak to the time to fall to half height on the back side of the second peak. The results of this method are shown in Fig. 4.12. Although there is considerable scatter in the data, the burn times follow the general trend of decreasing time with increasing temperature and fall within the range of 50 to 100 μs. Once again, these burn times are characteristic of those for parasite particles.

The core of this research is the definition and explanation of the third peak signal. As discussed earlier in this chapter, the third peak is related to ignition and combustion of the main boron particles. Ignition delay time for 20 μm boron in 100% O_2 is shown in Fig. 4.13, indicating an ignition limit at 2500 K.

Tests conducted below that temperature sometimes produced a weak but readable signal that could be defined as a third peak. Because the signal was weak, there was some question as to whether ignition occurred. A no-particle shock tube test was conducted to measure background noise of the photodiode. At 2340 K, the noise peaked at 13 mV. Therefore, a criterion was set of requiring the third peak signal to have an amplitude of at least 25 mV.

Because some signals did not display a well-defined peak, a second, more qualitative criterion was developed. For some signals where the third peak is questionable, the point of maximum voltage appears right after a relatively sharp rise in voltage (see signal 58 in Appendix D). Other signals have gradual slopes leading to the peak (see signal 55 in Appendix D), and the

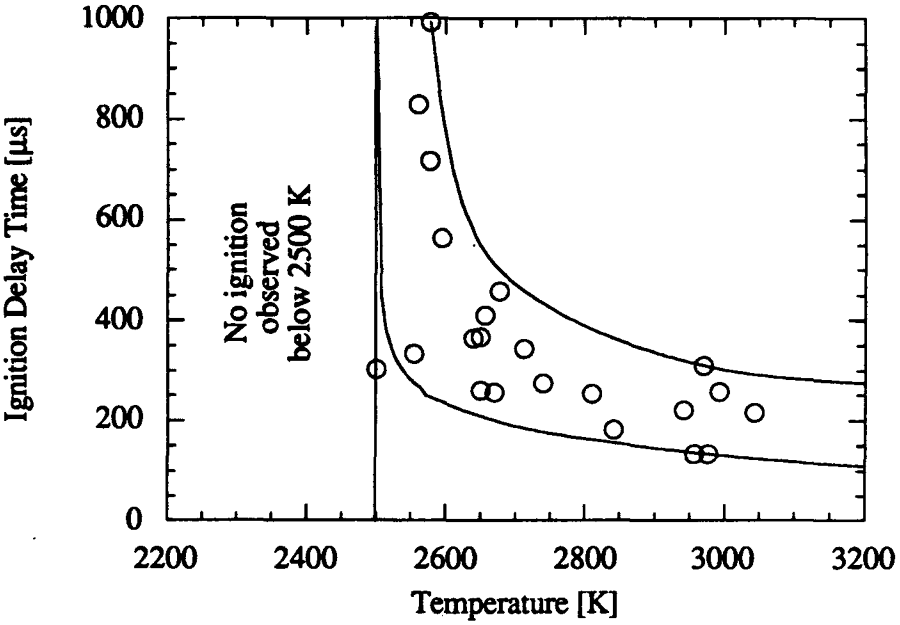

Figure 4.13 Ignition delay time versus temperature in 100% oxygen atmosphere at 125 psia for 20 μm crystalline boron particles.

downward slope following the peak voltage can also vary between steep and gradual. It was decided that both upward and downward slopes must be relatively steep for the signal to be called ignition; i.e. the peak had to "stand out" from the rest of the signal. It is recognized that this criterion is subjective and that this researcher could be biased into a certain way of thinking. Therefore, all of the signals are presented in Appendix D for future independent study. Out of 29 tests that were defined as not to having a third peak, only 9 were due to the second, more subjective criterion.

Figure 4.13 displays the results for tests meeting both criteria. The data display an ignition temperature limit of 2500 K, compared to limits as low as 1900 K found by other researchers [22]. As discussed earlier, the shock tube produces a region of constant endwall ambient conditions for at least 400 μs, followed by sharp rise in temperature for an additional 1600 μs. Ignition events occurring beyond this time window are not recorded, resulting in no *observable* ignition events below 2500 K and within 2000 μs in Fig. 4.13.

Attempts were made, nevertheless, to locate ignition events outside the 2000 μs time window. The DAS was set to record for up to 100 milliseconds, with a 20 ms duration used for most cases. A problem when recording this length of time was the intermixing of other light signals from shock tube diaphragm particles traveling the length of the shock tube and burning near the test section. These signals appeared as early as t = 10 ms. To determine if the $t > 10$ ms signals were noise or boron combustion, the experiments were repeated with boron for the same conditions. In all cases, the $t > 10$ ms signals varied as much as 60 ms from the previous experiment. Sometimes no signals were observed except for the consistent signal within the 400 μs window. It was concluded that all signals beyond 10 ms were probably caused by burning diaphragm particles burning.

The second significant result shown by Fig. 4.13 is the measured ignition delay time for temperatures above 2700 K. As shown, the ignition delay approaches a constant average value of approximately 200 μs as temperature increases. The shortest time measured for 20 μm particles is 134 μs at 2950 K. Temperatures above 3200 K could not be achieved with the shock tube so further studies were not completed. Figure 4.13 also displays considerable scatter in the data. The delay times for any one temperature vary from 150 μs to more than 700 μs near the ignition temperature limit.

The burn time 20 μm boron particles is depicted as a function of temperature in Fig. 4.14. At 3000 K, the lowest burn time measured is just above 200 μs while the highest is approaching 1.6 ms. Explanations for the scatter are discussed in Chapter 5.

A final discussion on the data from the nominal condition experiments focuses on the appearance of additional signals. With the DAS set to record for 20 ms, more peaks beyond the

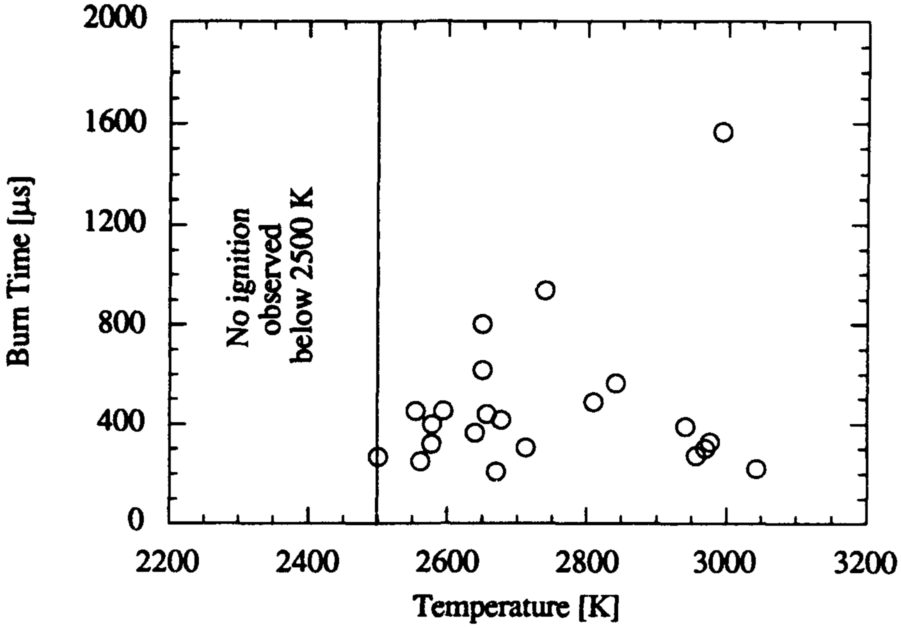

Figure 4.14 Burn time versus temperature in 100% oxygen atmosphere at 125 psia for 20 µm crystalline boron particles.

fourth peak, occasionally become visible. It is assumed that these peaks are diaphragm particles burning as discussed earlier. The fourth peak, which appeared in a majority of the tests at $t < 3$ ms, was investigated in a similar fashion as the third peak. For the most part, the voltage amplitude of the fourth peak is of the same order as the third peak, as shown in Fig. 4.5. Figures 4.15 and 4.16 display the ignition delay and burn times as a function of temperature of the fourth peak from a 20 µm particle sample at nominal conditions.

The ignition delay time of the fourth peak shows considerably more scatter than the third peak data. The boundaries vary from 500 to 6000 µs, with a similar trend with temperature as seen with the third peak.

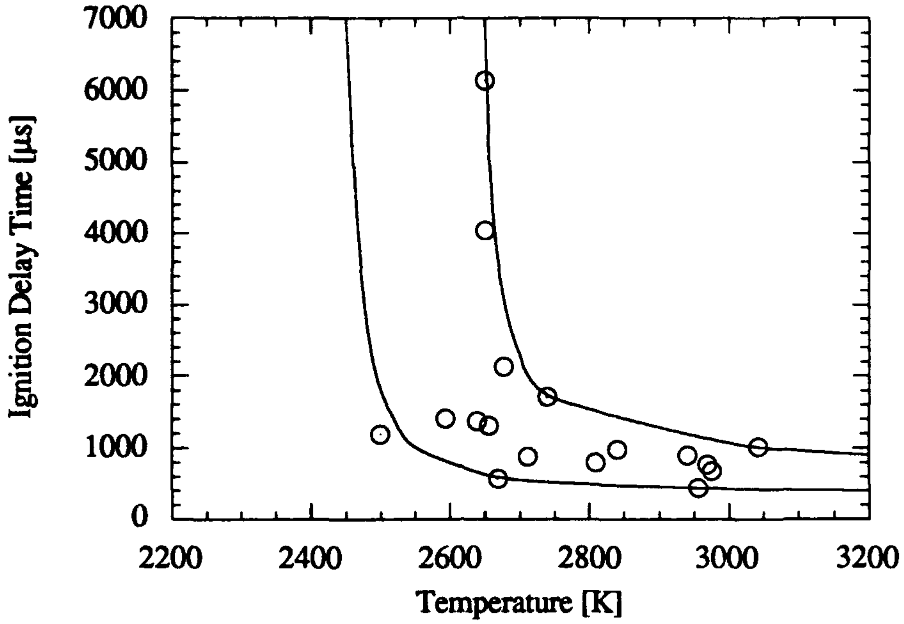

Figure 4.15 Ignition delay time versus temperature for the fourth peak in 100% oxygen atmosphere for 20 µm crystalline boron particles.

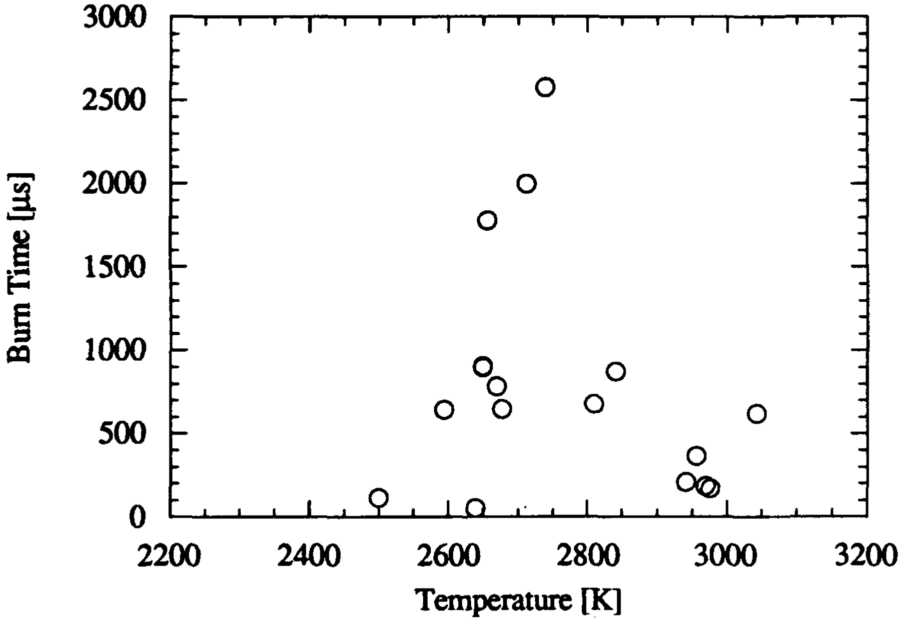

Figure 4.16 Burn time versus temperature of the fourth peak in 100% oxygen atmosphere at 125 psia for 20 µm crystalline boron particles.

4.3.2 Particle size effects

Two other size ranges, 25-32 μm and 32-38 μm, are investigated in this research for comparison to the nominal size range of 20-25 μm. As shown in Chapter 3, the average diameter of the three samples are 23, 29, and 36 μm. Experiments were performed with the three samples, referred to as 20, 25, and 32 μm for the three size ranges. All experiments in this section are conducted in 100 percent oxygen at 125 psia.

Figure 4.17 displays the trend of ignition delay time with temperature at the first peak for 20, 25, and 32 μm diameter particles. All data fall within the range between 12 and 34 μs, indicating parasite particle ignition.

The ignition delay time at the second peak as a function of temperature and particle diameter is displayed in Fig. 4.18. Again the two larger diameter particles follow the same trend as the smaller diameter particles. With the burn time versus temperature results depicted in Fig 4.19 and the results from the previous two figures, it can be concluded that similar combustion phenomena are occurring in all three samples. A more in-depth discussion is presented in Chapter 5.

Figures 4.20 and 4.21 show the trends of ignition delay and burn time with respect to temperature for three particle sizes. The first figure does not show any significant difference of ignition delay with particle diameter. However, the burn time relation with particle diameter does display some differences at the higher temperatures. At 2900 K, the burn time increases with

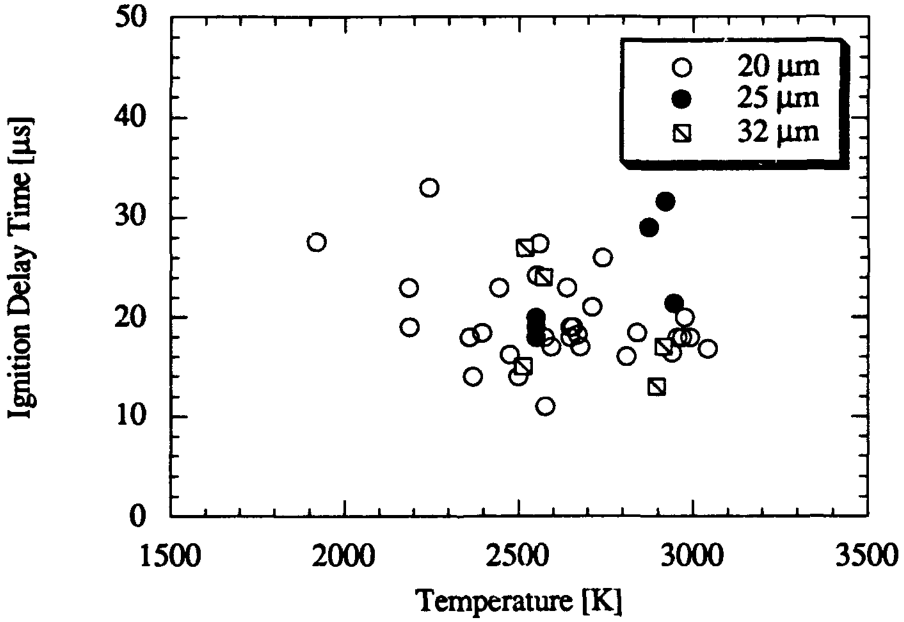

Figure 4.17 Ignition delay time versus temperature for the first peak in 100% oxygen atmosphere at 125 psia for 20, 25, and 32 μm crystalline boron particles.

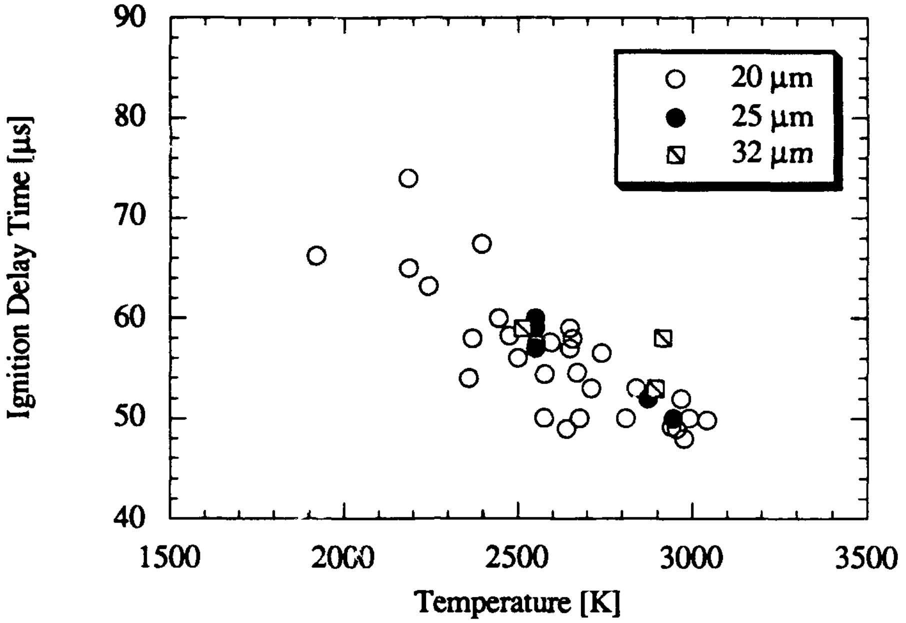

Figure 4.18 Ignition delay time versus temperature for the first peak in 100% oxygen atmosphere at 125 psia for 20, 25, and 32 µm crystalline boron particles.

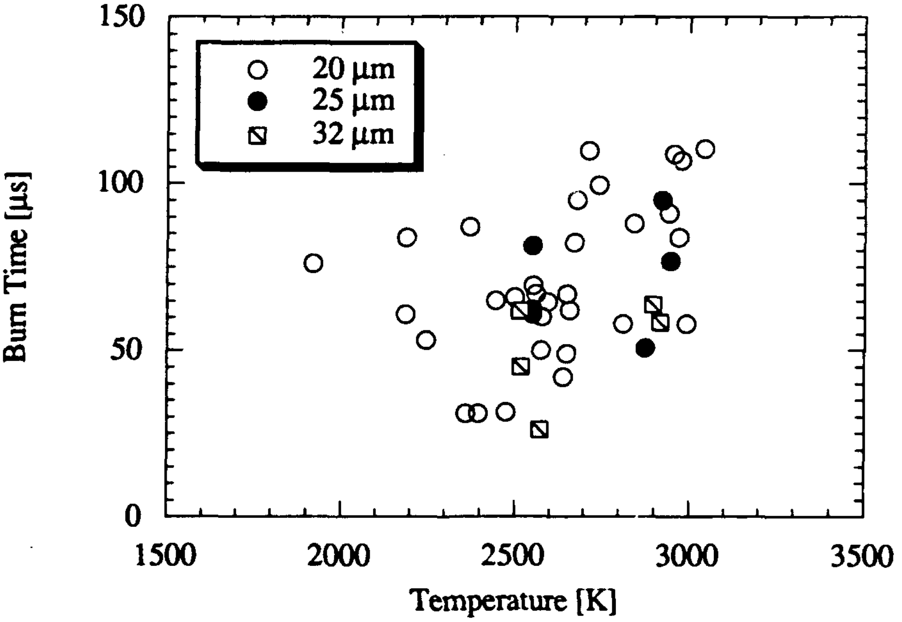

Figure 4.19 Burn time versus temperature of the first two peaks in 100% oxygen atmosphere at 125 psia for 20, 25, and 32 µm crystalline boron particles.

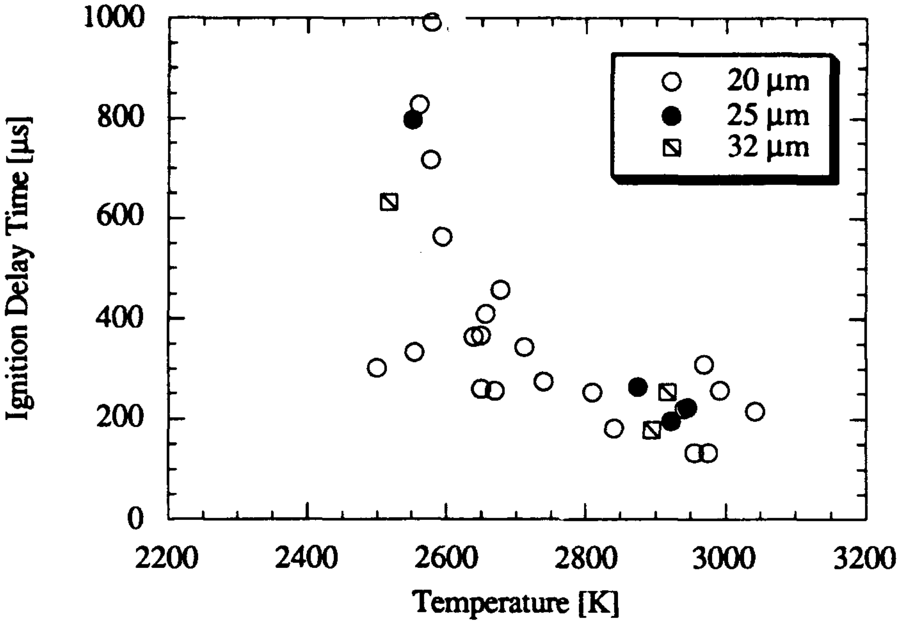

Figure 4.20 Ignition delay time versus temperature of the third peak in 100% oxygen atmosphere at 125 psia for 20, 25, and 32 μm crystalline boron particles.

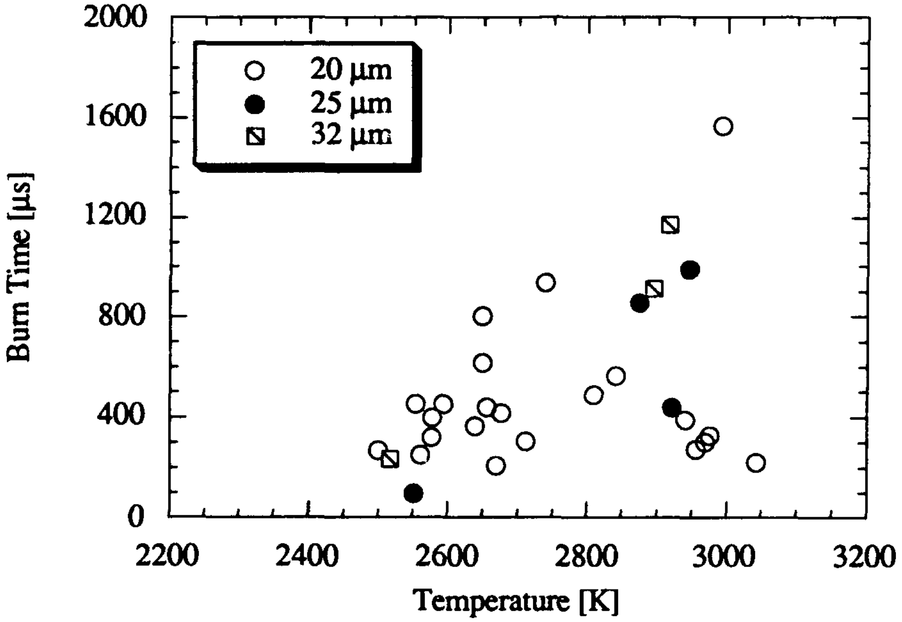

Figure 4.21 Burn time versus temperature of the third peak in 100% oxygen atmosphere at 125 psia for 20, 25, and 32 μm crystalline boron particles.

particle size, as expected. At the lower temperatures (2550 K) the burn time of the larger diameter samples is the same as, if not slightly lower than, the 20 µm particle burn time. This could be due to incomplete combustion at those temperatures. At temperatures above 2750 K, the burn time of the 20 µm particles generally decrease with increasing temperature as mentioned above and found elsewhere [16].

4.3.3 Pressure effects

For the next set of experiments, the pressure behind the reflected shock wave was varied to study the effect on ignition delay and burn time. Three pressures were examined: 125, 250, and 500 psia (0.86, 1.72, and 3.44 MPa). All experiments were conducted in 100% oxygen and used 20 µm boron particles.

Figure 4.22 displays the results of the ignition delay time of the first peak as a function of temperature and pressure. Once again, the scatter for all cases is sufficient to obscure a general trend. As with the particle size experiments, the pressure experiments yield ignition delay times between 12 and 34 µs.

The second peak ignition delay time for higher pressures, shown as a function of temperature in Fig. 4.23, displays no discernible pressure effect. For the 500 psia case, the scatter is not as great as with the 125 psia case, although only a few experiments at high temperature were completed. If one were to perform a linear curve fit with the data for each pressure, the 500 psia case would display a slightly greater ignition delay time than the 125 psia case for all temperatures.

Figure 4.24 display the burn time for the first two peaks at three different pressures. The mean burn time for the 500 psia pressure experiments falls below the mean burn time for the nominal 125 psia case. It appears that pressure has a small effect on the burn time of sub-micron particles.

Figure 4.25 illustrates the results from the study of ignition delay time of the third peak at three different pressures. There appears to be a slight decrease in ignition delay for the 500 psia case compared to the 125 psia case for similar temperatures. A majority of the 500 psia points below 2700 K have ignition times under 180 µs, with the average around 160 µs (see Appendix C for the actual time of each data point). At lower temperatures, the ignition delay of the high pressure case is lower than the low pressure case. There is one point showing ignition at 2050 K, although the signal had more than four peaks within 2 ms possibly indicating particle shattering (see Appendix D, shot 73).

The data for burn time at different pressures (Fig. 4.26), show a similar trend above 2700 K. At lower temperatures, the data are scattered around burn times of 250 to 500 µs for the three different pressures. Thus, burn time does not appear to be a function of pressure.

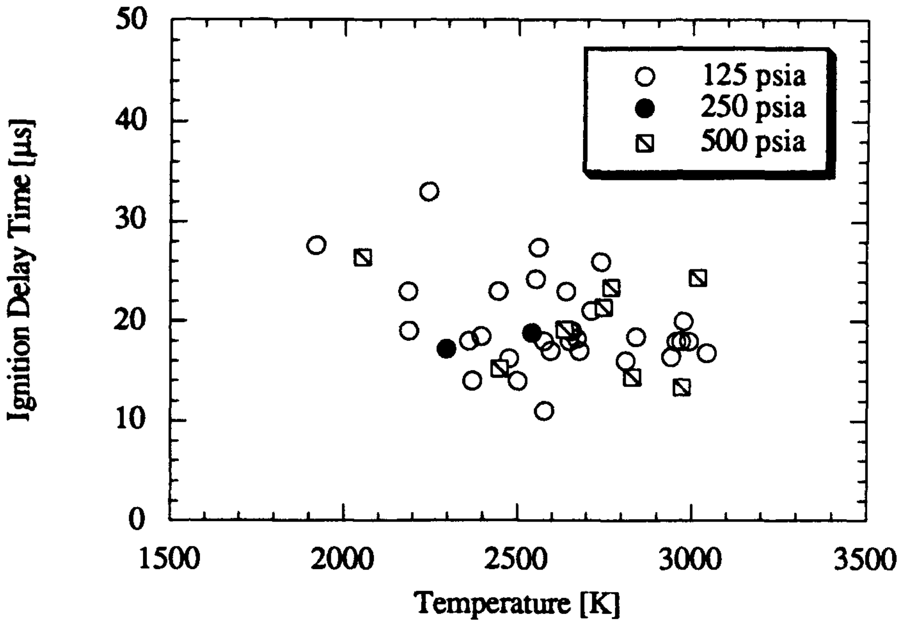

Figure 4.22 Ignition delay time versus temperature of the first peak in 100% oxygen atmosphere for 20 μm crystalline boron particles at pressures of 125, 250, and 500 psia.

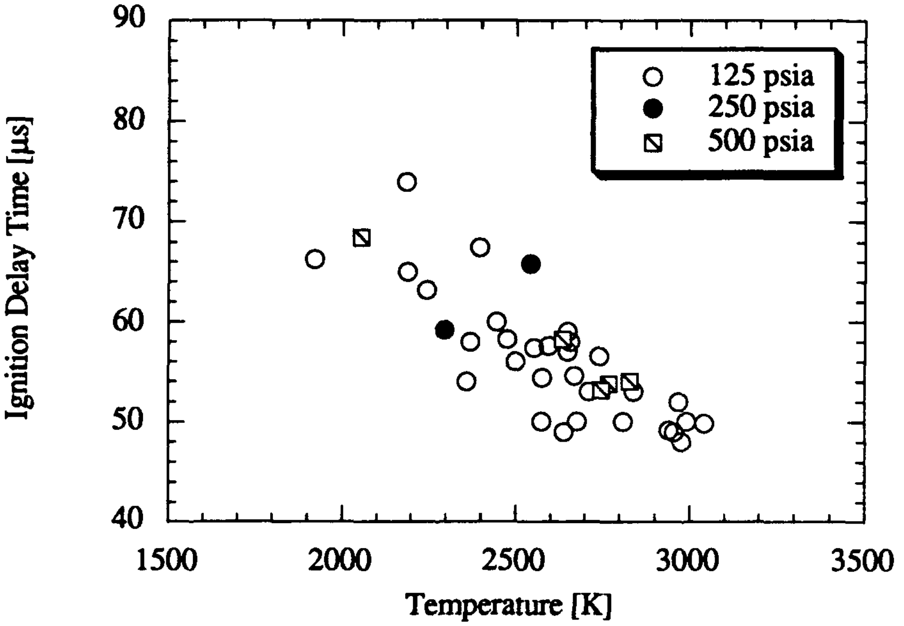

Figure 4.23 Ignition delay time versus temperature of the second peak in 100% oxygen atmosphere for 20 μm crystalline boron particles at pressures of 125, 250, and 500 psia.

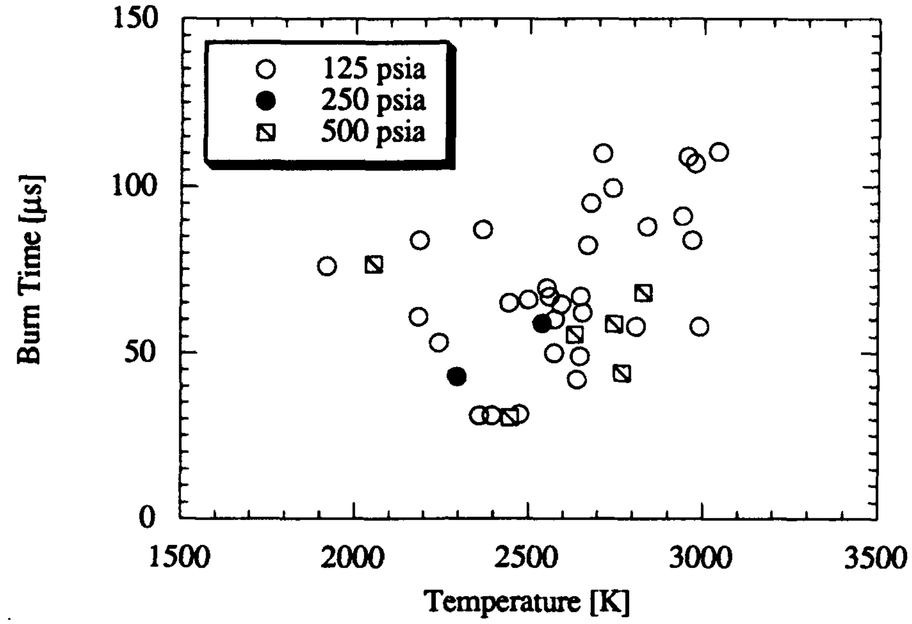

Figure 4.24 Burn time versus temperature of the first two peaks in 100% oxygen atmosphere for 20 μm crystalline boron particles at pressures of 125, 250, and 500 psia.

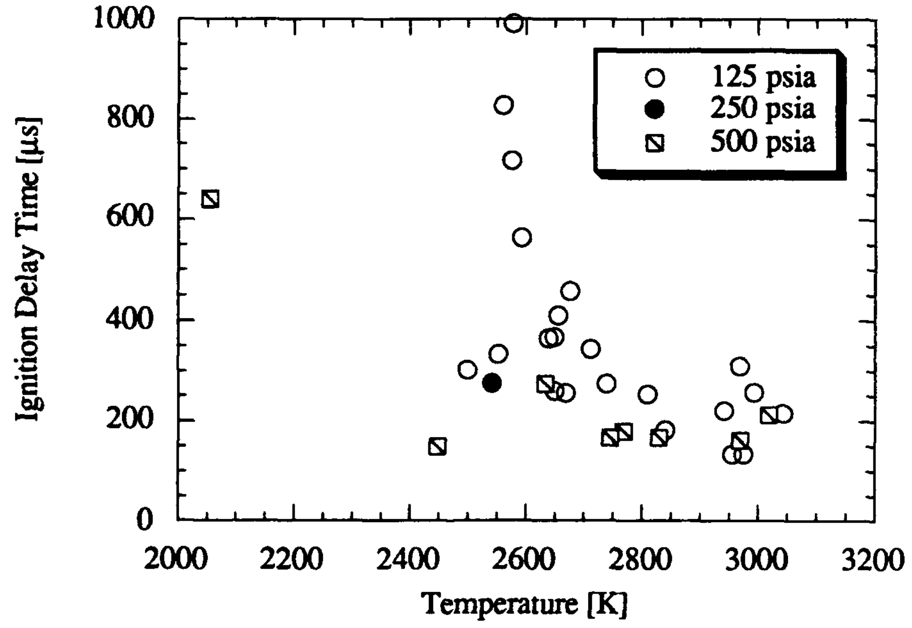

Figure 4.25 Ignition delay time versus temperature of the third peak in 100% oxygen atmosphere for 20 μm crystalline boron particles at pressures of 125, 250, and 500 psia.

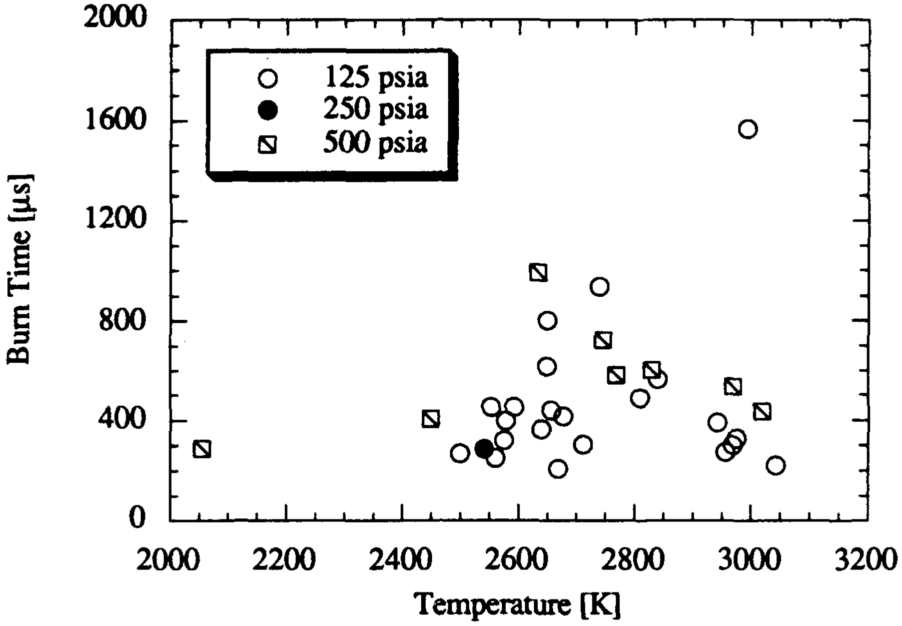

Figure 4.26 Burn time versus temperature of the third peak in 100% oxygen atmosphere for 20 μm crystalline boron particles at pressures of 125, 250, and 500 psia.

4.3.4 Oxidizer effects

The main focus of this research is to determine if fluorine or fluorine-containing compounds affect the combustion history of boron particles. Sulfur hexafluoride, which dissociates its fluorine atoms easily, and hydrogen fluoride, which does not dissociate substantially at the temperatures examined, are the two fluorine-containing compounds studied. A set of experiments is also conducted with water vapor to confirm the results of past researchers. Two different concentrations of each fluorine compound are investigated for comparison. All of the experiments discussed in this section are conducted at a nominal pressure of 125 psia in an oxidizing atmosphere of oxygen plus additive.

This section initially focuses on the first two peaks of the photodiode signal. Figure 4.27 illustrates the results of the ignition delay time as a function of temperature and oxidizing atmosphere. Ignition is observed to occur between 7 and 34 μs. Both the 30% H_2O and the 1% SF_6 data suggest a trend of decreasing ignition delay with increasing temperature. This trend could be used to describe the pure oxygen data as well (see Fig. 4.10). However, no trends in ignition delay are evident with 2% SF_6 or either HF oxidizing mixtures.

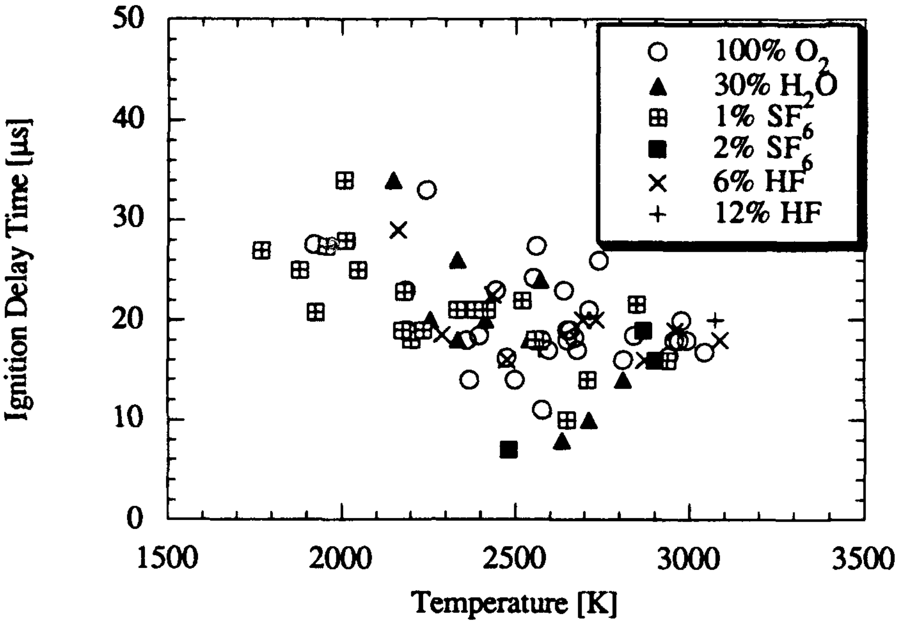

Figure 4.27 Ignition delay time versus temperature of the first peak for several oxygen plus additive mixtures of 20 µm boron particles at 125 psia.

The ignition delay time for the second peak versus temperature as a function of oxidizing mixture is depicted in Fig. 4.28. For the most part, except for hydrogen fluoride, the oxidizing mixtures follow the same trend of decreasing ignition delay time with increasing temperature. No distinct trend is displayed for the hydrogen fluoride experiments for the narrow temperature range studied. The water vapor data show slightly lower ignition delay times than oxygen. On the other hand, SF_6 appears to have slightly higher ignition delay times than oxygen. However, for the SF_6 experiments, only 3 shots out of 20 produced a second peak. It is highly possible that the second peak was obscured by the first peak, rendering the second peak SF_6 trend inconclusive.

Figure 4.29 displays the results for the burn time of the first two peaks. If the second peak was not present, the burn time of the first peak, measured by the half-height method, was substituted. As can be seen, there is no obvious relation of burn time with temperature for any of the oxidizing mixtures. The burn time ranges from 18 to 110 µs when combining all cases. When comparing oxidizing mixtures, the water vapor and hydrogen fluoride data are similar to the oxygen data. However, the sulfur hexafluoride data is grouped below that of the oxygen, with no burn time exceeding 70 µs. The lack of a second peak would account for the low times but the reason for the missing peak is unclear.

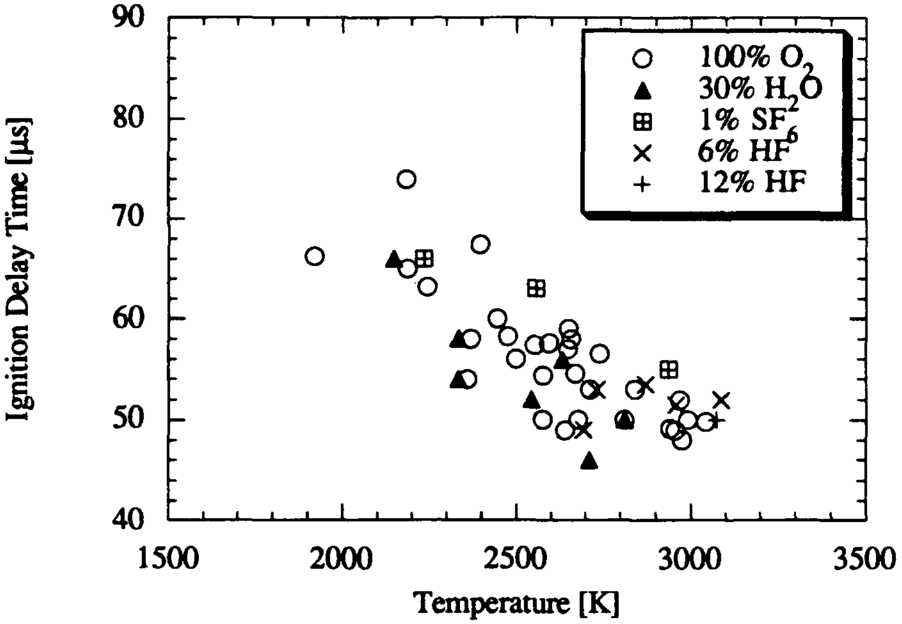

Figure 4.28 Ignition delay time versus temperature of the second peak for several oxygen plus additive mixtures of 20 μm boron particles at 125 psia.

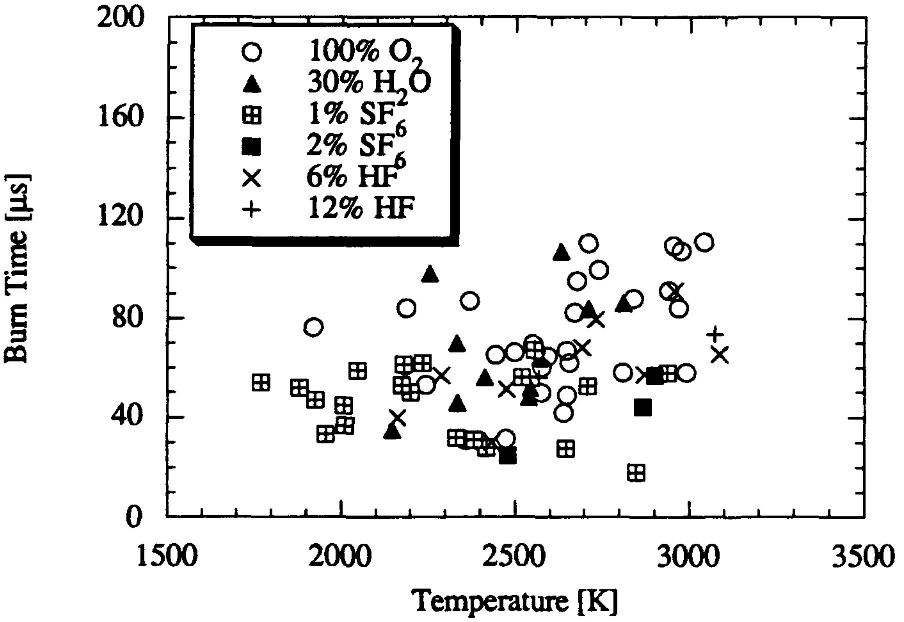

Figure 4.29 Burn time versus temperature of the first two peaks of several oxygen plus additive mixtures of 20 μm boron particles at 125 psia.

The ignition delay time and burn time of the third peak are illustrated in Figs. 4.30 through 4.35, where each oxidizer additive is compared to 100 percent oxygen to highlight specific results. Figure 4.30 compares the ignition delay of boron in water vapor and in oxygen. Below 2600 K, the ignition delay is reduced when water vapor is used. Also, no ignition is observed below 2200 K with water vapor and below 2500 K with oxygen. Finally, at temperatures above 2500 K, both oxidizers yield similar ignition delay times around 200 μs, indicating that a boron ignition delay time limit has been reached.

Figure 4.31 shown the third peak burn time results in water vapor and oxygen. Despite considerable scatter in the water vapor data, there is a trend of decreasing burn time with increasing temperature.

Figure 4.32 illustrates the effect SF_6 on third peak ignition delay time. Clearly there is a 600 K reduction in the ignition temperature limit. The limit for SF_6 is 1900 K compared to 2500 K for the oxygen limit and 2200 K for the water vapor limit. For temperatures above 2400 K, the ignition delay time remains roughly constant at approximately 200 to 300 μs. When comparing the 1% and 2% mole fractions of SF_6, there is no discernible difference.

Third peak burn time results (Fig. 4.33) show a constant value for SF_6 of approximately 400 μs for all temperatures studied. The burn time is similar to the oxygen case burn time, indicating that fluorine does not increase the rate of combustion but reduces the ignition temperature.

A side note on the SF_6 experiments concerns the profile of the photodiode signal. At temperatures close to the 1900 K ignition temperature limit for SF_6, the third peak was relatively easy to measure, compared to signals for O_2 at temperatures close to its 2500 K ignition temperature limit (see Appendix D). There was also less "noise" in many of the SF_6 shots. For a majority of the SF_6 cases, a fourth peak was not evident. This will be discussed further in Chapter 5.

Figure 4.34 illustrates the third peak ignition delay results from the hydrogen fluoride experiments. The ignition delay times are very similar to the oxygen case, but with larger scatter around a 200 μs mean, and with no ignition observed below 2450 K. There does not appear to be a trend of decreasing ignition delay time with increasing temperature over the range studied.

The burn time results depicted in Fig. 4.35 also do not indicate any significant difference between the HF and oxygen cases, even when using greater concentrations of hydrogen fluoride. It would appear that hydrogen fluoride does not contribute to the combustion of boron.

Two other HF shots, shown in the figures, were taken at 250 psia (see Appendix C). These were done at temperatures above 3000 K to see if there was any change in the ignition delay time limit. The lowest ignition delay observed was 180 μs and the burn time was 400 μs, similar to the 125 psia case and supporting the observation that HF has a limited effect on boron

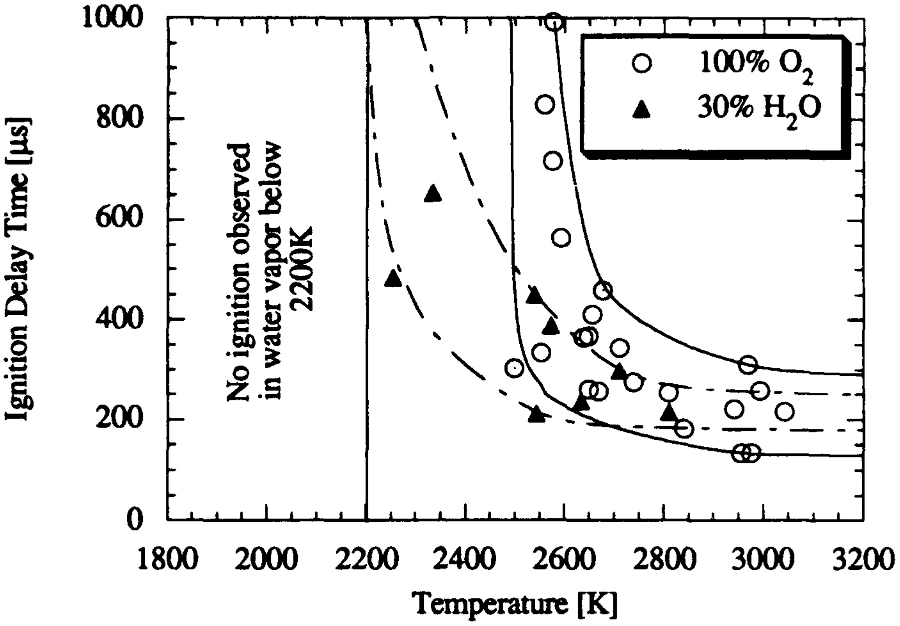

Figure 4.30 Ignition delay time versus temperature of the third peak comparing water vapor and oxygen for 20 μm boron particles at 125 psia.

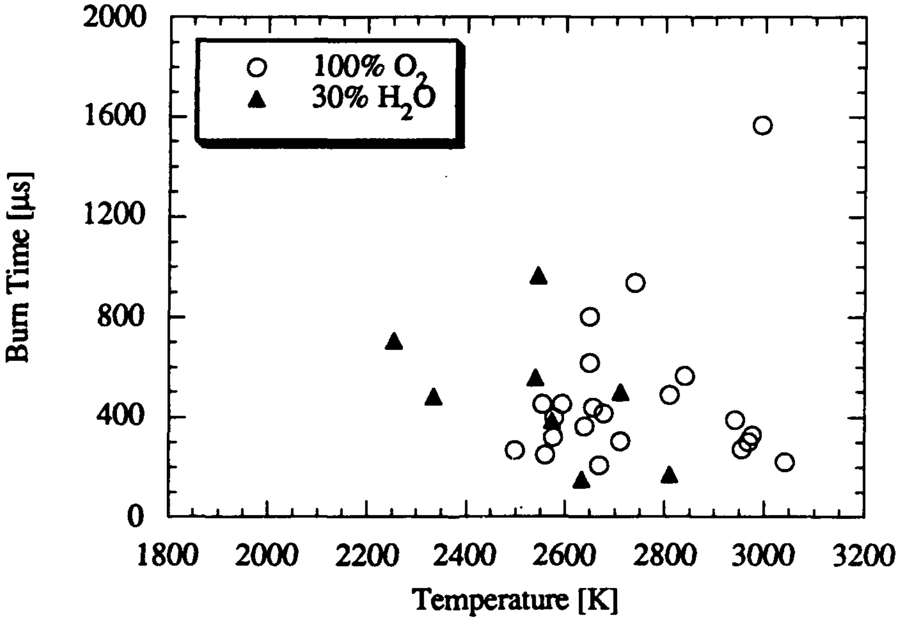

Figure 4.31 Burn time versus temperature of the third peak comparing water vapor and oxygen for 20 μm boron particles at 125 psia.

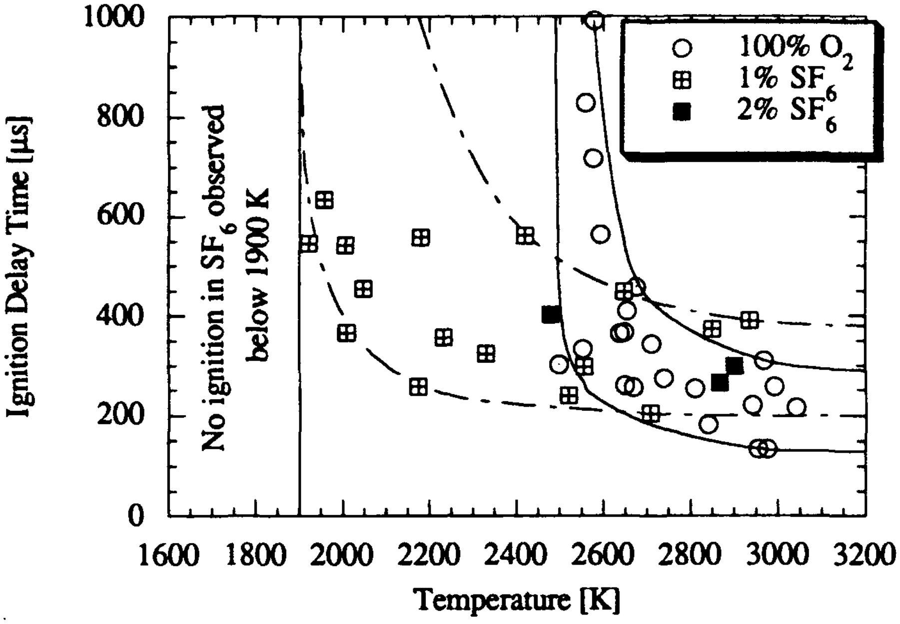

Figure 4.32 Ignition delay time versus temperature of the third peak comparing SF_6 and O_2 for 20 μm boron particles at 125 psia.

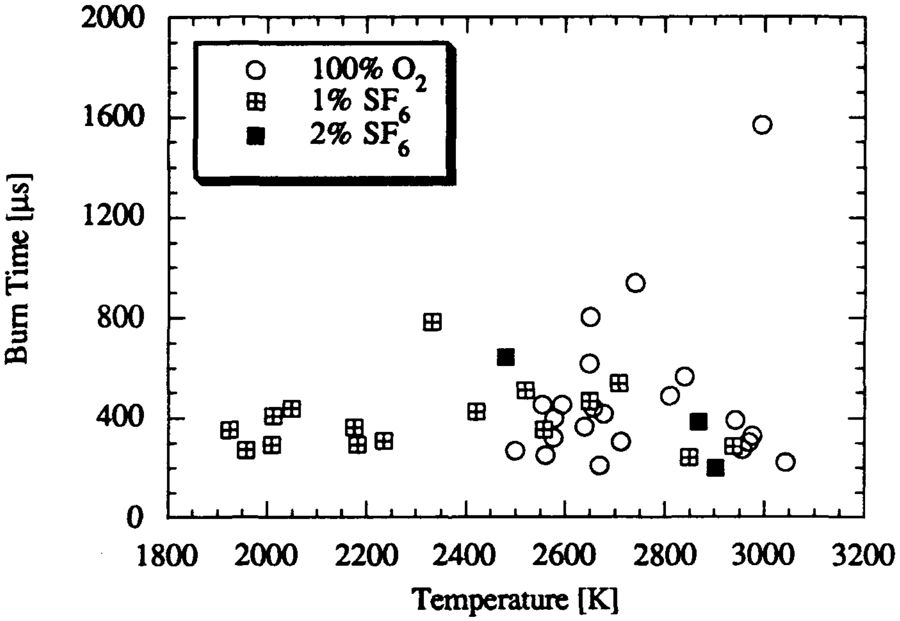

Figure 4.33 Burn time versus temperature of the third peak comparing SF_6 and O_2 for 20 μm boron particles at 125 psia.

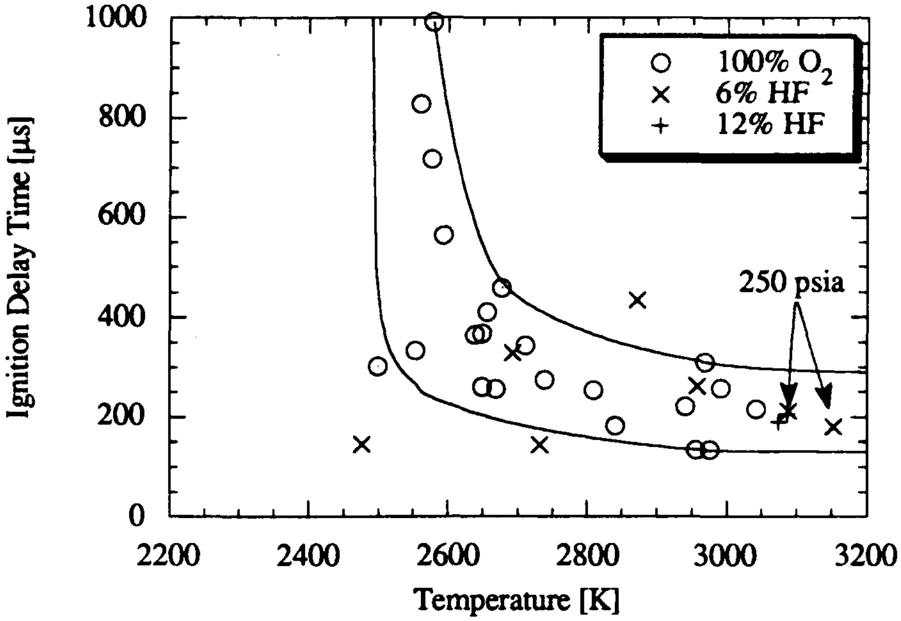

Figure 4.34 Ignition delay time versus temperature of the third peak comparing HF and O$_2$ for 20 µm boron particles at 125 psia.

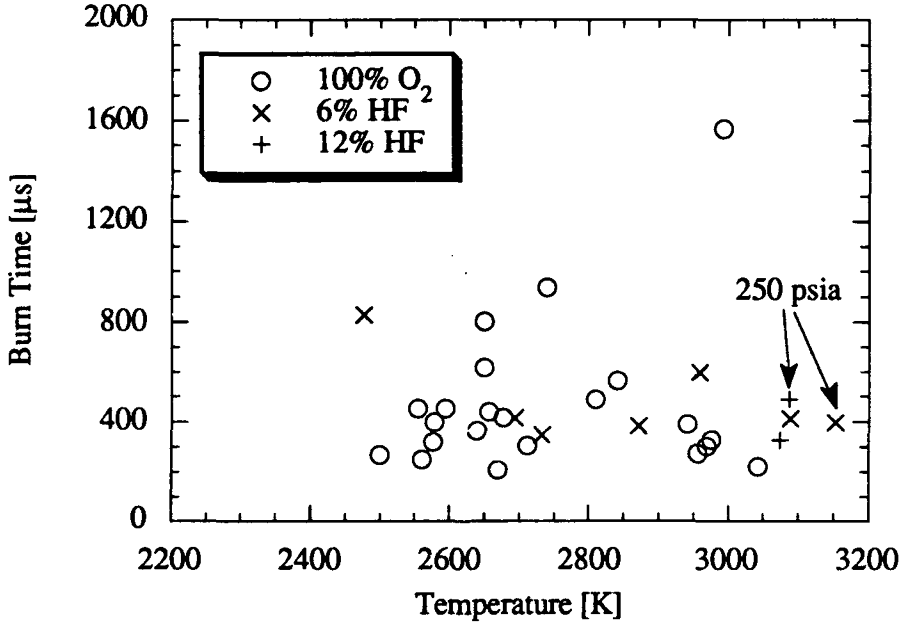

Figure 4.35 Burn time versus temperature of the third peak comparing HF and O$_2$ for 20 µm boron particles at 125 psia.

combustion.

To summarize, water vapor and sulfur hexafluoride show a reduction of ignition temperature limit when compared to oxygen, with SF_6 showing the greater reduction. However, no significant changes in the ignition time limit at high temperatures were observed.

4.4 Error Analysis

Because there is considerable scatter in the data, an examination of the errors involved in the measurement is in order. Four parameters are in question: reflected temperature, reflected pressure, ignition delay time, and burn time. For the time measurements, most of the error comes from the researcher's decision of where to choose the midpoint of the peak. As for uncertainty of the recorder, most of the cases were operated at a recorder frequency of 5 MHz. This yields an uncertainty of ±0.2 μs, which is on the order of a one percent error of the first peak measurement and one-tenth of a percent for the third peak measurement. The cases where the acquisition system was set to record for over 10 ms had a maximum uncertainty of ±5 μs. This would cause the first peak measurement to be considerably inaccurate but the third peak would still have less than 3% error.

The uncertainties of the temperature and pressure, which are calculated from the NASA Gordon-McBride code, are dependent on the uncertainties of the inputs used to the program. Both temperature and pressure are functions of initial temperature, initial pressure, the incident shock wave Mach number, and the mole fraction of the gases in the driven section and are represented as follows:

$$T_5 = f_1\left(T_1, P_1, M_{S_i}, y_{gas}\right) \tag{4.1}$$

$$P_5 = f_2\left(T_1, P_1, M_{S_i}, y_{gas}\right) \tag{4.2}$$

Using the approach given by Holman [36], the uncertainties in T_5 and P_5 can be expressed as:

$$w_{T_5} = \left[\left(\frac{\partial T_5}{\partial T_1} w_{T_1}\right)^2 + \left(\frac{\partial T_5}{\partial P_1} w_{P_1}\right)^2 + \left(\frac{\partial T_5}{\partial M_{S_i}} w_{M_{S_i}}\right)^2 + \left(\frac{\partial T_5}{\partial y_{gas}} w_{y_{gas}}\right)^2\right]^{1/2} \tag{4.3}$$

$$w_{P_5} = \left[\left(\frac{\partial P_5}{\partial T_1} w_{T_1}\right)^2 + \left(\frac{\partial P_5}{\partial P_1} w_{P_1}\right)^2 + \left(\frac{\partial P_5}{\partial M_{S_i}} w_{M_{S_i}}\right)^2 + \left(\frac{\partial P_5}{\partial y_{gas}} w_{y_{gas}}\right)^2\right]^{1/2} \tag{4.4}$$

where w_i represents the uncertainty in variable i.

The initial temperature and pressure uncertainty is based on the resolution of a mercury thermometer and an analog vacuum pressure gauge, which are taken to be ±0.1 K and ±0.1 kPa, respectively. When modifying the laboratory for hydrogen fluoride, the vacuum gauge had to be replaced. The new gauge has a resolution of ±0.2 kPa.

The uncertainties for Mach number and additive mole fraction are calculated from the uncertainties of the initial temperature, pressure, and sidewall location of the pressure transducers from the relations:

$$M_{S_i} = \frac{V_{S_i}}{\sqrt{\gamma R T_1}} \tag{4.5}$$

$$y_{gas} = 1 - \frac{p_{gas}}{P_1} \tag{4.6}$$

An analysis similar to the calculation of the reflected pressure and temperature uncertainties is completed for Equations 4.5 and 4.6, with the error in p_{gas} the same as P_1. The error in the velocity comes from the error in the pressure transducer location which is assumed to be ±2.54 mm.

Figures 4.36 and 4.37 illustrate the temperature and pressure uncertainty estimates for each oxidizer mixture case. The calculations were done at three temperatures for each case. For the oxygen, water vapor, and hydrogen fluoride cases, the uncertainty in temperature is always less than 75 K, which is 4 percent of the test temperature.

The uncertainty estimates for SF_6 are slightly higher. At approximately 2400 K, the

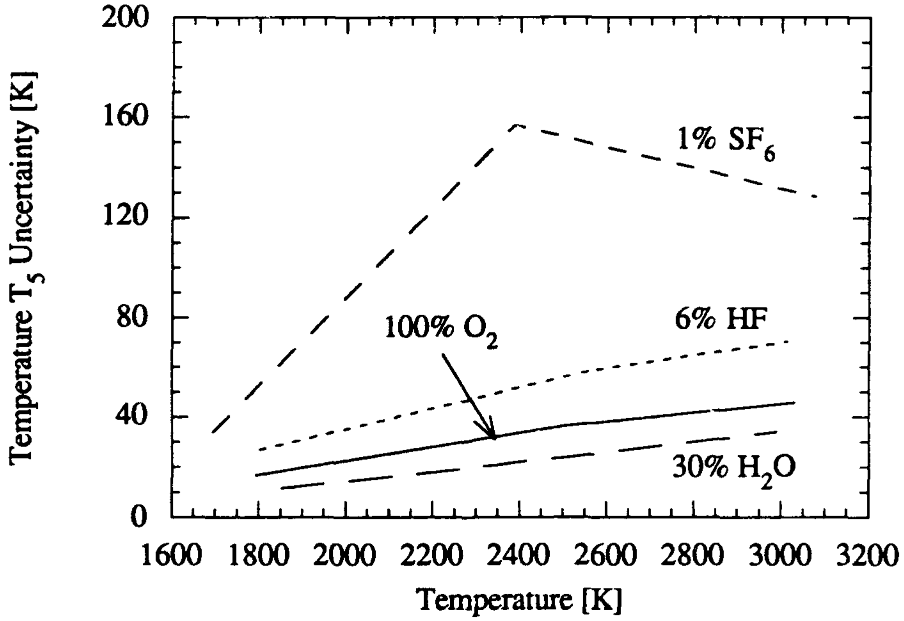

Figure 4.36 Temperature T_5 uncertainty as a function of temperature and oxidizer mixture at a test pressure of 860 kPa (125 psia). The partial mole fraction gases are complemented with oxygen.

temperature uncertainty is ±160 K which is approaching an error of 7%. When doing the sensitivity analysis, it was discovered that the temperature for SF_6 experiments is a strong function of mole fraction. Considerable energy is absorbed by the dissociation of sulfur hexafluoride. Any slight increase in the mole fraction results in more energy absorbed and less energy available to increase the gas temperature. Figure 3.22 illustrates this relationship.

The pressure uncertainty is similar for the O_2, H_2O, and SF_6 peaking at approximately 7% (±60 kPa) of the nominal pressure (860 kPa). The HF uncertainty is strongly influenced by the pressure gauge resolution. A gauge resolution of 0.2 kPa compared to 0.1 kPa almost doubles the error. However, the error is still less than 9%, so any trends that are evident are reasonably reliable.

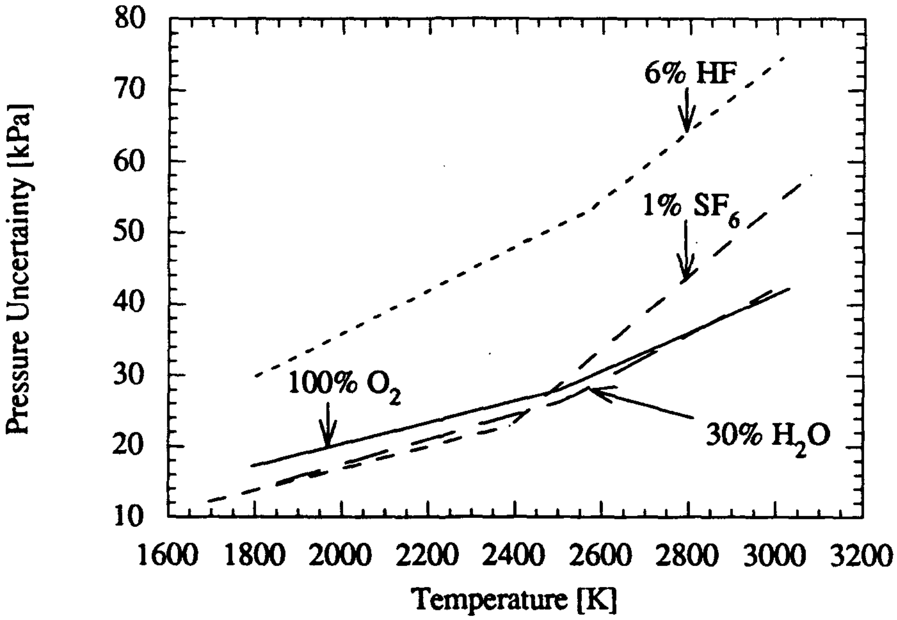

Figure 4.36 Pressure uncertainty as a function of temperature and oxidizer mixture at a test pressure of 860 kPa (125 psia). The partial mole fraction gases are complemented with oxygen.

CHAPTER 5 - ANALYSIS OF RESULTS

When examining the results of the previous chapter, it was noticed that the ignition delay and burn times were an order of magnitude less than the results of previous research on boron combustion. This chapter focuses on linking past and present research together and developing possible explanations to describe the observable trends of ignition delay and combustion of boron.

5.1 Current Research Summary

The current research focused on the shock tube study of the ignition and combustion of amorphous and crystalline boron at elevated pressures. Ignition delay and combustion trends with temperature were examined for different crystalline particle sizes, pressures, and oxidizing gas additives. The experimental conditions ranged from 1400 to 3200 K, 125 to 500 psia, and sub-micron to 32 μm particle diameters. The additives consisted of 30% H_2O, 1-3% SF_6, and 6-12% HF, which were complemented with oxygen. The results from these experiments are presented in Chapter 4.

Chapter 4 also discusses the light signal that the boron sample produces when combusting. For a majority of the crystalline boron cases, each signal has three or four peaks of light output (see Figs. 4.2 and 4.5). This research interprets each peak as a different combustion event. The first two peaks are claimed to be sub-micron particles, which are present as parasites on each crystalline boron sample, and which ignite and combust in two stages. The third peak is suggested to represent the combustion event of the larger crystalline particle. The fourth peak definition is interpreted as the combustion of a shattered larger particle.

5.2 Comparison to Previous Experimental Research

Previous amorphous boron research is extremely limited and few qualitative results are published. Gurevich, et al. [20] discovered that amorphous boron agglomerates ignite at lower temperatures than crystalline boron particles of the same size. This behavior was also evident in this research where the amorphous boron ignition limit is 1425 K and the crystalline limit is 1900 K for particles smaller than 10 μm in diameter. As for ignition and combustion times, Mohan and Williams [10], using a 5000 frame/s camera, found 150 μm amorphous boron agglomerates to ignite in less than 200 μs and to burn completely in less than 1 ms. This research discovered ignition times less than 40 μs and burn times less than 50 μs. Mohan and Williams' framing resolution was only 200 μs so the 40 μs ignition delay time found in this research falls within their uncertainty. As for burn time comparison, apart from the different pressures studied, they had considerably larger particles and smaller mole fractions of oxygen (0.5) which could account for the longer burn time.

It is suggested that the first two peaks represent parasite sub-micron particle combustion. Uda [21] did shock tube ignition studies of 0.015 μm boron particles and found ignition delay to be less than 100 μs at temperatures above 1400 K. This research shows results of the same order of magnitude as Uda, which is consistent with sub-micron boron particle combustion. Also, from all of the past research on combustion of crystalline boron greater than 20 μm in diameter, there has been no evidence published of any portion of the ignition or combustion process occurring on a time scale of less than 100 μs. This suggests that the first two peaks are not the result of the combustion of the primary 20 μm particles.

Li, et al., [23, 37] also conducted experiments using sub-micron particles and discovered a two stage combustion process. They injected a jet of particles into a flat-flame burner and found three flame regions; a yellow zone corresponding to the ignition stage, a white-glow zone representing the combustion of the particle with removed oxide layer, and a green luminous zone representing the emission of the combustion products. The white region could not be measured accurately because it had a small height, but the burn time was estimated to be below 100 μs. The white region corresponds to the second peak and the burn times for both Li and this research are the same order of magnitude.

Li's ignition (yellow zone) results, corresponding to an ignition and oxide burn time of 2 ms, show a significant difference of more than an order of magnitude with the present results (70 μs). Li's long ignition times could be due to the differences in the experimental set-up or to his lower pressure operation. (Li's flat flame burner used a mixture of methane, oxygen, and nitrogen, where the oxygen mole ratio ranged from 0.08 to 0.80 and experiments were conducted at one atmosphere.) However, Uda's ignition delay results (< 100 μs) and Li's burn time results (< 100 μs) are consistent with a sub-micron particle combustion model for the first two peaks.

The third peak, because of its weak light intensity at low temperatures, needs to be examined carefully. Conditions close to the ones examined here were achieved by Macek and Semple [16]. They experimented on 37 μm crystalline boron particles at elevated pressures for different mole fractions of oxygen. However, their set-up utilized a laser to heat the particles to 2000 K, which could account for the significant differences between the two sets of results. For their tests with 40/60 O_2/N_2 at 7.8 atm, they found an ignition delay time of 2 ms. The highest observable ignition delay time in this research was 1 ms, but a majority of the results averaged to be 200 μs. Recall that in this research, the shock tube particles were heated up to 2500 K, were ignited in 100% oxygen, and had a smaller diameter. Also the particles here remain in the hot oxidizing gases, while Macek's particles, once falling past the laser beam, saw oxidizing gases at room temperature.

Comparing burn times here with Macek and Semple shows a larger discrepancy. Their 37 μm particle burned for 11 ms while our 20 μm particle burned for an average of 400 μs, a factor of 30 less. This discrepancy is possibly caused by the mole fraction of oxygen. In an earlier work by Macek and Semple [22], when comparing burn times of 75 μm particles at one atmosphere, combustion in oxygen (7 ms) was nearly an order of magnitude less than combustion in air (50 ms). Therefore, it is possible that the difference between the burn times is due to experimental conditions.

5.3 Observable Trends

5.3.1 Amorphous boron

One result from the amorphous boron data is the ignition temperature limit of 1425 K. Signals between 1425 and 1600 K are weaker than higher temperature signals, implying that the ignition limit is being approached. Only one other ignition limit with oxygen was found in the literature [12], which gives 1073 K for one atmosphere in air. The difference in the limit for this research is probably due to the particle size and elevated pressure.

Another ignition delay trend is that ignition delay time decreases with increasing temperature between 1425 and 2000 K (Fig. 4.6) and asymptotically approaches 15 μs. Pressure differences have little effect.

Fluorine atoms appear to accelerate amorphous boron ignition, as shown in Fig. 4.8. Fluorine additive data approach the same lower temperature limit as oxygen, but the ignition delay is reduced. Burn times with SF_6 do not change significantly compared to oxygen burn times. A reduction in ignition delay by fluorine without affecting burn time is consistent with a physical model in which fluorine only assists in accelerating the boron oxide removal. This presumes that amorphous boron has an oxide layer similar to crystalline boron, although this is not stated in the literature.

5.3.2 Sub-micron crystalline boron

Given that the first peak represents the first stage ignition of sub-micron crystalline boron, then the following conclusions can be reached. First, the experimental ignition limit for sub-micron particles in 100% O_2 is found to be 1900 K. This limit was found elsewhere [14] for larger particles. Although the ignition limit for sub-micron particles was not the focus of this research and limited data were taken at low temperatures with additives, it is found that using SF_6 reduced the ignition limit below 1750 K (a lower limit was not determined).

First stage ignition delay time does not vary with pressure or oxidizer, and is a weak function of temperature. If the first peak represents boron particle combustion while oxide still coats the particle, then the data indicate that the diffusion rates of oxygen or boron through the oxide layer are not a function of pressure or temperature, and that oxidizer additives do not assist in oxide removal at the beginning of the stage.

The second stage ignition (second peak), where the particle reignites after the oxide layer has been removed, is strongly dependent on temperature, since the ignition delay decreases with increasing temperature. This suggests two conclusions. First the particle heat up is accelerated with increasing temperature and second, the oxide is removed at a faster rate. The second stage ignition delay with water vapor is decreased slightly compared to oxygen. However, the SF_6 second peak apparently overlaps the first peak for many cases, so few delay times were measured. Therefore, both additives appear to assist in the oxide removal.

Hydrogen fluoride does not produce any effect on the ignition delay of either the first or second peak. It was suggested [17] that HF would help remove the oxide layer, even before heating up the particle. However, from the results, HF does not appear to assist in any portion of the boron combustion process for the pressures tested.

Burn times of sub-micron boron are not significantly affected by temperature, pressure, or oxidizer. For all cases, the burn time falls between 20 and 110 μs.

5.3.3 20 micron crystalline boron

For the nominal case of 20 μm boron in 100% O_2 at 125 psia, there are three notable characteristics. First, there appears to be an ignition temperature limit of 2500 K. Note that this limit exceeds both the boiling point of the boron oxide (2316 K) and the melting point of the boron particle (2350 K). This would indicate that for the particle to ignite, the boron oxide must be removed, which is concluded by other researchers [1]. If this is the case, the result should hold for the parasite particles as well. However, the ignition limit of the parasite particles is around 1900 K. A possible explanation for this is that the temperature of the particle is not necessarily known. As discussed in Chapters 1 and 2, boron particles experience both self-heating due to chemical reactions and self-cooling due to the evaporation of the oxide. The smaller particles could ignite at the lower temperature if self-heating was comparatively more important for small particles than for large.

The second characteristic is the decrease of ignition delay with increasing temperature between 2500 and 2800 K. The third characteristic is an asymptotic approach to an ignition delay time of 200 μs at higher temperatures.

Using different size particles did not change any of the trends described above. Previous researchers [16] also indicated that particle diameters below 54 μm exhibit no particle size effect on ignition delay time. However, increasing the pressure from 125 to 500 psia did lower the ignition delay time, at least at the high temperature asymptotic value. This could imply that the ignition is diffusionally controlled, where oxygen reaches the boron by diffusing through the oxide layer to initiate combustion.

The effect of the oxidizer additives is to change the ignition temperature limit. Water vapor decreased the limit from 2500 K to 2200 K, and SF_6 decreased it to 1900 K. Hydrogen fluoride did not change the temperature limit or the ignition delay limit when compared to pure oxygen. If H_2O and SF_6 assist in the removal of the oxide layer, the ignition delay time should be reduced, but this is not observed.

Burn time results for the nominal condition showed considerable scatter possibly due to incomplete combustion. From Fig 4.14, most of the burn times below 2700 K are in the range of 200 to 800 μs with no relationship observed between burn time and temperature. However, above 2700 K, there appears to be a trend of decreasing burn time from 900 to 200 μs with increasing temperature. The 500 psia case also follows the same trend. Larger particles do not show longer burn times until a temperature of 2900 K is reached (Fig. 4.21). All of these trends would suggest that below 2700 K, the particles do not burn completely.

As for oxidizer effects, the change in burn time is negligible. This leads to the conclusion that additives do not accelerate the reaction rate of boron but react with the boron oxide.

As stated before, for some of the experiments, fourth and even fifth peaks are observed (Appendix D). Because they are infrequent and non-reproducible, the fourth peaks are not considered as another stage of combustion. However, the third and fourth peaks seem to be related. One possible suggestion is that the main particles break apart during combustion and ignite at later times. Another possibility is that the particles stick together on the knife blade prior to combustion and subsequently separate.

The widely scattered fourth peak burn time data in Fig 4.16 could support either conclusion. In fact, the fourth peak has both low and high burn times, ranging from 170 to 2600 μs, compared to the third peak range of 200 to 900 μs (Fig. 4.14), which implies that both scenarios could occur.

CHAPTER 6 - CONCLUSIONS AND RECOMMENDATIONS

A brief summary and the major conclusions from the experimental results of the ignition and combustion of boron particles are presented in this chapter. Recommendations are proposed to solve some of the problems with the apparatus and to verify the steps involved in boron combustion.

6.1 Conclusions

Based on the experimental measurements of boron ignition in pure oxygen, the following conclusions can be drawn:

1) Amorphous boron has an ignition limit of 1425 K at pressures above 8.5 atm and ignition delay times decrease with increasing temperature from 40 μs to an asymptotic value of 15 μs at 2000 K. Higher pressures have negligible effects.
2) Sub-micron crystalline particles have an ignition temperature of 1900 K at pressures above 8.5 atm and exhibit a two stage combustion phenomenon. The first stage varies insignificantly with temperature but the second stage ignition delay decreases with increasing temperature. Higher pressures do not have any effect on either stage.
3) 20 μm crystalline particles ignite in less than 1 ms at temperatures above 2500 K and approach the ignition delay time limit of 200 μs at 2700 K for pressures above 8.5 atm. Increases in particle size or pressure show no effects.

When examining the burn times, the evidence leads to the following conclusions:

1) Amorphous boron burn times do not change with temperature or pressure.
2) Sub-micron crystalline boron burn times do not change with temperature or pressure.
3) Larger crystalline boron particles exhibit two different burn time trends for two different temperature regions. Below 2700 K, particles burn for approximately 400 μs, for all pressure cases and particle sizes studied. Above 2700 K, there appears to be a trend of decreasing burn time with increasing temperature, which is evident for both the 125 and 500 psia case. Also above 2700 K, larger particles burn for longer durations. This is suggestive of incomplete combustion at temperatures below 2700 K.

With additives, the results indicate the following conclusions:

1) Water vapor as an additive reduces the ignition delay of the second stage of sub-micron crystalline boron. For larger particles, water vapor reduces the ignition temperature to 2200 K. However, it does not change the ignition delay time limit of the larger particles or the burn time

of either group of particles. Therefore, it would appear that water vapor only assists in the removal of the oxide layer.

2) Sulfur hexafluoride reduces the ignition delay time of amorphous boron and is assumed to do the same for the second stage of sub-micron particles, although the actual signal is not measured for the later case due to interference of the first stage signal. SF_6 reduces the ignition temperature for the larger particles to 1900 K, but does not change the ignition delay time limit. Using different amounts of SF_6 does not affect the ignition delay. No amount of SF_6 changes the burn time. All of this would lead to the conclusion that fluorine plays a significant role in the kinetic reaction with boron oxide.
3) Using hydrogen fluoride does not display significant differences in ignition delay or burn time trends when compared to pure oxygen. Increasing the amount of HF does not change the results. Therefore, hydrogen fluoride does not enhance the chemical kinetics with boron or boron oxide as predicted by other researchers [17].

6.2 Recommendations

There were some problems with the experimental technique that need improving to verify the results found in this research. The first concerns the presence of the parasite particles. To verify that the first peak in the photodiode signal is parasite particle combustion and not some other aspect of the large particle combustion process, the parasite particles should either be completely removed from the large particles, or just a sample of sub-micron particles should be examined. The problem with the current set-up is that the smallest sieve has 20 μm openings, so the particles that fall through have a size range of 20 μm to < 1 μm.

The problem stated above can be approached in another way, and that is to spectroscopically observe the combustion process. If each peak of the signal represent a different reaction mechanism which produce different end-products, then the first peak could be related to the combustion of the larger particles and not to the parasite particles. However, even if the spectroscope determines that the first peak represents the smaller particles, then there is still possibly a problem that the energy released from their combustion assists in the larger particle's combustion. Therefore, removing the smaller particles would be a distinguishing test for the origin of the first two peaks.

The spectroscope could be used for another portion of the experiment; to determine the products of combustion when additives are used. One of the reasons fluorine is suggested as an additive is that, when it reacts with boron it produces BF_3, which is energetically superior to B_2O_3. However, this product is simply derived from kinetic modeling and has not been observed by anyone to date.

The ignition delay and burn times of 20 µm crystalline boron, measured here do not display the long ignition delay other researchers have experienced for temperatures above 2700 K. The boron becomes a liquid droplet at that temperature and the oxide layer would be evaporated. Future work in modeling the combustion process of the liquid droplet is in order, with an emphasis on the reaction rates between boron and oxygen as well as with water vapor and fluorine.

As for recommendations for future experiments, it would be desirable to search for reasons why hydrogen fluoride did not change the ignition delay times. One possible theory is that it is necessary to dissociate HF, which cannot be done at the relatively low temperatures in the shock tube. Future experiments using water vapor and sulfur hexafluoride together might answer this question.

As of the time of this study, work is being done at our laboratory on an apparatus to observe the combustion events at higher temperatures and pressures than are obtainable in the shock tube. Pressures as high as 10,000 psia and temperatures approaching 5000 K are theoretically possible for this device and therefore is capable of supporting research on the combustion of gaseous boron.

The most important recommendation is that an accurate kinetic model, with fluorine, is necessary for any future studies with boron. It is obvious that fluorine assists in the combustion process. In fact, it appears to alleviate the long ignition delay at relatively low temperatures that has hindered the use of boron as a fuel.

APPENDIX A - NUMERICAL SOLUTION OF THE UNSTEADY ONE-DIMENSIONAL SHOCK TUBE PROBLEM[¥]

This appendix summarizes the results obtained for the numerical solution of a one-dimensional unsteady shock tube problem. A shock tube is a type of apparatus which allows experimental tests to be performed at high pressures and temperatures by sending a shock wave through a tube and reflecting the wave off the end wall which raises the temperature and pressure of the contained gas. At time $t = 0$, the tube is initialized with a high pressure driver gas in one section while the other section is evacuated. The two sections are separated by a membrane (see Fig. A.1) which is broken at time $t > 0$. The breaking of the membrane and the pressure differential creates a shock wave that moves through the evacuated section and an expansion wave which propagates back through the high pressure driver gas.

The shock wave sent through the evacuated section of the shock tube reflects off the end wall and moves back through the gases. The reflected shock produces a further increase in the temperature and pressure of the gas, and also brings the gas to rest. Immediately after the reflected shock wave passes, the gas experiences a time where the temperature, pressure, and density are constant. This time is referred to as the test time. Eventually, the expansion waves will pass and create disturbances which change the uniform conditions present during the test time. The reflected

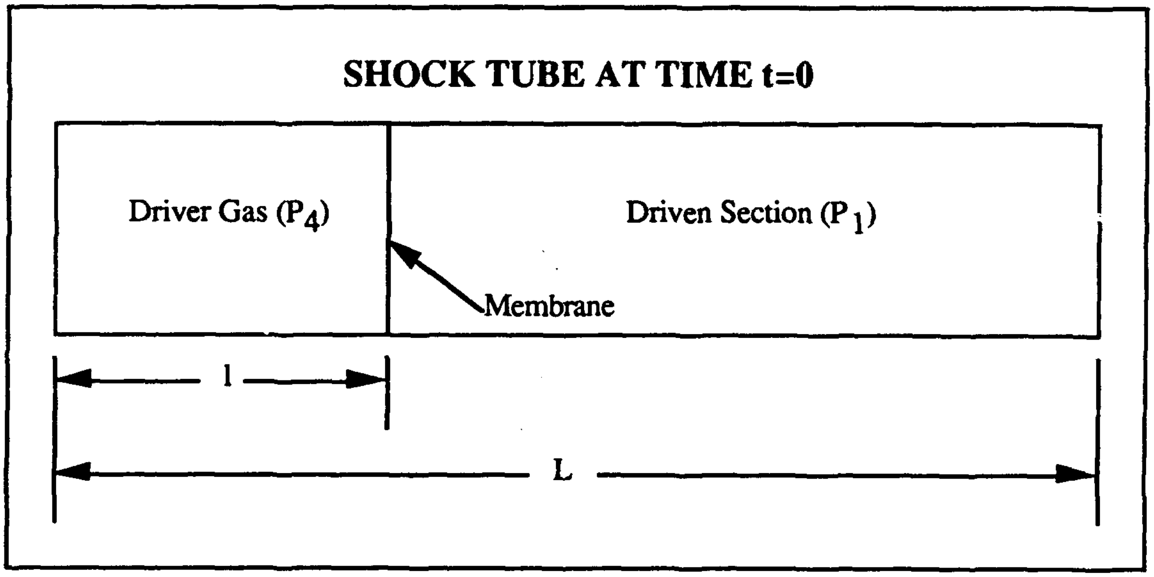

Figure A.1 Shock tube diagram at $t = 0$.

[¥] This appendix was prepared by Ph.D. candidate Lisa A. Orth, currently working on a thesis of modeling detonations of explosives containing metals.

pressure ratio (P_5/P_1) which exists before the expansion wave passes and the test time are two of the desired results.

The governing equations are the conservation of mass, momentum and energy equations, additionally, an ideal gas equation of state was used. For the one-dimensional unsteady problem, the Eulerian formulation of the conservation equations are given by:

$$\frac{\partial \rho}{\partial t} + \frac{\partial (\rho u)}{\partial x} = 0 \tag{A.1}$$

$$\frac{\partial (\rho u)}{\partial t} + \frac{\partial (\rho u u)}{\partial x} = -\frac{\partial P}{\partial x} \tag{A.2}$$

$$\frac{\partial \rho e}{\partial t} + \frac{\partial (\rho u e + u P)}{\partial x} = 0 \tag{A.3}$$

The numerical method used to solve this set of differential equations was the program EBTFCT developed by Gross and Baer at Sandia National Laboratory [38] for use on the Cray computer. This method solves the one-dimensional unsteady hyperbolic partial differential equation of the form:

$$\frac{\partial \rho}{\partial t} = -\frac{1}{r^{\alpha-1}}\frac{\partial}{\partial r}\left(r^{\alpha-1}\rho v\right) + \frac{1}{r^{\alpha-1}}\frac{\partial}{\partial r}\left(r^{\alpha-1}D_1\right) + C_2\frac{\partial D_2}{\partial r} + D_3 \tag{A.4}$$

where D_1, D_2 and D_3 represent source terms and C_2 is a constant. Also, alpha is set at 1, 2 or 3 for cartesian, cylindrical and spherical coordinates, respectively. These general finite difference subroutines allow the user to create a driver program for any problem which requires the solution of the above partial differential equation in either cartesian, cylindrical or spherical coordinates. The Sandia report included, as an example, a driver program for the one-dimensional unsteady Riemann problem described above for a uniform gas (i.e. the driver and driven gases have the same specific heat ratio).

This program was run for low and high initial pressure ratios for both air and helium as the medium. The results obtained are presented here. Figure A.2 shows the pressure and temperature ratios at the wall for air at an initial pressure ratio of $P_4/P_1 = 7$. Additionally, the driver section was initialized at $l/L = 0.25$ for all results presented here. For low pressure ratios, the program was very stable and a clear test time was observed.

As the initial pressure ratio was increased, the program became less stable. These instabilities are observed in Figs. A.3 and A.4 which provide the temperature and pressure profiles at the wall for air and helium at high initial pressure ratios. Overall, the finite difference solver was sensitive to the number of grid points used and to the courant number stability condition which needed to be decreased at higher pressure ratios. A grid of 300 nodes was used for the results

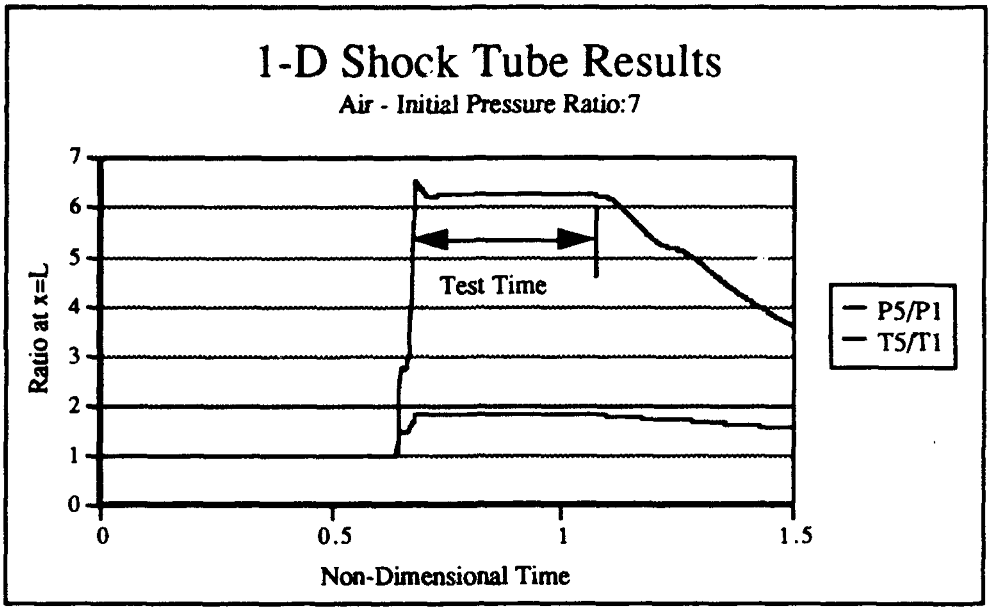

Figure A.2 Numerical results for air with a low pressure ratio.

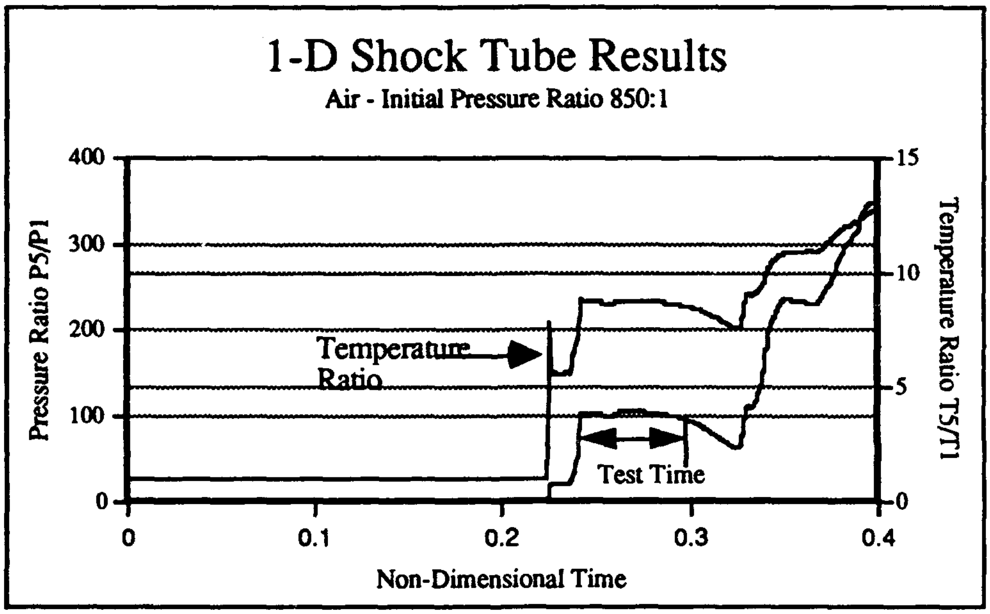

Figure A.3 Numerical results for air with a high pressure ratio.

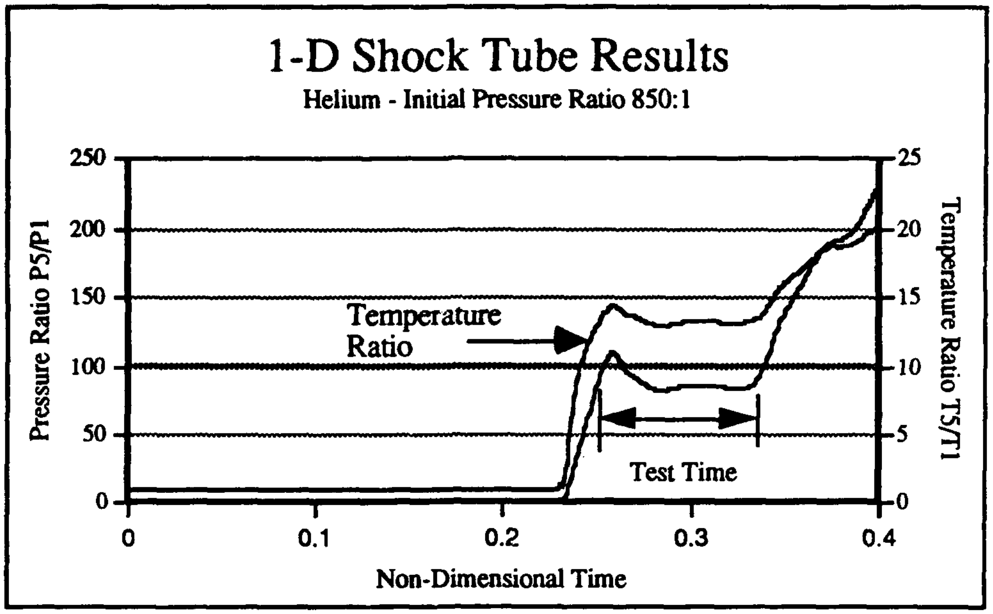

Figure A.4 Numerical results for helium with a high pressure ratio.

presented here. The converted test times for a shock tube of 39 ft with the above operating conditions are given in Table A.1 along with the approximate pressure ratio P_5/P_1.

Two techniques were utilized the check the accuracy of the program results. First, a comparison of the numerically predicted pressure ratio (P_5/P_1) was made with the predicted reflected pressure ratios using a steady-state analysis of a shock tube problem. The numerical solution before the expansion wave interrupts the test time should be the same as the steady state solution. The steady state solution is given by Anderson [33] and begins by solving for incident shock pressure ratio (P_2/P_1) as a function of the initial pressure ratio (P_4/P_1) using the equation

$$\frac{P_4}{P_1} = \frac{P_2}{P_1}\left\{1 - \frac{(\gamma_4 - 1)(a_1/a_4)(p_2/p_1 - 1)}{\sqrt{2\gamma_1\left[2\gamma_1 + (\gamma_1 + 1)(p_2/p_1 - 1)\right]}}\right\}^{\frac{-2\gamma_4}{(\gamma_4 - 1)}} \qquad \text{(A.5)}$$

Table A.1 Summary of numerical results

Pressure Ratio P_4/P_1	Test Time (milliseconds)	Pressure Ratio P_5/P_1
Air - 7	13.5	6.25
Air - 850	2.14	101
Helium - 850	0.96	85

Once the pressure ratio P_2/P_1 has been determined the Mach number of the incident shock (M_S) can be found using normal shock relations. The Mach number of the reflected shock wave (M_R) is determined with the following equation

$$\frac{M_R}{M_R^2 - 1} = \frac{M_S}{M_S^2 - 1}\sqrt{1 + \frac{2(\gamma_1 - 1)}{(\gamma_1 + 1)^2}\left(M_S^2 - 1\right)\frac{\gamma_1 + 1}{M_S^2}} \tag{A.6}$$

The pressure ratio P_5/P_2 is the found using normal shock relations and the final result P_5/P_1 is then known. For the case of air at an initial pressure ratio of 7:1, the numerical solution was extremely accurate in comparison with the steady state pressure ratio of 6.243. As the pressure ratio increased, the accuracy of the solution decreased, and the steady state solution for air at the higher pressure ratio was $P_5/P_1 = 75.74$ and 50.166 for helium. Comparing these results with those found in Table 1 indicates that there are large errors in the numerical prediction for higher pressure ratios would could be eliminated by increasing the number of nodes and stability criterion.

The second method used to verify the program was the long time numerical solution results which predict the final steady state pressure ratio. The theoretical steady state final pressure ratio was obtained with the conservation of mass equation which can be manipulated into the following form:

$$\frac{P_4}{T_4}\left[\frac{l}{L}\right] + \frac{P_1}{T_1}\left[1 - \frac{l}{L}\right] = \frac{P_F}{T_F} \tag{A.7}$$

where l/L is the percent of driver gas used. Figure A.5 shows the long time numerical solution for air with an initial pressure ratio of 140/1 and $l/L = 0.15$. The equation above predicts a steady state pressure ratio of 14.92, which is indeed the value which the numerical solution approaches.

The two methods used to verify the numerical results indicate that although there can be some rather large instabilities in the reflected pressure ratios at higher operating pressures, the program provides an accurate long term solution. Additionally, for higher operating pressures the results indicate that further increases in pressure and temperature may occur after the reflected expansion waves move through the medium. This phenomena is observed in both Figures A.3 and A.4, and indicates that there may actually be longer test times available with non-uniform properties. The numerical solution of the Riemann problem provides a basic knowledge of the interaction of shock waves and expansion waves.

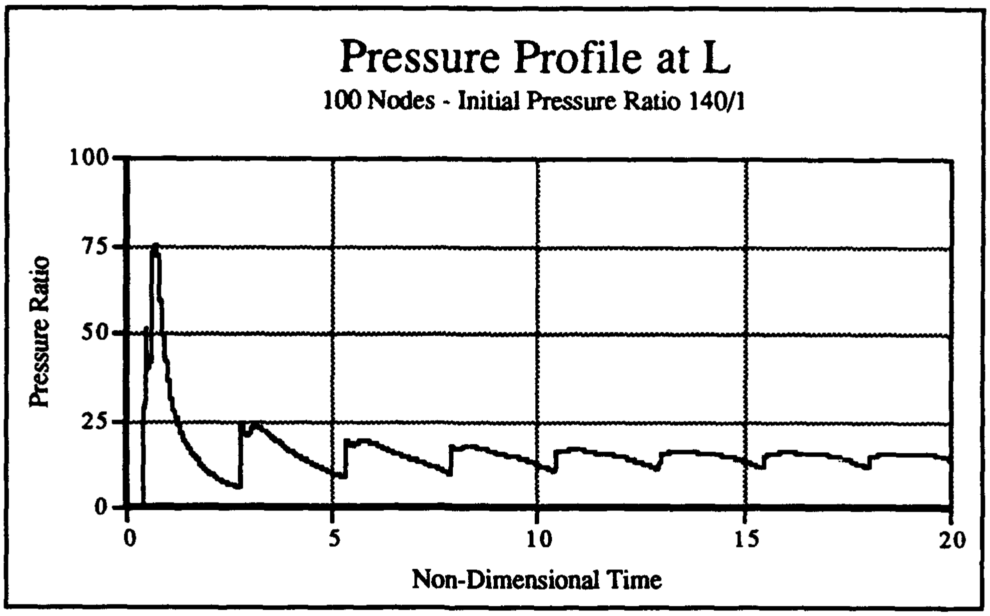

Figure A.5 Long time solution

APPENDIX B - SHOCK TUBE OPERATING PROCEDURE FOR HYDROGEN FLUORIDE EXPERIMENTS

This appendix describes the procedural steps and precautions necessary to operate the shock tube facility. Also listed is the equipment required to safely handle hydrogen fluoride and sodium hydroxide, the neutralizing agent.

B.1 Safety Equipment

Items to be worn when handling Hydrogen Fluoride

1) Neoprene Gloves
2) Latex Gloves underneath Neoprene gloves
3) Neoprene Lab coat with arm protection
4) Goggles, dust resistant and splash resistant
5) Face Shield
6) Gas Mask with Acid cartridges

Items to be worn when handling scrubber solution

1) Neoprene Gloves
2) Latex Gloves underneath Neoprene gloves
3) Neoprene Lab coat with arm protection
4) Lab Apron
5) Goggles, dust resistant and splash resistant
6) Face Shield
7) Rubber Boots
8) Gas Mask

Other safety equipment necessary for laboratory

1) Escape respirators
2) Fume hood
3) Eye wash station
4) Safety shower
5) List of phone numbers
6) Material Safety Data Sheets

B.2 Hydrogen Fluoride Handling and Shock Tube Operating Procedure

BEFORE HF CAN BE ORDERED AND DELIVERED

1) Check for leaks in Shock Tube and all piping. Look at transducer plugs and endwall carefully.
    a) To detect leaks, use Snoop solution, obtainable at the Material Research Laboratory storeroom
    b) Fill shock tube with helium to approximately 500 psig.
    c) Sniff out leaks with Snoop, concentrating on plugs and endwall. Also check out piping.
    d) If possible, obtain a helium leak detector from the Materials Processing Lab in the Engineering Sciences Building, room 140, 3-1710. Recheck any questionable joints.

2) Check Safety Equipment. Make sure emergency respirators have a full air supply and are in working order. Check gloves for leaks and tears in clothing, aprons.
    a) If respirators do not have a full supply, they can be filled and tested at Illini Fire Supplies, 367-9521.
    b) People who use respirators must be trained to operate them by the University Fire Department, Lt. Richard A. Rodgers, 3-2428.

3) Check ventilation system. Check all ducts for operation. Make sure fume hood is operational. Check circuit breaker frequently.

4) Close all valves in entire system. **There are 12 valves in all** (See piping diagram in appendix). Use check list.

5) Display Material Safety Data Sheets outside room as well as emergency phone numbers.

6) Make everyone involved aware of the procedures. Make sure everyone can operate respirators, knows escape routes, location of emergency phone numbers.

7) Prepare scrubber solution
    a) **Neoprene gloves, lab coat, apron, goggles, face shield and gas mask must be worn when preparing solution.**
    b) Fill scrubber with 4.5 gallons of water with polyethylene 5-gallon container. It can be measured with the wooden dowel provided. Place empty container under drain of scrubber.
    c) Check again to see if ventilation system is operational.
    d) Mix in 70 grams of solid Sodium Hydroxide, one spoonful at a time to carefully dissolve the solid. Mix solution with wooden dowel. This will create a 10% solution. Calcium Hydroxide may be interchanged with Sodium Hydroxide because it produces a non toxic organic compound. However, only a 2% solution (20 grams) can be made because of the low solubility of $Ca(OH)_2$ in water.
    e) Check pH level of solution with litmus paper by attaching the litmus paper to the wooden dowel. Record level. The normal level of a 10% solution is a pH of 13 (blue).
    f) Close scrubber securely.
    g) Place remainder of solid NaOH in designated cabinet (along north wall). Make sure warnings are placed on cabinet describing nature of contents.

TWO PEOPLE MUST BE PRESENT TO COMPLETE CHECKLIST FROM THIS POINT

8) HYDROGEN FLUORIDE Procedure. Purchase a lecture bottle from S.J. Smith. A lecture bottle requires a 25 dollar return fee at the time of return.

9) Secure HF bottle in bracket in fume hood. Do not attach valves or piping until ready to run the experiment.

10) Lower fume hood door to lowest position, but not completely closed.

11) Make sure warnings are placed on fume hood describing nature of contents.

12) Prepare for an experiment. Select a target temperature and pressure and oxidizer, calculate initial conditions. Turn on recording equipment. The equipment needs 30 minutes to warm up.
a) Turn on Soltec, transducer power output, and computer.
b) Load up PEAK_UP software.
c) Under SERVICES, select CHANGE DIR and change directory until in C:/PEAK_UP/SHOCKDTA directory.
d) Under TRANSFER, select MENU --> RECORDER, and then select the 5 MHz file.
e) Change directory to C:/PEAK_UP/TESTDAT
f) Under TC CONTROL, select INPUT. Change TB1:RATE to determine the test time. 500 ns gives about a 10 ms time.
g) Select MAIN DELAY to determine the amount of negative time recorded. It is desirable to have 2 ms of negative time so an appropriate value is -25%.
h) Under TC CONTROL, select AMPLIFIER. Set amplifier to desired recording ranges.
i) On the actual recorder, hit the GND button on each channel so that they are grounded. On the fourth channel, hit the AAF so that its light is off.
j) On the power output box, check the output of channels 1, 2, and 3. If they are not in the green, check the actual transducer connection and amplifier.
k) Under TC CONTROL, select CLR to clear and arm the recorder. Select it again so that the message TC WAITING FOR TRIGGER comes up to make sure the recorder is armed.
l) TRG under TC CONTROL will trigger the recorder. Do it once to see if everything is working properly.
m) CLR recorder right before you fire the shock tube.

Steps 13-17 should be completed with gas masks, Neoprene gloves, rubber gloves, goggles, apron, and face mask on. Some tasks are difficult with Neoprene gloves, but wear them whenever possible.

13) Open vent valve [11] and scrubber valve [9] to make sure there is no pressure in shock tube. Close valves when completely vented. Then open ball valve [3] and needle valve [2] to driven section pressure gauge to vent remaining gases. Close valves when completed. Open diaphragm section of shock tube. Dispose of old diaphragms.

14) Remove endwall from shock tube.

15) Remove sidewall transducers and trigger.

16) With Stomper Truck, fishing line, and dry scouring cloth, dry scrub the inside of the shock tube twice. Catch diaphragm particles in plastic bin. When finished with cloth, place it in the designated receptacle.

17) With Stomper Truck, fishing line, wet scrubbing cloth, and a weak solution of NaOH (1%) (provided in spray bottle), wet scrub the inside of the shock tube twice. When finished with cloth, place it in the designated receptacle.

18) Dry shock tube with vacuum cleaner for approximately ten minutes. Steps 19-29 can be completed while vacuum is operating.

Rubber gloves must be worn when handling and cleaning equipment, steps 19-29. Gas mask, goggles, and face mask may be removed. Double check the gloves for leaks.

19) Wipe down end of sidewall transducers and trigger with weak NaOH solution. Dry off with cloth.

20) Replace protective tape over transducers.

21) Inspect transducer plug gaskets for any deterioration, three gaskets per plug. Replace if necessary.

22) Replace sidewall transducers to shock tube.

23) Test trigger with voltmeter. Should read approximately 7 volts. Fix if necessary.

24) Inspect trigger plug gasket. Replace if necessary.

25) Replace trigger in shock tube.

26) Clean endwall with weak solution of NaOH, removing large particles, being careful not to scratch window.

27) With degreaser, remove small particles from endwall. If necessary, use scouring pad on the steel section and a razor blade on the window.

28) Inspect endwall for corrosion damage - window and gaskets. Replace if necessary.

29) Dry endwall with Kimwipe, including the gap between the window and the steel section.

30) Check and realign optics.
    a) Cover endwall window with filter.
    b) Place light bulb approximately 6 inches within the shock tube. Have cord come through the top port of shock tube.
    c) Install endwall in shock tube.
    d) Move shock tube back so shoulder bolts align with back end of tape which is located on the lens holder's base.
    e) Plug in light.
    f) Align mirror and lens so that light is focused on center of photo diode. When photo diode is connected to voltmeter, attempt to get maximum voltage, which is approximately 40 mV.
    g) Unplug light bulb. Move shock tube so that shoulder bolts align with the from end of the tape. Remove endwall. Remove light bulb.

31) Inspect sidewall plug gasket. Replace if necessary. Install plug to shock tube.

32) Dry off condensation from endwall with Kimwipe.

33) Place boron particles on clean knife blade. Install on endwall.

34) Install endwall on shock tube.

35) Install proper number of diaphragms in diaphragm section. **Must hold a minimum of 100 psig.**

36) Close diaphragm-driven section securely. Open diaphragm-driver section. Install diaphragms. Close section securely.

37) Check pH level of scrubber solution. **Gloves, lab coat, apron, face mask, goggles and gas mask must be worn for this step.** Tack a strip of litmus paper to end of wooden dowel. Dip in scrubber. If solution is neutralized (pH below 9, green/yellow litmus paper), add more sodium hydroxide to solution. Be aware of how much solution is available. A pH of 13 is recommended.

38) Open the scrubber needle valve [9] to the setting appropriate for the initial driver pressure.

Protective clothing may be removed for steps 39-59.

39) Open Helium, Oxygen, and Nitrogen bottles. Check regulators to see if adequate pressure is available to run experiment.

a) Helium should have approximately twice the pressure available than the experiment's initial driver pressure. Also the needle valve after the helium regulator should be opened slightly, depending on how much helium remains in the bottle, so as not to have a pressure jump in the shock tube during the loading procedure.

b) Oxygen should have over 100 psig available and regulator delivery pressure should be set to above 60 psig.

c) Nitrogen should have over 750 psig available and regulator delivery pressure should be set to 120 psig.

40) Open Nitrogen needle valve [1] to driven section.

41) Open needle valve [6] from shock tube to oxygen line and open ball valve [3] to the driven section pressure gauge.

42) Fill driven section with nitrogen by way of the solenoid switch in the control room. This will serve as a leak checker as well as a moisture purge. Close solenoid when 100 psig is reached.

43) With Snoop, check for leaks around plugs (6), endwall, and diaphragms. Also periodically check Hydrogen Fluoride needle valve [7] as well as any other valves that will be under pressure (every 5-10 shots). If leak is present, vent off driven section from the needle valve [2] located underneath the driven section pressure gauge. Fix leak. Repeat 39-41.

44) Vent off Nitrogen through the needle valve [2] located underneath the driven section pressure gauge. Close valves [2,3] around the pressure gauge when completed.

45) Turn on vacuum pump. Open needle valve [4] and ball valve [5] to vacuum pump.

46) Evacuate tube to below 95 kPa below atmospheric. This is read from the vacuum gauge in control room.

47) Close needle valve [6] from shock tube to oxygen line.

48) Evacuate piping down until minimum vacuum is reached. Record vacuum measurement.

49) Open needle valve [6] from shock tube to oxygen line.

50) Close ball valve [5] and needle valve [4] to vacuum pump. Turn off vacuum.

51) Fill driven section with oxygen from control room for approximately two minutes.

52) Open ball valve [3] to driven section pressure gauge.

53) Fill driven section with oxygen to approximately 50 psig.

54) Vent off driven section through driven section pressure gauge needle valve [2].

55) When 10 psig is reached, close both valves [2,3] and turn on vacuum pump and open the needle valve [4] and ball valve [5].

56) Evacuate tube to desired partial pressure of oxygen.

57) Turn off vacuum pump and needle [4] and ball valves [5].

58) Check and record temperature.

HYDROGEN FLUORIDE LOADING

59) Double check ventilation system.

60) Place yellow personnel caution tape outside of door. Close outside door, but DO NOT LOCK or have someone remain outside of door.

61) With **gas mask, gloves, goggles and face shield**, open fume hood door.

62) Plumb Hydrogen Fluoride bottle with lecture bottle valve [8], if not already done.

63) Open lecture bottle and lecture bottle valve [8].

64) Lower fume hood door to lowest position.

65) Open needle valve [7] to HF line from shock tube.

66) From control room, quickly open and close HF solenoid until desired driven pressure is reached.

67) **With gas mask, gloves, goggles and face mask on, exit control room and close HF needle valve [7] to tube, needle valve [6] from shock tube to oxygen line, lecture bottle valve [8] and lecture bottle. Lower fume hood door.** After completed, **everyone should be in the control room and should not leave until step 78. Protective equipment may be removed but kept in control room.**

68) Make sure that the firing valve [10] and vent valve [11] are closed.

69) Open diaphragm solenoid.

70) Open helium solenoid; this will start the filling process of the driver section.

71) When the diaphragm section has reached half of the desired driver section pressure, turn off diaphragm solenoid.

72) When driver section has reached its desired pressure, turn off helium solenoid.

73) Check data acquisition system. Make sure appropriate settings are set and recorder is armed by selecting CLR. Clear recorder a few times to make sure that it has not prematurely fired.

74) **Fire the shock tube by flipping the fire switch up.**

75) After the tube has fired, flip the vent switch up to vent the shock tube. **This is the time when the room is most susceptible to HF leaks.** Visually observe the shock tube for any white fumes escaping, which would signify the HF reacting with the moisture in the room.

76) While it is venting, load up the data onto the computer form under the TRANSFER directory, the DATA --> WINDOW command.

77) When the driver gauge reads 100 psig, turn on the Nitrogen solenoid to flush the system.

78) Leave Nitrogen solenoid open for 5 minutes, then shut off.

79) Let tube vent down for another 5 minutes.

80) **With gas mask and gloves on**, go out to scrubber and open valve [9] to scrubber to the 400 psi setting.

81) Open the needle valve [6] from the shock tube to the oxygen line and the needle valve [7] from the shock tube to the HF line.

82) From control room, close fire [10] and vent valves [11].

83) Fill tube with Nitrogen for another 5 minutes or until 100 psig is reached.

84) Open vent valve [11].

85) After another 5 minutes close Nitrogen solenoid.

86) Let tube evacuate to zero gauge pressure.

87) If doing another shot, go to step 12.

IF LAST SHOT OF DAY

88) Turn on vacuum pump and ball [5] and needle valves [4] and evacuate shock tube completely. Turn off pump. Close valves [4,5].

89) **With gas mask, gloves, goggles and face shield,** open lecture bottle valve [8] and needle valve [7] from HF line to tube. Open HF solenoid.

90) Open vent valve [11].

91) Close Helium and Oxygen bottles, but not the Nitrogen bottle.

92) Open Helium, Diaphragm, and Oxygen solenoids until lines are evacuated (approximately 1 minute; it can be heard).

93) With HF solenoid open, turn on Nitrogen solenoid and fill until tube has reached positive pressure. Turn off HF solenoid.

94) Leave Nitrogen solenoid open for 5 minutes. Turn off solenoid.

95) If next shot will be over 24 hours away, let shock tube vent down to atmospheric pressure and then breakdown and clean tube as in steps 13-29.
If next shot is next day, let shock tube vent down to 10 psig and the close vent valve [11]. Shock tube must remain under pressure if not used.

IF FINISHED WITH HYDROGEN FLUORIDE

96) After venting is complete, close HF lecture bottle valve.

97) **With fume hood halfway open, and with gloves and gas mask on,** remove lecture bottle valve from lecture bottle.

98) Leave lecture bottle in fume hood until the proper personnel (bottle supplier) can remove it safely.

IF FINISHED WITH SCRUBBER

99) **With goggles, face shield, gas mask, gloves, lab coat, and apron**, check the pH level of solution with litmus paper.

100) If pH level is above 9 (green paper), neutralize solution with dilute amounts of citric acid, located in storage cabinet.

101) If pH level is below 5 (orange paper), slowly add more sodium hydroxide.

102) Once solution has a pH level between 5 and 9, the liquid solution can then be drained through ball valve [12] into the 5 gallon polyethylene jug. This solution can then be safely poured down the drain. While pouring the solution, keep the faucet running to dilute the solution even further.

103) After the scrubber has drained, remove drain cap from scrubber. There should be some salt residue on the cap and possibly within the scrubber as well.

104) The residue may be washed down the sink as well, but only in small amounts. If there is large amounts of residue, contact Hazardous Waste Management, 244-9278.

105) After drain cap has been cleaned, replace cap and fill scrubber with water. Drain scrubber to remove any residual chemicals.

If bottle of HF springs a leak:

a) If in the control room, **put on emergency escape respirators**. If in main room, do not go back into the control room.
b) If next to fume hood when leak starts, safely attempt to close fume hood. If not possible, do not attempt.
c) Leave room.
d) Get list of emergency phone numbers which wall outside of room and go to room 6, which is in the building, downstairs.
e) Call fire department, gas bottle supplier, and then other people on list.
f) After HF clears, disconnect bottle from lines.
g) Purge all lines with Nitrogen.
h) Have supplier remove the bottle.

If there is a leak with the system:

a) If it is a continuous leak where the HF bottle is open to the leak, repeat procedure as if the bottle has sprung a leak.
b) If leak is within the lines but not directly connected to the bottle, remain in the control room, open the vent solenoid, and purge the system with Nitrogen for 20 minutes.
c) Once completely discharged, fix line.

If there is a spill of Sodium Hydroxide

a) Wear gas mask, gown, boots, goggles, face mask, and gloves before attempting to neutralize solution.
b) Dilute spill with water. If solution has high pH level, use a dilute citric acid to neutralize solution.

If either HF or scrubber solution get in contact with skin, eyes, or is inhaled, refer to the MSDS for the material in question, which is appended to the procedure.

Valve Checklist

1) Nitrogen Needle Valve ____ ____ ____ ____ ____ ____
2) Driven Section Gauge Exit Ball Valve ____ ____ ____ ____ ____ ____
3) Driven Section Gauge Entrance Ball Valve ____ ____ ____ ____ ____ ____
4) Vacuum Pump Needle Valve ____ ____ ____ ____ ____ ____
5) Vacuum Pump Ball Valve ____ ____ ____ ____ ____ ____
6) Oxygen Needle Valve ____ ____ ____ ____ ____ ____
7) Hydrogen Fluoride Needle Valve ____ ____ ____ ____ ____ ____
8) Hydrogen Fluoride Lecture Bottle Valve ____ ____ ____ ____ ____ ____
9) Scrubber Needle Valve ____ ____ ____ ____ ____ ____
10) Fire (Diaphragm) Electric Ball Valve ____ ____ ____ ____ ____ ____
11) Vent (Driver) Electric Ball Valve ____ ____ ____ ____ ____ ____
12) Scrubber Drain ____ ____ ____ ____ ____ ____

APPENDIX C - SHOCK TUBE DATA

This appendix tabulates the data recorded for the amorphous and crystalline boron shock tube research. The header blocks before each set of data describe the type of boron used, the type of oxidizer used, and the target reflected pressure.

For the amorphous data (Table C.1), the columns are, from left to right, the shot number, oxidizing mixture, incident shock wave Mach number, reflected pressure, initial temperature, incident temperature, reflected temperature, the peak voltage of the photodiode signal, the ignition delay time, and the burn time.

The crystalline boron data (Table C.2) columns are the shot number, oxidizing mixture, incident shock wave Mach number, reflected pressure, initial temperature, incident temperature, reflected temperature, the peak voltage of the third peak of the photodiode signal, the ignition delay of peak 1, the ignition delay of peak 2, the burn time of peaks 1 and 2 combined, the ignition delay of peak 3, the burn time of peak 3, the ignition delay of peak 4, the burn time of peak 4, and whether or not the third peak signal can be considered ignition. Chapter 4 describes the conditions for determining ignition.

The x's in the tables represent data that could not be recorded.

Table C.1 Amorphous boron data

	Shot Number	Oxidizer Mole Fraction	Mach Number	P5 [psia]	T1 [K]	T2 [K]	T5 [K]	Voltage Peak [mV]	Ignition Delay [μs]	Burn time [μs]
Amorphous Boron **<1 micron** **100% O2** **125 psia**	6	1	4.18	114.33	295.1	1172.0	2101.0	3000+	x	x
	7	1	4.22	116.83	298.6	1199.0	2152.0	6000+	13.8	?
	8	1	4.64	103.61	300.0	1382.2	2488.9	3184	14.0	41.6
	9	1	5.14	133.59	296.0	1592.8	2814.0	1680	15.0	25.4
	10	1	4.08	127.71	298.2	1143.0	2040.9	7088	14.4	32.4
	11	1	3.76	150.78	299.5	1025.8	1800.6	3216	23.0	21.0
	12	1	3.88	147.84	300.2	1070.6	1891.8	1648	18.6	33.4
	13	1	3.70	153.87	302.2	1010.4	1766.3	2168	21.0	16.0
	14	1	3.48	139.47	298.2	920.6	1585.2	344	29.8	25.8
	15	1	4.19	151.37	298.4	1188.0	2130.7	4688	14.4	31.6
	16	1	3.27	146.96	295.3	842.4	1426.7	0	∞	∞
	17	1	3.45	155.19	296.0	903.6	1552.2	848	37.6	27.8
	18	1	3.47	155.48	297.0	912.5	1569.6	568	34.4	28.4
	19	1	3.35	148.58	296.7	872.1	1486.6	1884	33.0	26.0
Amorphous Boron **<1 micron** **100% O2** **250 psia**	20	1	4.10	263.65	293.6	1132.1	2023.7	4304	14.4	23.6
	21	1	3.45	254.83	295.3	902.0	1549.7	472	31.2	27.0
	22	1	5.12	272.90	296.5	1585.7	2835.0	8020	10.6	32.6
Amorphous Boron **<1 micron** **60% H2O/40% Ar** **125 psia**	24	.5900/.4100	4.17	108.60	295.1	1225.4	2112.9	232	18.0	27.6
	25	.5900/.4100	4.21	111.25	294.1	1237.5	2133.5	1940+	14.6	27.6
	26	.5700/.4300	5.12	110.66	295.4	1663.7	2687.3	3660	-5.0	25.8
	27	.5900/.4100	4.56	110.81	296.0	1391.8	2363.0	1380	1.0	29.4
Noise Shot **0 micron** **60% H2O/40% Ar** **125 psia**	28	.5600/.4400	4.21	108.75	294.3	1257.4	2171.8	38	x	x
Amorphous Boron **<1 micron** **97% O2/3% SF6** **125 psia**	29	.9790/.0210	3.86	158.86	297.4	1003.9	1573.0	240	19.0	21.0
	30	.9630/.0370	4.49	157.69	297.8	1177.0	1694.9	2892	6.8	23.2
	31	.9710/.0290	3.60	153.57	298.1	899.4	1454.7	24	35.0	18.0

Table C.2 Crystalline boron data

	Shot Number	Oxidizer Mole Fraction	Mach Number	P5 [psia]	T1 [K]	T2 [K]	T5 [K]	Voltage Peak 3 [mV]	Ignition Delay 1 [µs]	Ignition Delay 2 [µs]	Burn time 1-2 [µs]	Ignition Delay 3 [µs]	Burn time 3 [µs]	Ignition Delay 4 [µs]	Burn time 4 [µs]	Ignition ?
Crystalline Boron 20-25 micron 100% O2 125 psia	48	1	5.211	118.32	294.2	1617.7	2841.3	340	18.4	53.0	88.0	181.6	565.0	978.6	874.0	yes
	49	1	4.782	107.10	294.9	1423.6	2561.0	52	27.4	0.0	67.0	827.6	251.0	x	x	yes
	50	1	4.568	122.50	293.5	1324.6	2395.2	20	18.4	67.4	31.0	579.2	423.4	x	x	no
	51	1	4.302	120.94	293.4	1213.6	2185.2	34	23.0	74.0	61.0	647.4	194.8	3010.0	380.0	no
	52	1	5.610	110.01	293.6	1809.2	3043.0	492	16.8	49.8	110.6	216.6	221.2	1011.8	619.0	yes
	54	1	4.522	119.37	293.4	1304.7	2358.6	12	18.0	54.0	31.0	646.0	193.0	x	x	no
	55	1	4.537	108.78	293.5	1311.4	2370.0	44	14.0	58.0	87.0	562.6	218.6	2417.0	275.0	no
	56	1	4.678	117.62	293.1	1370.3	2475.9	36	16.2	58.2	31.4	754.4	146.0	x	x	no
	57	1	4.949	114.59	293.2	1491.2	2669.3	164	18.2	54.6	82.4	256.8	208.2	569.6	785.4	yes
	58	1	4.747	112.54	289.0	1382.9	2500.1	52	14.0	56.0	66.0	302.4	267.4	1190.4	117.6	yes
	93	1	5.342	125.76	298.6	1702.5	2941.9	174	16.4	49.2	91.2	221.4	390.0	896.2	209.4	yes
	106	1	4.603	112.94	297.2	1354.6	2444.7	22	23.0	60.0	65.0	530.4	750.8	x	x	no
	106A	1	4.808	126.08	296.4	1441.7	2593.5	58	17.0	57.6	64.6	563.8	453.0	1401.8	644.0	yes
	107	1	3.938	115.28	296.9	1082.8	1919.6	14	27.6	66.2	76.2	761.4	117.0	x	x	no
	109	1	4.819	116.99	292.7	1430.5	2576.6	60	18.0	30.0	50.0	718.0	320.0	x	x	yes
	110	1	5.501	117.18	293.1	1752.6	2992.6	190	18.0	50.0	58.0	258.0	1566.0	x	x	yes
	111	1	5.440	120.59	294.3	1728.8	2969.5	540	18.0	52.0	84.0	310.0	302.0	768.0	188.0	yes
	112	1	2.871	171.03	295.8	719.8	1173.1	x	x	x	x	x	x	x	x	no
	113	1	5.203	108.22	290.2	1594.4	2810.0	76	16.0	50.0	58.0	254.0	490.0	792.0	680.0	yes
	114	1	3.977	146.60	290.5	1076.5	1913.2	-4	x	x	x	x	x	x	x	no
	128	1	4.866	118.83	297.4	1472.8	2639.4	76	23.0	49.0	42.0	364.0	365.0	1370.0	54.0	yes
	129	1	4.964	118.89	298.6	1522.2	2712.3	124	21.0	53.0	110.0	344.0	304.0	875.0	1998.0	yes
	129A	1	4.913	115.76	294.0	1478.4	2650.0	116	19.0	59.0	49.0	367.0	802.0	6139.0	897.0	yes
	129B	1	4.918	116.04	293.4	1478.0	2649.9	92	18.0	57.0	67.0	260.0	616.0	4043.0	907.0	yes
	129C	1	4.929	116.68	293.2	1482.1	2656.3	92	19.0	58.0	62.0	410.0	439.0	1306.0	1783.0	yes
	129D	1	4.955	118.22	293.7	1496.2	2677.3	140	17.0	50.0	95.0	459.0	417.0	2131.0	646.0	yes
	130	1	5.413	120.29	294.6	1717.2	2956.7	292	18.0	49.0	109.0	134.0	274.0	440.0	365.0	yes
	130A	1	5.460	122.80	293.6	1734.0	2976.6	412	20.0	48.0	107.0	134.0	327.0	675.0	170.0	yes
	134A	1	4.993	120.60	299.9	1541.9	2739.5	86	26.0	56.5	99.5	275.0	937.5	1704.0	2578.0	yes
Crystalline Boron 32-38 micron 100% O2 125 psia	59	1	4.766	113.69	289.0	1391.2	2514.2	28	15.0	59.0	62.0	1265.4	283.4	x	x	no
	91	1	4.765	117.66	298.2	1430.2	2572.1	12	24.0	x	26.0	732.6	143.8	x	x	no
	91A	1	4.694	113.25	297.9	1397.6	2517.7	36	27.0	x	45.0	633.6	232.6	1310.8	104.6	yes
	91B	1	4.738	115.96	298.0	1417.4	2551.1	20	x	x	x	670.8	97.0	2302.0	217.0	no
	92	1	5.301	123.40	298.3	1681.3	2916.8	78	17.0	58.0	58.4	255.0	1174.0	2688.2	469.0	yes
	92A	1	5.265	121.39	298.3	1663.7	2895.8	78	13.0	53.0	63.8	179.0	913.8	x	x	yes

Table C.2 Crystalline boron data (continued)

	Shot Number	Oxidizer Mole Fraction	Mach Numbe	P5 [psia]	T1 [K]	T2 [K]	T5 [K]	Voltage Peak 3 [mV]	Ignition Delay 1 [µs]	Ignition Delay 2 [µs]	Burn time 1-2 [µs]	Ignition Delay 3 [µs]	Burn time 3 [µs]	Ignition Delay 4 [µs]	Burn time 4 [µs]	Ignition ?
Crystalline Boron **20-25 micron** **100% O2** **250 psia**	60	1	4.785	233.74	289.3	1400.8	2542.2	132	18.8	65.8	59.0	276.2	287.4	1015.0	319.0	yes
	61	1	4.495	228.40	286.6	1266.5	2296.0	x	17.2	59.2	43.0	x	x	x	x	no
Crystalline Boron **20-25 micron** **100% O2** **500 psia**	66	1	5.262	486.87	299.0	1665.3	2970.3	1108	13.4	162.4	120.6	162.8	536.2	917.0	1074.0	yes
	67	1	5.338	503.92	298.3	1699.5	3018.3	2510	24.4	134.8	183.8	212.2	435.2	780.4	920.0	yes
	68	1	4.947	545.83	298.9	1515.5	2746.1	760	21.4	53.2	58.8	168.0	722.2	924.2	1169.0	yes
	69	1	4.985	496.23	298.4	1531.2	2769.6	654	23.4	53.8	43.8	179.6	582.6	787.2	939.0	yes
	70	1	5.071	479.72	298.0	1570.0	2830.0	1032	14.4	54.0	68.0	167.0	603.4	850.4	1013.0	yes
	71	1	4.813	479.67	298.2	1451.7	2635.0	258	19.2	58.2	55.6	274.2	994.8	1702.0	547.0	yes
	73	1	4.098	450.90	298.5	1149.9	2055.8	78	26.4	68.4	76.6	640.0	288.0	1146.0	123.0	yes
	108	1	5.589	492.08	297.2	1348.6	2448.2	90	15.2	x	30.4	149.0	405.8	1432.4	327.0	yes
Crystalline Boron **32-38 micron** **100% O2** **250 psia**	75	1	5.455	238.49	298.0	1755.8	3043.7	952	27.8	88.4	130.2	172.4	292.0	642.2	766.2	yes
Crystalline Boron **<20 micron** **100% O2** **250 psia**	76	1	5.431	236.00	298.2	1744.8	3030.4	x	33.2	484.4	549.6	x	x	x	x	yes
	77	1	5.281	244.93	298.2	1671.1	2944.0	2184	18.2	49.4	65.6	529.6	465.2	x	x	yes
	78	1	4.976	241.36	298.3	1526.7	2742.3	410	10.2	50.6	98.0	578.8	311.0	1504.2	735.8	yes
	85	1	4.848	240.00	298.3	1467.9	2649.4	330	16.0	55.4	70.6	176.8	373.4	1468.4	317.0	yes
	86	1	4.821	236.61	298.1	1455.0	2627.7	230	23.0	56.8	46.2	434.6	297.0	1105.0	767.6	yes
Crystalline Boron **25-32 micron** **100% O2** **125 psia**	87	1	5.351	129.89	298.1	1704.8	2946.5	186	21.4	50.0	77.0	224.2	992.2	x	x	yes
	88	1	5.232	119.53	298.1	1647.0	2875.1	102	29.0	52.0	50.8	264.6	855.6	x	x	yes
	89	1	5.312	124.00	298.1	1685.8	2922.2	150	31.6	x	95.2	196.0	439.6	x	x	yes
	90	1	4.738	115.97	298.1	1417.8	2551.6	x	19.0	57.0	81.4	x	x	x	x	no
	90A	1	4.738	115.97	298.1	1417.8	2551.6	28	18.0	60.0	61.0	698.4	122.2	1374.0	507.4	no
	90B	1	4.738	115.97	298.1	1417.8	2551.6	76	20.0	59.0	62.4	797.8	97.0	1351.6	269.6	yes

Table C.2 Crystalline boron data (continued)

	Shot Number	Oxidizer Mole Fraction	Mach Number	P5 [psia]	T1 [K]	T2 [K]	T5 [K]	Voltage Peak 3 [mV]	Ignition Delay 1 [µs]	Ignition Delay 2 [µs]	Burn time 1-2 [µs]	Ignition Delay 3 [µs]	Burn time 3 [µs]	Ignition Delay 4 [µs]	Burn time 4 [µs]	Ignition ?
Crystalline Boron 20-25 micron 30% H2O 70% O2 125 psia	115	.423/.577	5.003	79.72	294.7	1421.7	2413.4	70	20.0	x	56.0	254.0	230.0	x	x	no
	116	.200/.800	5.519	116.35	295.1	1703.4	2810.5	570	14.0	50.0	86.0	216.0	170.0	3464.0	256.0	yes
	117	.329/.671	5.184	121.62	292.4	1501.4	2544.1	180	18.0	52.0	52.0	212.0	966.0	1416.0	822.0	yes
	118	.300/.700	4.770	117.58	293.6	1347.7	2334.0	12	18.0	54.0	46.0	718.0	234.0	8078.0	254.0	no
	119	.275/.725	4.462	110.97	294.2	1232.1	2148.0	4	34.0	66.0	35.0	1038.0	34.0	9608.0	702.0	no
	122	.300/.700	5.131	134.81	291.2	1487.3	2539.9	138	18.0	x	48.0	448.0	558.0	1408.0	2476.0	yes
	123	.300/.700	5.174	123.98	293.4	1515.3	2572.8	66	24.0	x	64.0	388.0	390.0	x	x	yes
	124	.300/.700	5.420	124.63	294.6	1630.2	2711.1	282	10.0	46.0	84.0	298.0	500.0	x	x	yes
	125	.300/.700	5.276	108.56	265.7	1569.6	2634.1	786	8.0	36.0	107.0	236.0	153.0	1577.0	260.0	yes
	126	.283/.717	4.717	125.16	298.0	1347.1	2333.9	42	26.0	58.0	70.0	654.0	482.0	2632.0	664.0	yes
	127	.298/.702	4.592	119.45	299.7	1300.0	2254.3	30	20.0	x	98.0	484.0	706.0	1938.0	236.0	yes
Crystalline Boron 20-25 micron 1% SF6 99% O2 125 psia	94	.9907/.0093	4.746	121.67	297.2	1325.8	2181.1	44	22.8	x	61.2	558.6	292.4	1820.0	319.0	yes
	94A	.9906/.0094	4.775	124.01	297.3	1334.0	2200.4	44	18.0	x	50.0	795.2	185.0	1656.0	458.8	no
	94B	.9899/.0101	4.499	103.57	297.5	1249.6	2008.5	36	34.0	x	45.0	542.2	294.0	1901.6	348.4	yes
	95	.9900/.0100	5.014	135.80	298.0	1396.5	2384.3	20	21.0	x	31.0	397.6	117.8	x	x	no
	95A	.9900/.0100	5.056	139.43	297.8	1406.9	2420.2	108	21.0	x	28.0	562.2	426.6	1568.6	773.4	yes
	95B	.9900/.0100	4.959	130.93	297.5	1381.2	2332.0	36	21.0	x	32.0	323.4	783.0	x	x	yes
	96	.9910/.0090	5.363	138.25	297.3	1494.2	2708.5	148	14.0	x	52.8	204.6	538.0	776.6	214.6	yes
	96A	.9910/.0090	5.285	132.66	297.3	1468.4	2648.2	140	10.0	x	27.8	448.0	466.0	x	x	yes
	97	.9880/.0120	5.841	130.97	297.7	1645.4	2937.5	450	16.0	55.0	58.0	390.0	286.0	x	x	yes
	98	.9900/.0100	5.169	136.85	298.0	1433.8	2520.7	82	22.0	x	56.0	240.2	513.0	x	x	yes
	98A	.9900/.0100	5.128	140.83	297.3	1447.7	2557.1	122	18.0	63.0	67.2	297.2	352.8	x	x	yes
	99	.9901/.0099	4.757	118.86	298.2	1328.9	2175.2	74	19.0	x	53.0	258.4	364.0	1296.0	367.6	yes
	99A	.9900/.0100	4.847	125.89	297.2	1351.0	2234.6	110	19.0	66.0	62.0	355.6	308.4	x	x	yes
	100	.9900/.0100	4.559	111.91	298.1	1270.7	2048.2	50	25.0	x	59.0	454.6	439.4	x	x	yes
	100A	.9900/.0100	4.413	102.53	296.2	1218.0	1957.3	42	27.4	x	33.6	634.2	273.0	x	x	yes
	104	.9900/.0100	4.128	115.41	296.6	1121.2	1768.7	14	27.0	x	54.0	565.0	71.0	x	x	no
	104A	.9900/.0100	4.339	130.75	296.9	1197.0	1923.8	26	20.8	x	47.0	546.8	353.0	x	x	yes
	104B	.9900/.0100	4.273	125.20	297.0	1174.2	1879.4	18	25.0	x	52.0	727.0	653.8	x	x	no
	105	.9900/.0100	4.494	120.60	296.7	1248.2	2011.3	30	28.0	x	37.0	366.0	408.0	x	x	yes
	131	.9901/.0099	5.613	127.13	297.5	1583.8	2849.7	78	21.6	x	18.0	373.6	239.6	x	x	yes
Crystalline Boron 20-25 micron 2% SF6 98% O2 125 psia	101	.9800/.0200	5.016	123.55	296.2	1359.2	2106.4	94	x	x	x	x	x	x	x	yes
	102	.9801/.0199	5.581	120.30	296.7	1466.9	2480.2	238	7.0	x	24.8	403.8	643.2	3066.0	251.0	yes
	132	.9801/.0199	6.062	125.66	297.2	1575.6	2867.3	250	19.0	x	44.5	265.5	384.0	1330.0	137.0	yes
	133	.9800/.0200	6.056	116.06	303.7	1601.1	2902.4	738	16.0	x	57.0	299.5	199.5	x	x	yes

Table C.2 Crystalline boron data (continued)

	Shot Number	Oxidizer Mole Fraction	Mach Number	P5 [psia]	T1 [K]	T2 [K]	T5 [K]	Voltage Peak 3 [mV]	Ignition Delay 1 [μs]	Ignition Delay 2 [μs]	Burn time 1-2 [μs]	Ignition Delay 3 [μs]	Burn time 3 [μs]	Ignition Delay 4 [μs]	Burn time 4 [μs]	Ignition ?
Crystalline Boron 20-25 micron 6% HF 94% O2 125 psia	135A	.9512/.0488	4.983	125.47	301.0	1548.1	2732.8	130	20.0	53.0	79.5	144.0	347.5	616.0	529.0	yes
	136	.9487/.0513	4.921	115.69	301.6	1522.1	2693.7	90	20.0	49.0	68.0	329.0	416.0	x	x	yes
	137	.9333/.0667	5.670	125.07	299.6	1881.7	3088.7	460	18.0	52.0	65.5	212.0	413.5	706.0	353.0	yes
	138	.9394/.0606	5.409	123.01	298.5	1743.1	2959.3	102	19.0	51.5	91.0	263.0	597.0	1402.5	1187.5	yes
	139	.9444/.0556	5.204	122.36	302.7	1663.0	2871.4	222	16.0	53.5	57.5	435.0	385.0	851.0	1551.0	yes
	141	.9444/.0556	3.614	95.14	304.1	987.8	1719.4	2	x	x	x	x	x	x	x	no
	142	.9400/.0600	4.195	98.68	302.2	1207.0	2161.4	22	29.0	x	40.0	645.5	702.0	2772.5	294.0	no
	143	.9397/.0603	4.347	125.66	303.2	1274.0	2288.8	x	18.5	x	57.0	x	x	x	x	no
	144	.9400/.0600	4.589	124.50	303.5	1380.1	2476.3	82	16.0	x	51.5	144.5	829.0	2041.5	175.0	yes
	147	.9434/.0566	4.561	129.89	300.1	1353.7	2434.9	42	22.5	x	30.0	2493.5	324.0	x	x	no
Crystalline Boron 20-25 micron 12% HF 88% O2 125 psia	145	.8800/.1200	4.722	132.99	301.4	1437.4	2567.8	30	17.0	x	56.0	315.0	1278.5	2522.5	569.5	no
	146	.8667/.1333	5.615	121.37	302.7	1880.0	3074.2	172	20.0	50.0	73.5	190.0	326.0	516.0	116.5	yes
Crystalline Boron 20-25 micron 6% HF 94% O2 250 psia	148	.9403/.0597	5.653	278.43	300.5	1877.5	3152.6	850	21.5	50.5	59.0	180.5	397.5	634.0	1092.0	yes
Crystalline Boron 20-25 micron 12% HF 88% O2 250 psia	149	.8806/.1194	5.530	262.41	301.1	1826.5	3086.7	686	18.0	49.0	116.0	206.5	490.0	2271.0	4131.0	yes
Noise Shots 0 micron	53	1	4.498	117.75	293.5	1295.0	2340.4	12.4	x	x	x	808.4	949.0	x	x	no
	72	1	4.197	480.23	298.2	1188.6	2133.9	108	x	x	x	865.4	220.0	x	x	no
	74	1	5.646	111.78	298.1	1864.1	3082.0	220	x	x	x	364.0	475.0	x	x	no
	103	.9903/.0097	4.905	115.49	296.7	1363.5	2290.1	18	x	x	x	78.0	662.0	1737.2	293.4	no
	140	.9487/.0513	4.956	117.76	303.4	1546.6	2726.6	42	x	x	x	431.0	443.0	1194.0	232.0	no

APPENDIX D - PHOTODIODE SIGNALS

Depicted in this appendix are selected photodiode signals recorded for boron ignition and combustion in a shock tube. The shot number is referenced to the data tabulated in Appendix C. Not all signals are plotted on the same time or voltage scale so direct comparison might not be possible. Also, not all photodiode signals are displayed in this appendix. The remainder of the signals can be found on disk and in notebooks located in the Shock Tube and High Pressure Combustion Laboratory.

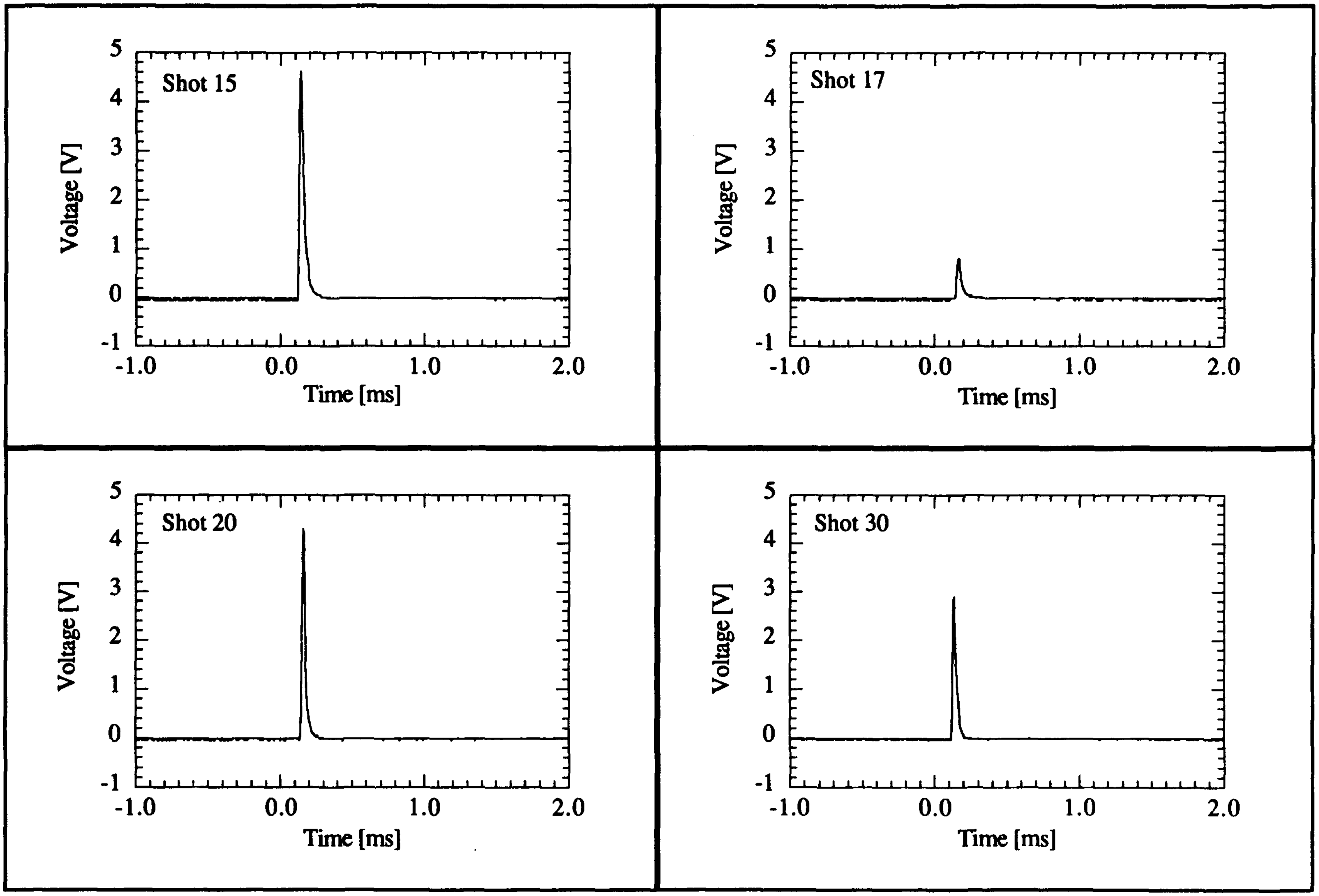

Figure D.1 Amorphous boron photodiode signals.

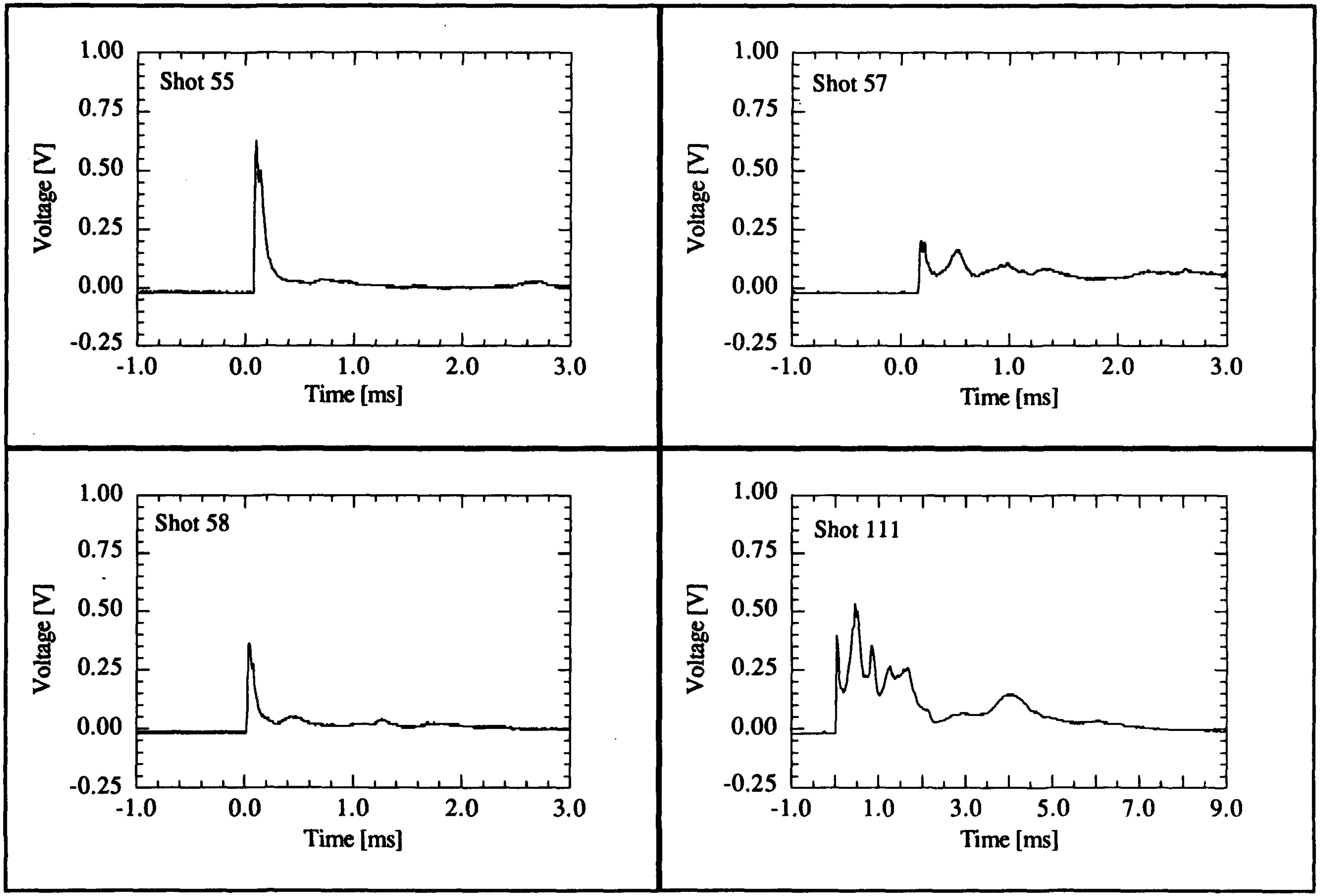

Figure D.2 Nominal condition crystalline boron photodiode signals.

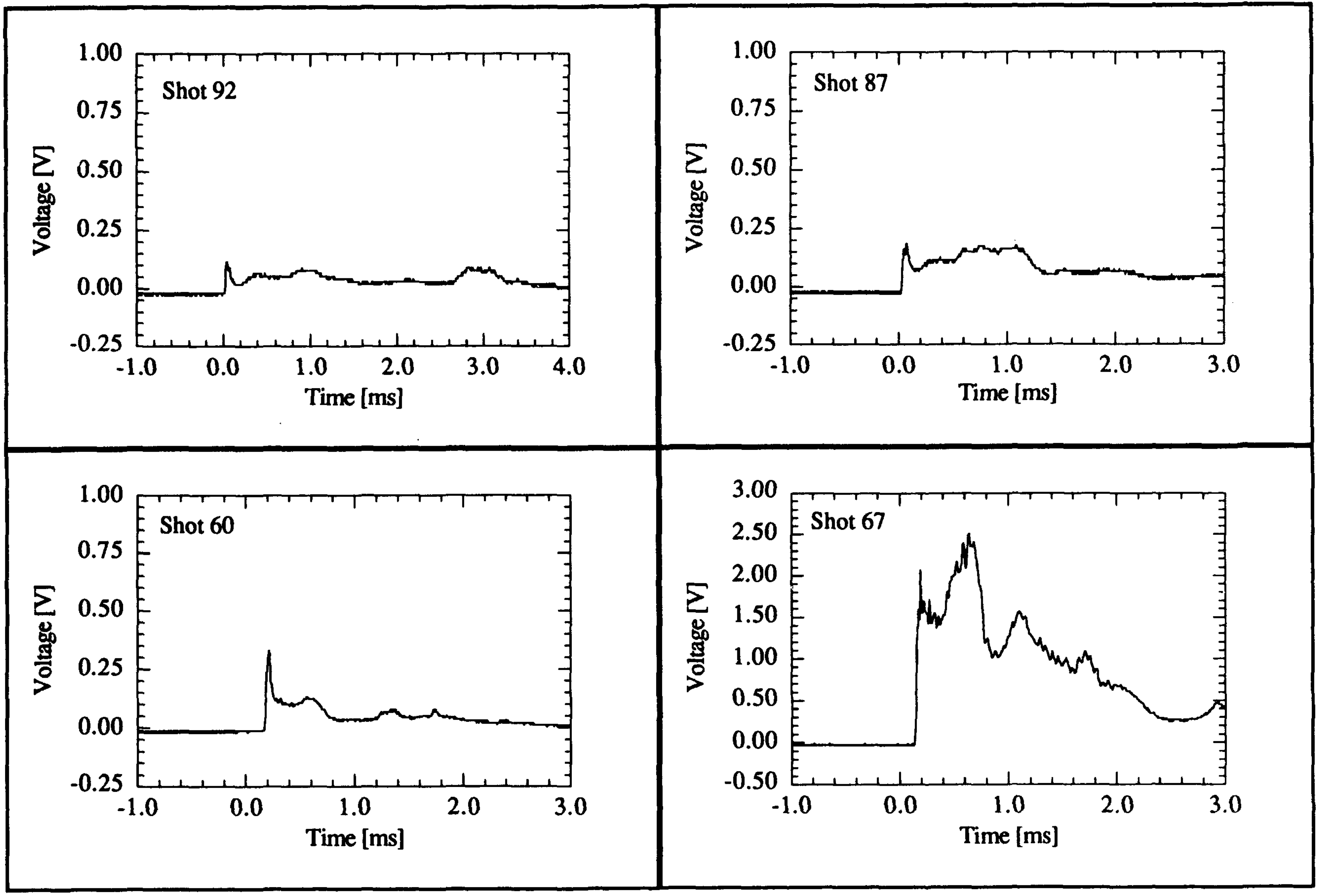

Figure D.3 Other photodiode signals of crystalline boron in 100% oxygen.

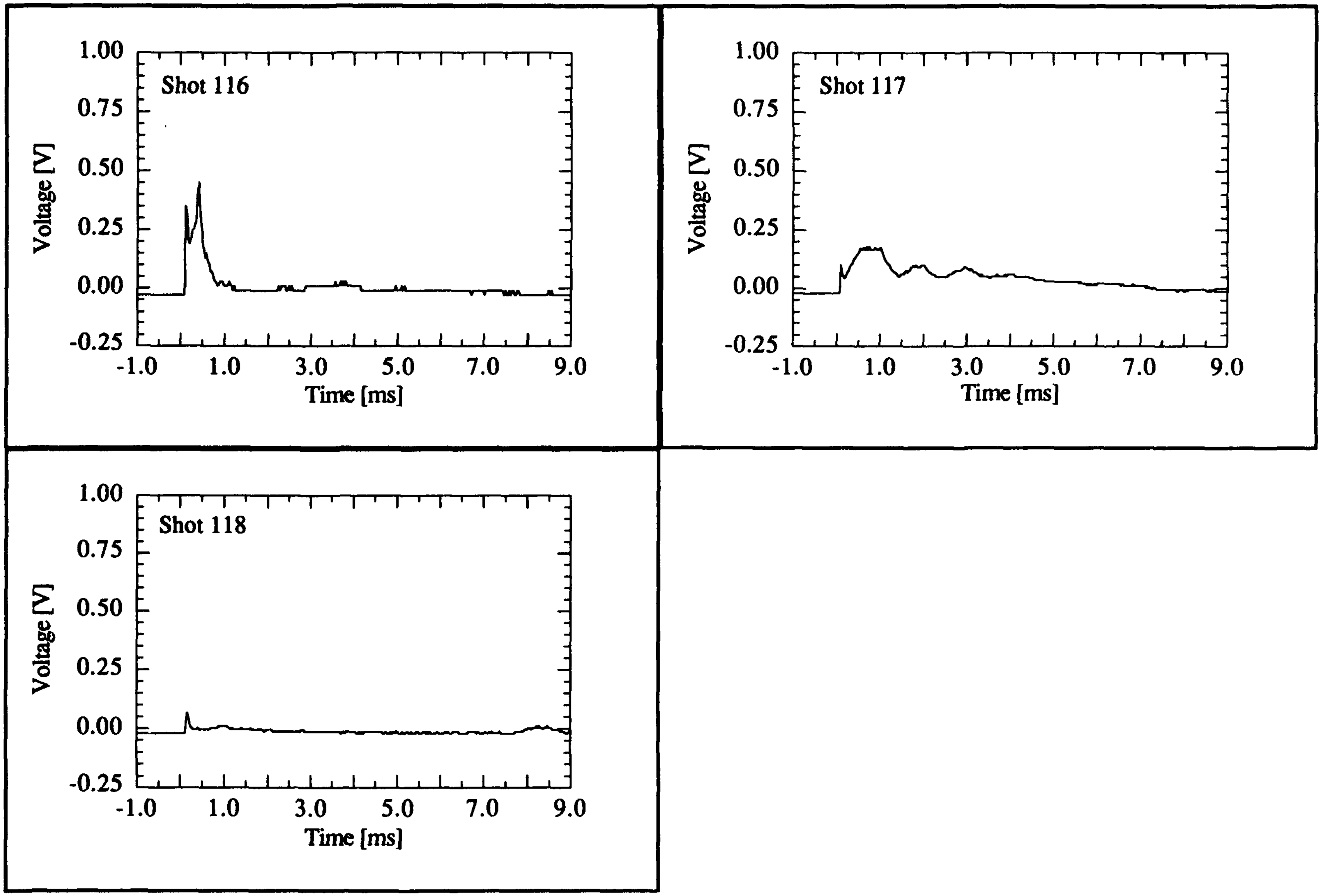

Figure D.4 Photodiode signals of cystalline boron in water vapor and oxygen.

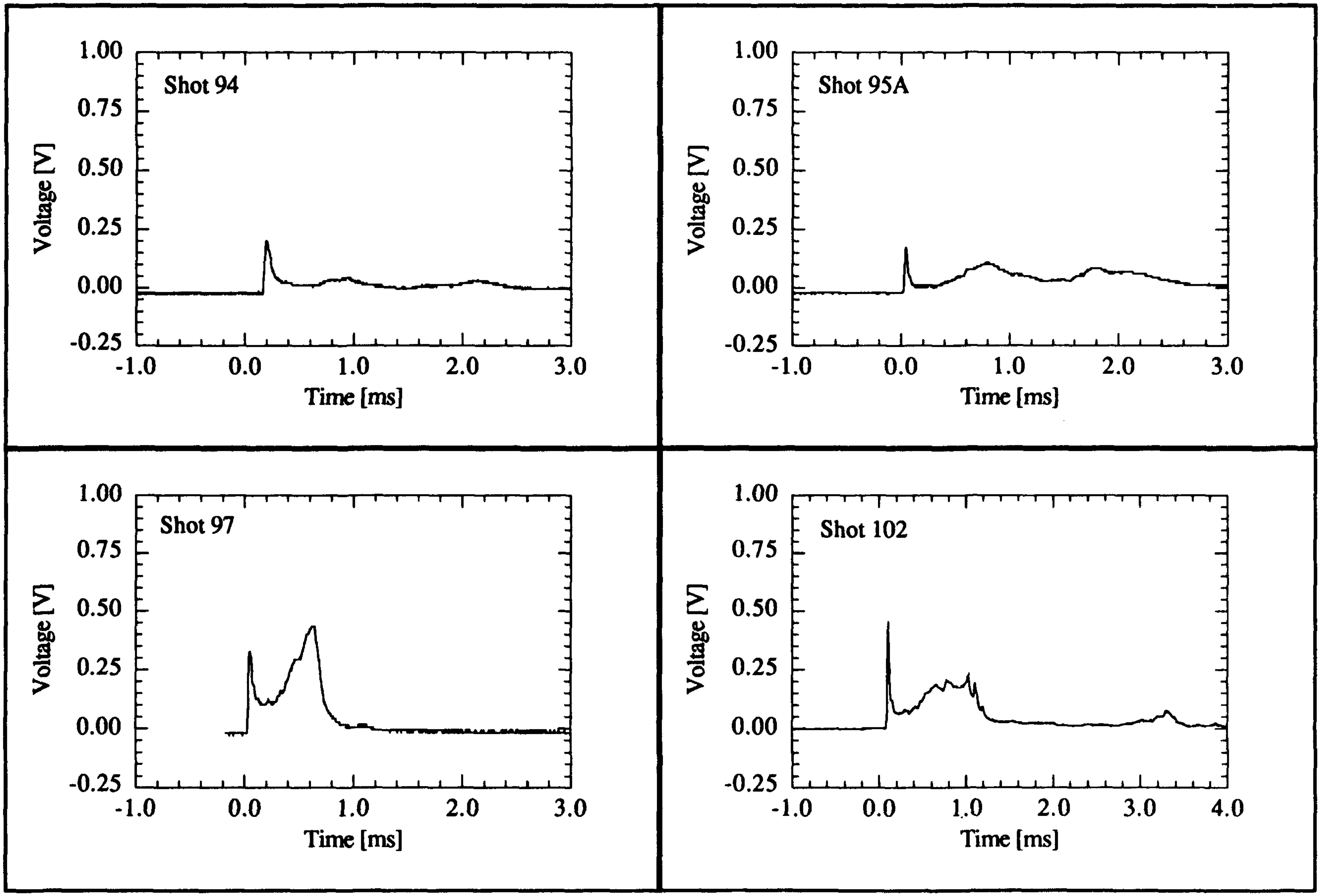

Figure D.5 Photodiode signals of cystalline boron in sulfur hexafluoride and oxygen.

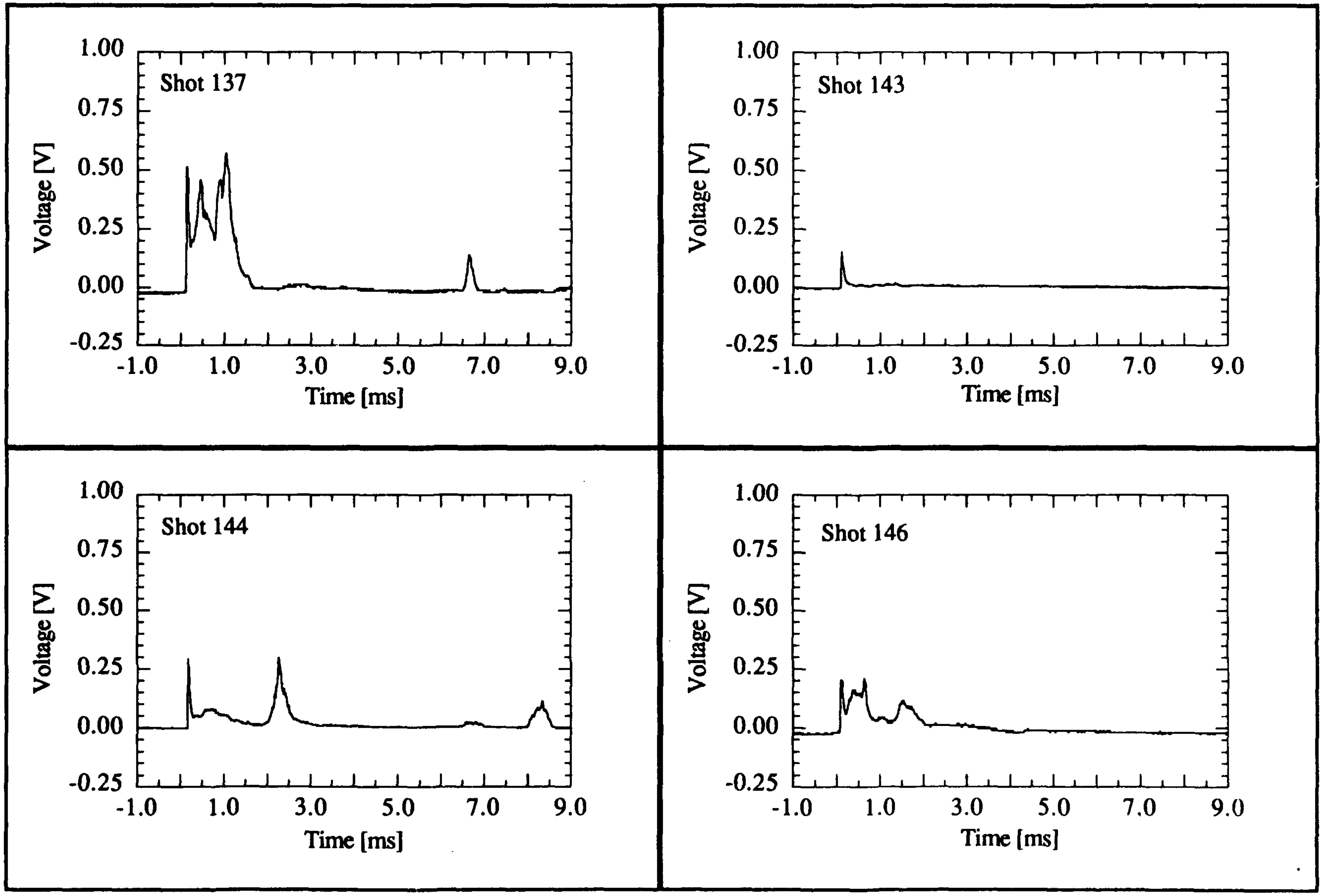

Figure D.6 Photodiode signals of cystalline boron in hydrogen fluoride and oxygen.

LIST OF REFERENCES

1. King, M.K., "Ignition and Combustion of Boron Particles and Clouds", **Journal of Spacecraft and Rockets**, Vol. 19, No. 4, pp. 294-306, Jul.-Aug. 1982.

2. Besser, H.L. and R. Strecker, "Overview of Boron Ducted Rocket Development During the Last Two Decades", **Combustion of Boron-Based Solid Propellants and Solid Fuels**, Edited by K.K. Kuo and R. Pein, CRC Press, Inc., Boca Raton, Florida, pp. 133-178, 1993.

3. Yetter, R.A., H. Rabitz, F.L. Dryer, R.C. Brown, and C.E. Kolb, "Kinetics of High-Temperature B/O/H/C Chemistry", **Combustion and Flame**, Vol. 83, pp. 43-62, 1991.

4. Roberts, T.A., R.L. Burton, and H. Krier, "Ignition and Combustion of Aluminum/Magnesium Alloy Particles in O_2 at High Pressures", **Combustion and Flame**, Vol. 92, No. 1 & 2, pp. 125-143, Jan. 1993.

5. Roberts, T.A., "Shock Tube Ignition and Combustion of Aluminum/Magnesium Alloy Particles in Oxygen at High Pressure", **Ph.D. Thesis**, University of Illinois at Urbana-Champaign, Urbana, Illinois, 1993.

6. **CRC Handbook of Chemistry and Physics**, 72nd ed., The Chemical Rubber Co., Cleveland, Ohio, 1991-1992.

7. Incropera, F.P. and D.P. DeWitt, **Fundamentals of Heat and Mass Transfer**, 3rd ed., John Wiley and Sons, Inc., New York, 1990.

8. Chase, M.W., **JANAF Thermochemical Data**, 3rd ed., American Chemical Society, Washington D.C., 1985.

9. **Journal of Physical and Chemical Reference Data**, Vol. 21, American Chemical Society, New York, 1992.

10. Mohan, G. and F.A. Williams, "Ignition and Combustion of Boron in O_2/Inert Atmospheres", **AIAA Journal**, Vol. 10, No. 6, pp. 776-783, Jun. 1972.

11. **TAPP, Thermochemical And Physical Properties**, Software Package, Version 1.0, E.S. Microware, Hamilton, Ohio, 1992.

12. Nemodruk, A.A. and Z.K. Karalova, **Analytical Chemistry of Boron**, Ann Arbor-Humphrey Science Publishers, London, pp. 5-16, 1969.

13. Glassman, I., F.A. Williams, and P. Antaki, "A Physical and Chemical Interpretation of Boron Particle Combustion", **Twentieth Symposium (International) on Combustion**, pp. 2057-2064, 1984.

14. Macek, A. and J.M. Semple, "Combustion of Boron Particles at Atmospheric Pressure", **Combustion Science and Technology**, Vol. 1, pp. 181-191, 1969.

15. Li, S.C. and F.A. Williams, "Ignition and Combustion of Boron in Wet and Dry Atmospheres", **Twenty-Third Symposium (International) on Combustion**, pp. 1147-1154, 1990.

16. Macek, A., "Combustion of Boron Particles: Experiment and Theory", **Fourteenth Symposium (International) on Combustion**, pp. 1401-1411, 1972.

17. Brown, R.C., C.E. Kolb, R.A. Yetter, F.L. Dryer, and H. Rabitz, "Advantages of Boron/Fluorine in Solid Propellants", Transparencies, Princeton University, 1992.

18. Roberts, T.A., "SHOCKTUBE", FORTRAN computer code, University of Illinois at Urbana-Champaign, 1992.

19. Talley, C.P., "The Combustion of Elemental Boron", **Solid Propellant Rocket Research**, Edited by M. Summerfield, Academic Press, New York, pp. 279-285, 1960.

20. Gurevich, M.A., I.M. Kir'yanov, and E.S. Ozerov, "Combustion of Individual Boron Particles", **Combustion, Explosion, and Shock Waves**, Vol. 5, No. 2, pp. 150-153, 1969.

21. Uda, R.T., "A Shock-Tube Study of the Ignition Limit of Boron Particles", **G.A./M.E. thesis**, Air Force Institute of Technology, Wright-Patterson Air Force Base, Dayton, Ohio, 1968.

22. Macek, A. and J.M. Semple, "Combustion of Boron Particles at Elevated Pressures", **Thirteenth Symposium (International) on Combustion**, The Combustion Institute, pp. 859-868, 1971.

23. Li, S.C., F.A. Williams, and F. Takahashi, "An Investigation of Combustion of Boron Suspensions", **Twenty-Second Symposium (International) on Combustion**, The Combustion Institute, pp. 1951-1960, 1988.

24. Yuasa, S. and H. Isoda, "Ignition and Combustion of Small Boron Lumps in an Oxygen Stream", **Combustion and Flame**, Vol. 86, pp. 216-222, 1991.

25. Childs, L.B., M.K. King, and J.D. Martin, "Improved Propellants for Throttleable Solid Air-Augmented Rockets", **AFRPL-TR-71-127**, Vol. 2, Dec. 1971.

26. Meinkohn, D, "The Ignition of Boron Particles", **Combustion and Flame**, Vol. 59, pp. 225-232, 1985.

27. Zvuloni, R., A. Gomez, and D.E. Rosner, "High Temperature Kinetics of Solid Boron Gasification by B_2O_3(g): Chemical Propulsion Implications", **Journal of Propulsion**, Vol. 7, No. 1, pp. 9-13, January-February 1991.

28. Pasternack, Louise, "Gas-Phase Modeling of Homogeneous Boron / Oxygen / Hydrogen / Carbon Combustion", **Combustion and Flame**, Vol. 90, pp. 259-268, 1992.

29. Brown, R.C., C.E. Kolb, H. Rabitz, S.Y. Cho, R.A. Yetter, and F.L. Dryer, "Kinetic Model of Liquid B_2O_3 Gasification in a Hydrocarbon Combustion Environment: I. Heterogeneous Surface Reactions", **International Journal of Chemical Kinetics**, Vol. 23, pp. 957-970, 1991.

30. Megli, T.W., H. Krier, and R.L. Burton, "Shock Tube Ignition of Al/Mg Alloys in Water Vapor and Argon", **Proceedings of the Third International Conference on Experimental Heat Transfer, Fluid Mechanics and Thermodynamics**, Honolulu, Hawaii, Oct. 31 - Nov. 5, 1993.

31. Megli, T.W., "Aluminum-Magnesium Particle Ignition in Shocked Mixtures of Water Vapor and Argon", **M.S. Thesis**, University of Illinois at Urbana-Champaign, Urbana, Illinois, 1993.

32. Zucker, R.D., **Fundamentals of Gas Dynamics**, Matrix Publishers, Inc., Chesterfield, Ohio, 1977.

33. Anderson, J.D. Jr., **Modern Compressible Flow with Historical Perspective**, 2nd ed., McGraw-Hill Publishing Co., New York, 1990.

34. Gordon, S. and B.J. McBride, "Computer Program for Calculation of Complex Chemical Equilibrium Compositions, Rocket Performance, Incident and Reflected Shocks, and Chapman-Jouguet Detonations", **NASA SP-273**, NASA, Mar. 1976.

35. Resler, E.L., S.C. Lin, and A. Kantrowitz, "The Production of High Temperature Gases in Shock Tubes", Journal of Applied Physics, Vol. 23, No. 12, p. 1390, 1952.

36. Holman, J.P., **Experimental Methods for Engineers**, 5th ed., McGraw-Hill Publishing Co., New York, 1989.

37. Li, S.C., "Experimental and Theoretical Studies of Ignition and Combustion of Boron Particles in Wet and Dry Atmospheres", **Ph.D. Thesis**, Princeton University, 1990.

38. Gross, R.J. and M.R. Baer, **Sandia National Laboratory Report SAND85-1273**, 1985.